
The old Nuclear Star Cluster in the Milky Way

Sotirios Chatzopoulos



München 2015

The old Nuclear Star Cluster in the Milky Way

Sotirios Chatzopoulos

Dissertation
an der Fakultätsname
der Ludwig–Maximilians–Universität
München

vorgelegt von
Sotirios Chatzopoulos
aus Athen, Griechenland

München, den 3 June 2015

Erstgutachter: Prof. Dr. Ortwin Gerhard
Zweitgutachter: Prof. Dr. Reinhard Genzel
Tag der mündlichen Prüfung: 17 July 2015

Contents

Zusammenfassung	xiii
Summary	xv
1 Our Milky Way Galaxy and its Nuclear Star Cluster.	1
1.1 The Galactic Center	1
1.1.1 The Central black hole Sgr* A	1
1.1.2 The young stars and the Paradox of Youth	4
1.1.3 The Minispiral and the CND	4
1.2 The old Nuclear Star Cluster of the Milky Way.	6
1.2.1 The stellar cusp problem	6
1.2.2 Dynamical structure & kinematics of the NSC	7
1.3 The Milky Way as a disk galaxy	9
1.3.1 The Galactic Disk	9
1.3.2 The Galactic Bulge	10
1.3.3 The Stellar Halo	11
1.4 Nuclear star clusters in external disk galaxies	13
1.5 Dynamical modeling of collisionless systems	16
1.5.1 The collisionless Boltzmann equation	16
1.5.2 Orbit-based and Particle-based methods	18
1.5.3 Analytic methods	20
2 The old nuclear star cluster in the Milky Way: dynamics, M_0, R_0, M_{BH}	23
2.1 Introduction	24
2.2 Dataset	24
2.3 Spherical models of the NSC	25
2.3.1 Mass model for the NSC	27
2.3.2 Spherical model	30
2.3.3 Adding self-consistent rotation to the spherical model	32
2.4 Axisymmetric modeling of the NSC	36
2.4.1 Axisymmetric Jeans modeling	37
2.4.2 Distance to the Galactic Center, mass of the star cluster, and mass of the black hole	42

2.4.3	Two-integral distribution function for the NSC	44
2.4.4	Adding rotation to the axisymmetric model: is the NSC an isotropic rotator?	47
2.5	Discussion	50
2.5.1	The dynamical structure of the NSC	50
2.5.2	Mass of the NSC	52
2.5.3	Evolution of the NSC	55
2.5.4	Distance to the Galactic center	56
2.5.5	Mass of the Galactic supermassive black hole	57
2.6	Conclusions	58
2.7	Two-integral distributions functions	59
2.8	Velocity histograms for the 2-I model	63
3	Dust within the old nuclear star cluster	69
3.1	Introduction	69
3.2	Effects of dust on the apparent dynamics of the NSC	72
3.2.1	Axisymmetric dynamical model of the NSC	72
3.2.2	Asymmetry of the v_l proper motion histograms	72
3.3	Differential extinction in the NSC	74
3.3.1	Total extinction	74
3.3.2	Extinction in the NSC region	77
3.4	Dust modeling	78
3.5	Predictions of the Dust model	81
3.6	Does the addition of dust affect the measured M_\bullet , M_* and R_0 ?	87
3.7	Discussion & Conclusions	92
4	Summary and Outlook	95
4.1	Summary	95
4.1.1	Modeling the NSC	95
4.1.2	Distance to the Galactic Center	96
4.1.3	Mass of the NSC	97
4.1.4	Mass of the Supermassive Black Hole	97
4.1.5	Dust within the NSC	98
4.2	Outlook	99
A	Multi-mass N-body realizations	103
A.0.1	Criticism on the ZM multi-mass scheme	104
A.0.2	Multi-mass and Made to Measure methods	105

List of Figures

1.1	Stellar Orbits close to Sgr A*	3
1.2	The minispiral structure	5
1.3	Typical velocity profiles of the NSC	9
1.4	The Milky Way bar's geometry and its rotation	12
1.5	Mean projected mass density against the total mass for various stellar systems	14
1.6	The prevalence of the central BH is increasing over the NSCs	15
2.1	Binning of the proper motion velocities	26
2.2	Binning of the line-of-sight velocities	27
2.3	Combination of two γ -models and number density	28
2.4	Isotropic DF for the two-component spherical model of the NSC including a central black hole	29
2.5	Modeled line-of-sight velocity dispersion and observed line-of-sight dispersions	31
2.6	Mean line-of-sight velocity data compared to the prediction of the two-component spherical model	33
2.7	Axisymmetric two-component model for the surface density of the nuclear cluster and number density	35
2.8	Velocity dispersions σ_l and σ_b compared to axisymmetric, semi-isotropic Jeans models.	39
2.9	Root mean square line-of-sight velocities compared with the best model	40
2.10	All three projected velocity disperions compared	41
2.11	Contour plots for the marginalized χ^2 in the three parameter planes (R_0, M_\bullet) , (M_\bullet, M_*) , (R_0, M_*)	43
2.12	Contours from stellar orbits, this work and combination of those	45
2.13	2I-DF for our best Jeans model	46
2.14	Typical velocity distributions for l and b -velocities within the area of interest ($r < 100''$)	48
2.15	Predicted distributions of v_l velocity compared to the observed histograms.	49
2.16	Best fitting model from the 2I DF compared to the isotropic rotator model.	51
2.17	Average differential extinction of nuclear cluster stars plotted as a function of v_l proper motion.	53
2.18	The mass, density and the potential of the NSC	54

2.19	The contour used for the numerical evaluation of $f(E, L_z)$ for the case where $\Psi_\infty = 0$	61
2.20	Our best DF for $\eta = 0.5$	62
2.21	VHs and VPs in the l and b directions predicted by the 2I model in angular bins.	64
2.22	VHs and VPs in the l and b directions predicted by the 2I model in radial bins.	65
2.23	VHs for the symmetrized los data compared with the corresponding even VPs of the model.	66
2.24	Line-of-sight VHs compared with the corresponding VPs of the model including rotation.	67
3.1	Effects of dust, rotation and triaxiality on the apparent dynamics of the NSC	71
3.2	VH data and VPs in the l direction predicted by the axisymmetric model and dust model.	73
3.3	Map of A_K for the NSC derived from $H - K$ colors.	75
3.4	Histogram of the extinction A_K based on $H - K$ colors for all the stars. . .	76
3.5	Average differential extinction of nuclear cluster stars plotted as a function of v_l and v_b proper motion.	77
3.6	Extinction derived from the observed ratio of Pa α to H92 α radio recombination-line emission (Roberts & Goss, 1993).	79
3.7	Modeled K luminosity with completeness function before and after a dust effect with $A_K = 0.4$	81
3.8	Percentage reduction in observable stars after a dust effect with $A_K = 0.4$. . .	82
3.9	VPs in l direction for different models.	83
3.10	Shape of δA_K versus v_l curve for several dust models.	86
3.11	Predictions of the model with the VH and δA_K data for each cell. The numbers in the brackets show where the screen of dust is placed relative to the center. Reduced χ^2 are also provided for the histograms and the photometry. For the cells A1, A2, B, C2, E, the screen dust distance is based on the orbit models of the mini-spiral (Zhao et al., 2009).	88
3.12	Predictions of the model with the VH and δA_K data for the outer cells shown in Fig.3.3.	89
3.13	Even part of the renormalized VPs for v_l, v_b and v_{los} for a NSC dynamical model with no dust and the same dynamical model including the dust screen prediction based on cell B.	91
4.1	Typical velocity distribution for v_l with the corresponding velocity histograms (left) along with the odd part of the model and the data (right) . .	101
A.1	Formal relative errors in mass included in logarithmically placed spherical cells of a Hernquist model	104

A.2	A Hernquist multi-mass realization with $N = 10^6$ particles with and without black hole.	105
A.3	Two snapshots (Model 1 and Model 2) of slit kinematics of the fitted multi-mass Hernquist particle realization	107

List of Tables

3.1	Inferred line-of-sight distance of the dust screen from Sgr A* for each one of the eight cells of Fig. 3.10	87
3.2	Extinction values per cell based on Fig. 3.3.	87

Zusammenfassung

Das Hauptanliegen dieser Arbeit ist es, den alten Nuclear Star Cluster (NSC) im Zentrum der Milchstraße zu studieren. Es werden neue Wertebereiche für die Masse, die Rotation, die Bahnstruktur und die statistische Parallaxe des galaktischen NSC, und für die Masse des supermassiven Schwarzen Loches abgeleitet. Diesen zugrunde liegen die Eigenbewegungen von ~ 10000 Sternen, ~ 2500 line-of-sight Geschwindigkeiten sowie Sternenzählungen von Fritz et al. (2014), erhalten durch VLT-Beobachtungen. Außerdem wird erstmals eine Messung der Extinktion des Staubes innerhalb des galaktischen Nuclear Star Clusters durchgeführt.

Zunächst wird die Oberflächendichte der Sterne in den zentralen $1000''$ durch eine Superposition eines sphäroidischen Haufens mit einem Skalenradius von $\sim 100''$ und einer viel größeren nuklearen Scheibe angepasst. Die Benutzung von zwei separaten abgeflachten Modellen ist vom Vorteil, da so ein nicht konstantes axiales Verhältnis berücksichtigt werden kann. Aus der Massendichte lässt sich das totale Potential aus der Summe der Potentiale der zwei Modelle plus dem des Schwarzen Lochs berechnen.

Letztendlich ist es das Ziel, die Verteilungsfunktion (DF) des NSC zu erhalten, welche die Verteilung der stellaren Masse im Phasenraum beschreibt. Es gibt zwei Methoden, um die DF eines Systems zu erhalten, einmal durch Verwendung eines Teilchensystems oder der Sternbahnen, oder aber durch analytische Methoden, die auf der stellardynamischen Theorie basieren. Für diese Arbeit wird eine analytische Methode benutzt, da sie an sich genauer ist (das Problem des Teilchen-Rauschens ist abwesend). Spezifisch wird die selbstkonsistente Zweiintegral-Verteilungsfunktion $f(E, L_z)$ für die oben genannten Dichtemodelle bestimmt, und die Rotation selbstkonsistent hinzugefügt.

Damit wird gezeigt, dass der Unterschied zwischen den Dispersionen der Eigenbewegungen σ_l und σ_b nicht durch Rotation erklärt werden kann, sondern eine Konsequenz der Abflachung des NSC ist. Die Bahnstruktur der $f(E, L_z)$ steht in exzellenter Übereinstimmung mit den beobachteten Geschwindigkeitsdispersionsprofilen, wie auch mit den Eigenbewegungs- und line-of-sight-Geschwindigkeitshistogrammen, einschließlich des Doppelpeaks im v_l -Histogramm. Durch das Anwenden axisymmetrischer Jeans Modellierung erhält man dann aus den Eigenbewegungs- und line of sight- Geschwindigkeitsdispersionen neue Abschätzungen der NSC Masse, der Schwarzen Loch Masse, und der Distanz zum Galaktischen Zentrum von $M_*(r < 100'') = (8.94 \pm 0.31|_{\text{stat}} \pm 0.9|_{\text{syst}}) \times 10^6 M_\odot$, $M_\bullet = (3.86 \pm 0.14|_{\text{stat}} \pm 0.4|_{\text{syst}}) \times 10^6 M_\odot$, und $R_0 = 8.27 \pm 0.09|_{\text{stat}} \pm 0.1|_{\text{syst}}$ kpc. Eine gemeinsame statistische Analyse mit den Ergebnissen aus Gillessen et al. (2009) basierend

auf den Sternbahnen um Sgr A* ergibt $M_{\bullet} = (4.23 \pm 0.14) \times 10^6 M_{\odot}$ und $R_0 = 8.33 \pm 0.11$ kpc. Die Bestimmung der Distanz ist besonders wichtig, da R_0 als Skalenfaktor der galaktischen Struktur wirkt und die Abschätzung von Massen und anderen Parametern galaktischer und extragalaktischer Objekte beeinflusst.

Wegen hoher interstellarer Extinktion durch Staub ist es unmöglich, den NSC mit einem optischen Teleskop zu beobachten. Deshalb sind wir auf Beobachtungen im infraroten Bereich angewiesen, da der Staub für größere Wellenlängen transparenter wird. Die mittlere absolute Extinktion in Richtung des zentralen parsec der Milchstraße ist $A_K \simeq 3$ mag, einschließlich des Staubs im Vordergrund und im galaktischen Zentrum.

In dieser Arbeit wird eine Messung der Staubextinktion *innerhalb* des galaktischen Nuclear Star Clusters abgeleitet, die auf den differentiellen Extinktionen der NSC Sterne sowie der Korrelation mit ihren v_l Eigenbewegungen entlang der galaktischen Länge beruht. Das Interesse an diesem Problem wurde von Beobachtungen geweckt, die zeigten, dass der positive Geschwindigkeitspeak des Geschwindigkeits-Histogramms in Richtung der galaktischen Länge konsequent leicht höher ist als der negative Geschwindigkeitspeak.

Eine Erklärung für diese Asymmetrie ergibt sich durch das Vorhandensein des Staubes *innerhalb* des NSC. Wegen des Staubes ist die sichtbare Anzahl der Sterne hinter dem NSC geringer, als die der vor dem Cluster liegenden. Dieses beobachtete Merkmal kann in Verbindung mit der Rotation erklärt werden. Durch den Vergleich der vorhergesagten Asymmetrie mit Daten von ~ 7100 Sternen in verschiedenen Gebieten des NSC ergibt sich, dass Staub assoziiert mit der Mini-Spirale im galaktischen Zentrum mit Extinktionen $A_K \simeq 0.15 - 0.8$ mag den Großteil der Daten erklärt. Schließlich wird berechnet, dass für eine typische Extinktion von $A_K \simeq 0.4$ die statistische Parallaxe des NSC sich um $\sim 0.4\%$ ändert, so dass systematische Effekte in der gemessenen Distanz durch Staubextinktion gering sind.

Summary

The main subject of this work is the study of the old nuclear star cluster (NSC) in the Milky Way. New constraints are derived on the mass, rotation, orbit structure and statistical parallax of the Galactic old nuclear star cluster and the mass of the super-massive black hole. For this ~ 10000 proper motions, ~ 2500 line-of-sight velocities, and star counts from Fritz et al. (2014) obtained with VLT instruments are used. In addition, for the first time a measurement of dust extinction within the Galactic old nuclear star cluster is presented.

As a first step, the surface density distribution of stars in the central $1000''$ is fitted by a superposition of a spheroidal cluster with scale $\sim 100''$ and a much larger nuclear disk component. The use of two flattened models is advantageous because it allows for a non-constant axial ratio. Having the density allows us to calculate the total potential as a sum of the two model potentials plus the black hole potential.

Eventually the goal is the distribution function (DF) of the NSC, that is the distribution of stellar mass over the phase space. There are two methods of acquiring the DF of a system, using particle systems or orbits, or through analytical methods based on stellar dynamics theory. In this thesis an analytical method is used since it is intrinsically more accurate (the problem of particle noise is absent). Specifically, the self-consistent two-integral distribution function $f(E, L_z)$ is computed for the above mentioned density model, and rotation is added self-consistently.

It is shown that the difference between the proper motion dispersions σ_l and σ_b cannot be explained by rotation, but is a consequence of the flattening of the NSC. The orbit structure of the $f(E, L_z)$ gives an excellent match to the observed velocity dispersion profiles as well as the proper motion and line-of-sight velocity histograms, including the double-peak in the v_l -histograms. By applying axisymmetric Jeans modeling to the proper motions and line-of-sight velocity dispersions, best estimates are obtained for the NSC mass, black hole mass, and distance $M_*(r < 100'') = (8.94 \pm 0.31|_{\text{stat}} \pm 0.9|_{\text{syst}}) \times 10^6 M_\odot$, $M_\bullet = (3.86 \pm 0.14|_{\text{stat}} \pm 0.4|_{\text{syst}}) \times 10^6 M_\odot$, and $R_0 = 8.27 \pm 0.09|_{\text{stat}} \pm 0.1|_{\text{syst}}$ kpc. A joint statistical analysis with the results of Gillessen et al. (2009) based on orbits around Sgr A* gives $M_\bullet = (4.23 \pm 0.14) \times 10^6 M_\odot$ and $R_0 = 8.33 \pm 0.11$ kpc. The constraint of the distance is particularly important since R_0 acts as a scale factor for the Galactic structure and impacts mass estimations and other parameters of Galactic and extra-galactic objects.

Because of high interstellar extinction caused by dust, it is impossible to observe the NSC with an optical telescope. Therefore we rely on observations taken in the infrared

because the dust is more transparent for larger wavelengths. The mean absolute extinction towards the central parsec of the Milky Way is $A_K \simeq 3$ mag, including both foreground and Galactic center dust.

In this work, a measurement is presented for the dust extinction *within* the Galactic old nuclear star cluster, based on combining differential extinctions of NSC stars with their v_l proper motions along Galactic longitude. Interest in this problem was triggered by the observation that the positive velocity peak of the velocity histograms in Galactic longitude is consistently slightly higher than the negative velocity peak.

An explanation is given for this asymmetry based on the existence of dust *within* the NSC. Because of the dust, the apparent number of stars behind the NSC is smaller than that in front of the cluster. This in conjunction with the rotation can explain the observed characteristic. Comparing the predicted asymmetry to data for ~ 7100 stars in several NSC fields, it is found that dust associated with the Galactic center mini-spiral with extinction $A_K \simeq 0.15 - 0.8$ mag explains most of the data. Finally, it is estimated that for a typical extinction of $A_K \simeq 0.4$ the statistical parallax of the NSC changes by $\sim 0.4\%$, so that systematic effects on the measured distance due to dust extinction are small.

Chapter 1

Our Milky Way Galaxy and its Nuclear Star Cluster.

This chapter consists of five sections. In the first of these, I describe aspects of the Galactic Centre (GC) which are related to the Nuclear star Cluster (NSC), the main subject of this thesis. The second section is dedicated to the NSC itself and its dynamics. In the third section follows an introduction to the larger-scale components of the Milky Way (MW). In the fourth section I describe NSCs beyond the MW including available formation models. Finally in the fifth section I present the available dynamical tools and theory that can be used to model a NSC.

1.1 The Galactic Center

1.1.1 The Central black hole Sgr* A

It is now well known (e.g. Ferrarese & Ford., 2005) that the center of most galaxies contain a supermassive black hole. In the 1930s a bright non-thermal radio source was discovered by Jansky (1933) at the center of the Milky Way. The radio source was named Sagittarius A* (Sgr A*) because it was projected near the Sagittarius constellation. Now it is believed that Sgr A* is the location of a supermassive black hole (Genzel et al., 2010).

The first indications of a massive black hole in the Galactic center emerged in the late 1970s with the work of Wollman et al. (1977). They discovered that the radial velocities of ionized gas over a region $40''$ from the center ranged from $+250$ km/s to about -350 km/s. From this they estimated that the total mass within a radius of 1 pc about the galactic center is $\sim 4 \times 10^6 M_{\odot}$. However no infrared or X-Ray source was detected near Sgr A* (Allen & Sanders, 1986) so it was not certain whether Sgr A* harbored a supermassive black hole (SMBH). The argument was settled later with the observation of stellar orbits (more on this matter later).

The earliest stellar dispersion measurements (therefore non-individual stellar orbits) derived from the $2\mu\text{m}$ CO absorption bands of late-type giants (Rieke et al., 1988; McGinn

et al., 1989). However these measurements were far away from the center and failed to constrain accurately the central non stellar mass. Genzel et al. (1996) used radial velocities of 223 early and late-type stars from 0.1 to 5 pc acquired from K-band imaging spectroscopy and applying projected mass estimators they constrained the central dark mass to $2.5 - 3.2 \times 10^6 M_\odot$ at $6-8\sigma$ significance.

The Sgr A* is special because at a distance of ~ 8 kpc it is the closest SMBH we can observe. This gives us the ability to observe the stars and gas near the black hole in much greater detail than any other SMBH (e.g. the next closest SMBH is at the center of Andromeda galaxy ~ 100 further than Sgr A*). However even at this distance observations in the Optical-UV wavelength are impossible because of the high extinction close to $A_V \sim 30$ mag (this means that only 10^{-12} photons in the optical reach Earth) by interstellar dust. Instead observations are made in the IR where the extinction in K-band is only $A_K \sim 3$ mag (Rieke et al., 1989).

The next major step came with the detection of proper motions (motions in the plane of the sky) within the central few arcseconds. This allowed us for the first time to get hints of the 3D stellar velocity structure close to the center. Eckart & Genzel (1996) reported the proper motions of 39 stars located between 0.04 and 0.4 pc from the Galactic Center. They found that the velocity dispersion estimated from the proper motions is in excellent agreement with that obtained from the radial velocities and placed a lower limit of $6.5 \times 10^9 M_\odot \text{pc}^{-3}$ on the density of the central region. The number of detected proper motion increased very fast. Schödel et al. (2010) used 6000 proper motions within 1 pc from Sgr A* obtained with NACO/CONICA at the ESO VLT. By applying Jeans modeling they found a best-fit black hole mass of $3.6_{-0.4}^{+0.6} \times 10^6 M_\odot$ consistent with the canonical value of $4 \times 10^6 M_\odot$.

We saw in the previous paragraph that the mass of the central black hole can be calculated by applying Jeans modeling to a set of stellar motions. The problem with this procedure is that most of the times the modeling does not guaranty the uniqueness of the solution. For example in spherical Jeans modeling there is a degeneracy between the radial velocity dispersion and the anisotropy (e.g. Binney & Tremaine, 2008). In Chapter 2 (Chatzopoulos et al., 2015) we combined star counts and kinematic data from Fritz et al. (2014) including 2500 line-of-sight velocities and 10000 proper motions obtained with VLT instruments. By applying axisymmetric Jeans modeling supported also from the very good match of the Velocity Profiles (VPs) to the corresponding $f(E, L_z)$, we found a mass of $(3.86 \pm 0.14)_{stat} \pm 0.4)_{syst} \times 10^6 M_\odot$. In addition a comparison of the distribution function $f(E, L_z)$ to the histograms gave us a good description of the NSC. In this way, much of anisotropy-mass degeneracy was removed. A joint statistical analysis with the S-orbits (see next paragraph, Gillessen et al., 2009) gives $(4.23 \pm 0.14) \times 10^6 M_\odot$ and $R_0 = 8.33 \pm 0.11$ kpc.

Probably the best indicator of the existence of the Sgr A* SMBH is the individual stellar orbits near it. Stars orbiting sufficiently close to a several million solar masses object would behave as test particles under the Keplerian laws or the general relativity approximation.

The first success towards the individual orbit goal came with the determination of the orbit of the star S2 (Schödel et al., 2002; Ghez et al., 2003). Having a high ellipticity of

$e = 0.88$ the pericenter of the S2 star is merely 17 light hours from the Sgr A*. The first orbital analysis gave $4.1 \times 10^6 M_\odot$ (Schödel et al., 2002) and $4.6 \times 10^6 M_\odot$ (Ghez et al., 2003) for a rescaled distance of $R_0 = 8.3$ kpc (most recent estimation) in agreement with each others statistical analysis. Recently Gillessen et al. (2009) presented the results of 16 years of monitoring stellar orbits around Sgr A* using near infrared techniques. They obtained orbits for 28 late-type including the S2 star and they determined the orbital parameters for six of those stars. Their best value for the mass of the SMBH is $(4.31 \pm 0.06|_{stat} \pm 0.36|_{syst}) \times 10^6 M_\odot$ for $R_0 = 8.33 \pm 0.35$ pc. Fig 1.1 shows 20 out of 30 stellar orbits close to Sgr A* (Gillessen et al., 2009). The S2 orbit was the first full orbit recorded from observations.

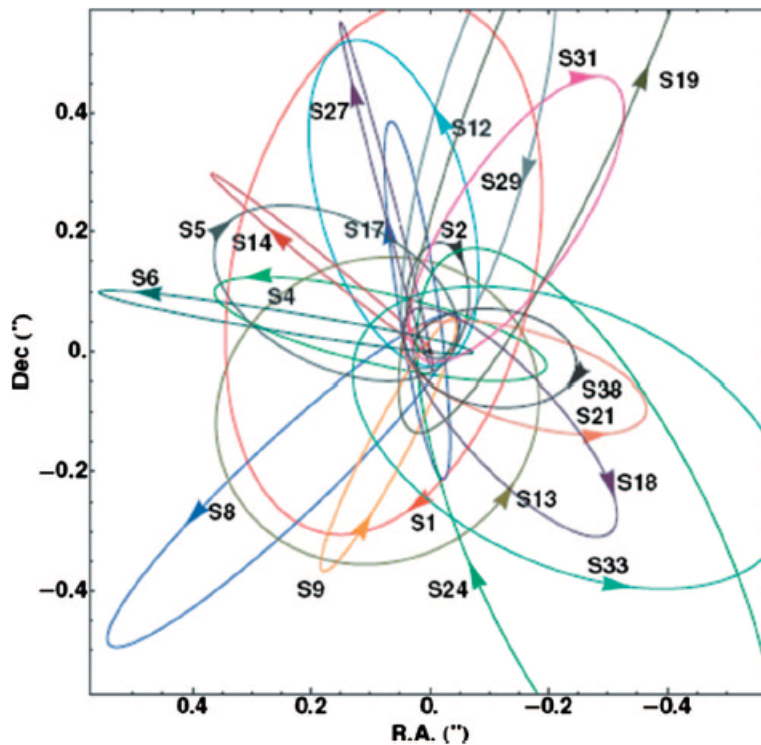


Figure 1.1: At the time of writing at least 30 S-star orbits have been isolated around Sgr A*. This plot shows 20 of them delineated from recent orbital analysis. The S2 orbit was the first full orbit recorded from observations. Fig. from Gillessen et al. (2009).

Observations of nearby galaxies show a strong correlation of their central SMBH and the velocity dispersion σ of the host galaxy (Tremaine et al., 2002; Alexander, 2005).

$$M_\odot \simeq 1.3 \times 10^8 \left(\frac{\sigma}{200 \text{ km s}^{-1}} \right)^{\beta_{m/\sigma}}, \beta_{m/\sigma} \sim 4 - 5 \quad (1.1)$$

This relation indicates a connection between the SMBH and its host galaxy. The Sgr A* SMBH follows the m/σ relation (Valluri et al., 2005). With a mass of $\sim 4 \times 10^6 M_\odot$ (see

later discussion about mass determination) the Sgr A* black hole is one of the lightest known SMBHs in accordance with the small bulge of the Milky way (Alexander, 2005). With this mass its radius of influence is $r_h = 90''$ and its event horizon is at much smaller radius $r_h = 9\mu\text{arcsec}$.

1.1.2 The young stars and the Paradox of Youth

The central parsec around Sgr A* contains thousands of stars. About 96% of those stars are old late-type giant stars (> 5 Gyr) the rest are early-type massive young stars with ages ~ 6 Myr (Genzel et al., 1996; Paumard et al., 2006). These include Wolf-Rayet stars, O and B main sequence stars and supergiant stars (e.g. Bartko et al., 2010). Most of these Wolf-Rayet, O and B stars reside in two strongly warped disks between $0.8''$ and $12''$ as well as a central compact concentration (the S-Star cluster) of B-stars centered on Sgr A*. Their half number radius is $r \sim 7''$ and only very few of them are outside of $r > 15''$ (Fritz, 2013). The later type B-stars in the radial interval between $0.8''$ and $12''$ seem to be in a more isotropic distribution outside the disks (Bartko et al., 2010).

The existence of so many young stars close to the center is unexpected because of the strong tidal forces the central black hole would disrupt any initial gas cloud before collapsing. Therefore how did the young stars get into the central parsec? Were they formed in situ or drifted from outside? The first scenario (in situ formation) is problematic because star formation within the central parsec requires substantial compression of the gas (Morris, 1993) while the second is also implausible since in the central parsec the two body relaxation time is much larger than the age of those stars. This problem has been termed the paradox of youth (Ghez et al., 2003).

Several possible solutions have been proposed for this problem (Ghez et al., 2003). The most promising one supports the in situ formation of those stars (Levin & Beloborodov, 2003; Bonnell & Rice, 2008). According to this scenario a recent burst of star formation has occurred in a dense gaseous disk around Sgr A*. Such a disk is no longer present therefore it is guessed that the remaining gas is accreted or expelled by the central black hole.

1.1.3 The Minispiral and the Circumnuclear disk

The area inside $\sim 1 - 1.5$ pc radius consists of several streamers of dust, ionized and atomic gas with temperatures between $100K - 10^4K$ and it is called “ionized central cavity” (Ekers et al., 1983). An important feature of the ionized cavity is the so called “minispiral”, named after its distinctive shape that resembles a spiral. Outside of the minispiral (and the ionized cavity) at radius $\sim 1.5 - 4$ pc lies the circumnuclear disk (CND) which is a set of streamers of dense molecular gas and warm dust (Becklin et al., 1982; Guesten et al., 1987). The gas density of the CND is higher than that of the minispiral and there is a sharp transition at ~ 1.5 pc. The total mass of the ionized gas in the central cavity is quite small $\sim 30M_\odot$. Additionally there is about $300M_\odot$ of dense neutral hydrogen gas, a few M_\odot of warm dust

(Davidson et al., 1992) and an inferred inflow rate into the central parsec of $3 \times 10^{-2} M_{\odot} \text{yr}^{-1}$ (Jackson et al., 1993).

The minispiral is fed by several streamers of infalling gas and dust from the inner part of the CND (Kunneriath et al., 2012) and it consists of four main components: the northern arm, the eastern arm, the western arm and the bar (Zhao et al., 2009) surrounded by the circumnuclear disk of inner radius ~ 1.6 pc (Christopher et al., 2005; Jackson et al., 1993). These three streams (northern, eastern, western) were modeled by Zhao et al. (2009) using three bundles of Keplerian orbits around Sgr A* with some significant deviations. Assuming that each of the observed streams of ionized gas follows a single orbit, they determined the five orbital parameters (a, e, Ω, ω, i) of them using least-square fitting to the geometry of the ionized streams. According to their findings, both the Northern and Eastern Arm streams have high eccentricities ($e \sim 0.8$), while the Western Arc stream is nearly circular ($e \sim 0.2$) (Fig. 1.2). The three streams rotate counterclockwise as seen from the Earth and have orbital periods in the range $4 - 8 \times 10^4 \text{yr}$ (Zhao et al., 2009). The typical electron density and temperature in the arms are $3 - 21 \times 10^4 \text{cm}^{-3}$ and $5000 - 13000 \text{K}$ respectively Zhao et al. (2010). In Chapter 3 (Chatzopoulos et al., 2015b) we modeled the dust within the nuclear star cluster using the observed proper motions. We found some correlation between the dust inferred from local extinction variation and the western arc of the minispiral.

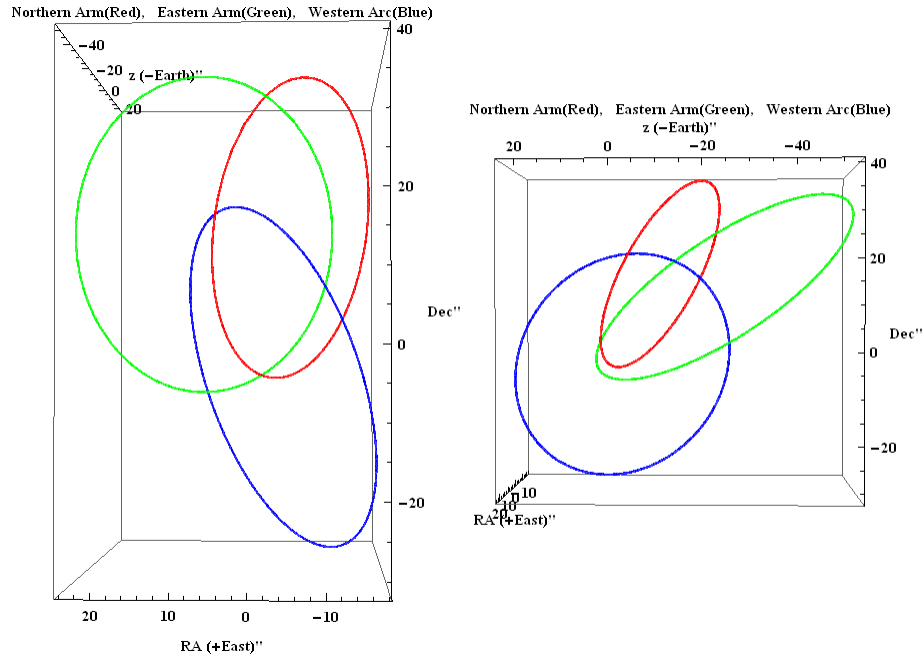


Figure 1.2: The three streams of the minispiral as they were modeled by Zhao et al. (2009). The Earth is towards negative z . The streams rotate counterclockwise as seen from the Earth and have orbital periods in the range $4 - 8 \times 10^4 \text{yr}$ (Zhao et al., 2009). The black hole lies at the origin.

1.2 The old Nuclear Star Cluster of the Milky Way.

The dominant structure of the inner Kpc in the MW is the Nuclear Bulge with stellar mass and luminosity of $(1.4 \pm 0.6) \times 10^9 M_\odot$ and $(2.5 \pm 1.0) \times 10^9 L_\odot$ respectively (Launhardt et al., 2002). The Nuclear Bulge appears as a distinct, massive disk-like complex of stars and molecular clouds which is, on a large scale, symmetric with respect to the Galactic Center (Launhardt et al., 2002). The Nuclear Bulge consists of the Nuclear Star Cluster (NSC) at the center and a large Nuclear Stellar Disk (NSD) with radius 230 ± 20 pc and scale height 45 ± 5 pc, as well as a Nuclear Molecular Disk (Launhardt et al., 2002).

The NSC was discovered as a source of infrared radiation at wavelengths of 1.65, 2.2 and 3.4μ by Becklin & Neugebauer (1968) using aperture with angular resolutions from $0.08'$ to $1.8'$. It was found to be a structure with a full width at half-maximum of $3' - 5'$ and elongated along the Galactic Plane. As in the Galactic center the NSC is invisible in optical wavelengths with an extinction of $A_V = 30$ mag. This is not the case for the infrared the extinction is $A_{K_s} \sim 3.0$ (e.g. Fritz et al., 2014). The NSC formation started about 10 Gyr ago when its average nuclear star formation rate was maximum. Afterwards the star formation rate dropped to a minimum 1 – 2 Gyr ago and increased again the last few hundred Myrs (Pfuhl et al., 2011). About 80% of its stellar mass formed about 5 Gyr ago (Blum & Ramirez, 2003; Pfuhl et al., 2011).

The formation mechanism of the NSC is still an open problem. The available scenarios can be split in two main categories (for details see section 1.4): (i) Several dense clusters migrated towards the center via dynamical friction and formed the NSC (ii) The NSC was build in situ from gas infall and subsequent star formation near the center (e.g. Böker, 2009)

1.2.1 The stellar cusp problem

One interesting theoretical problem is the shape of the stellar density distribution close to the center of a relaxed system that contains a black hole. Since the density distribution near the center can be approximated with a power-law of the form $\rho \propto r^{-\gamma}$ we seek for the value of γ . First steps towards the solution were done by Bahcall & Wolf (1976) when they found that $\gamma = 7/4$ for a spherical symmetric cluster close to equilibrium with approximately isotropic distribution in velocity space, assuming that all of its stars have the same mass. The value $\gamma = 7/4$ was confirmed later numerically by Preto et al. (2004). This is called the weak-segregation solution and it is considered suitable for globular clusters. For the NSC the strong-segregation solution is more suitable in which $\gamma = 11/4$ for the rare massive stellar objects and $\gamma = 3/2$ for the light ones (Preto & Amaro Seoane, 2010). Initial estimates on star counts from 8m telescopes (Genzel et al., 2003) showed that $\gamma = 1.4 \pm 0.1$ which is consistent with the later value. However, this estimation includes the massive young stars within a few ~ 0.1 pc. These stars cannot be dynamically relaxed since they are so young and therefore cannot be part of the equilibrium cusp. When these stars are excluded the stellar density is too flat to be consistent with a classical cusp. Recent estimates of the density slope based on the late-type stars give values as low as

$\gamma = 0.05_{-0.60}^{+0.29}$ (Do et al., 2013), however values smaller than $\gamma = 0.5$ are inconsistent with the presence of the central black hole at least for spherical models (Tremaine et al., 1994) and axisymmetric models to the form $f(E, L_z)$ (Hunter & Qian, 1993). This describes the cusp or core problem which is still open.

Possible solutions of the problem are (Alexander, 2005; Schödel et al., 2014): (i) The cusp exists but it is invisible because of the existence of dark objects like black holes or faint giant stars near the center. (ii) The cusp around Sgr A* has not yet been formed which means that the relaxation time near the center is larger than expected. (iii) The cusp has been destroyed by the infall of an intermediate-mass black hole and has not yet had the time to regrow. According to the last scenario, the cusp could regrow at the center of a galaxy after being destroyed in a merger event of two central black holes (Merritt & Szell, 2006). The growth of the cusp for the GC has been studied with numerical simulations from Antonini et al. (2012) with massive globular clusters spiraling into the center of a galaxy and merging to form the nucleus. After the final inspiral was complete, the core was observed to shrink as the stellar density evolved toward a Bahcall Wolf cusp.

1.2.2 Dynamical structure & kinematics of the NSC

Extensive dynamical modeling of the NSC and the surrounding NSD has become possible with the observation of several thousand proper motions and radial velocities (e.g. Trippe et al., 2008; Schödel et al., 2009). The ultimate goal of the dynamical modeling of a stellar system (in this case the NSC) is the successful prediction of the observed surface density distribution and the observed 3d VPs and thereby also of unobservable parameters such as the mass distribution or the intrinsic anisotropies. This is because the VPs contain information of all the moments of a distribution function (see also section 1.5). Additionally the recovery of the distribution function ensures the self consistency of the system (in simple words, that the model is a manifestation of a real system).

Initially the NSC was modeled as an isotropic spherical system aligned with the galactic plane and with the same sense of rotation. We note here that it is possible to add rotation to a spherical system self consistently by reversing the sense of rotation of some or all of its stars (Lynden Bell, 1960). Trippe et al. (2008) obtained the proper motions for 5445 stars using NAOS/CONICA and SINFONI instruments at the VLT. Using those data they derived a statistical parallax for the GC of $R_0 = 8.07 \pm 0.32|_{stat} \pm 0.13|_{syst}$ kpc. Additionally by applying spherical Jeans equation to the data they estimated a black hole mass $M_{BH} \simeq 1.2 \times 10^6 M_\odot$ contrary to the canonical $M_{BH} \simeq 4.0 \times 10^6 M_\odot$ estimated from the orbits (Schödel et al., 2002, 2003; Eisenhauer et al., 2005; Gillessen et al., 2009). Schödel et al. (2014) measured the proper motions of more than 6000 stars within ~ 1.0 pc of Sgr A*. They modeled the NSC non-parametrically as an isotropic and anisotropic spherical system, solving Jeans equations. Their best-fit black hole mass was $M_{BH} \simeq 3.6_{-0.4}^{+0.2} \times 10^6 M_\odot$ much closer to the expected value. Their modeling gave a stellar mass within the innermost pc of $1.1 \times 10^6 M_\odot < M(< 1pc) < 1.5 \times 10^6 M_\odot$.

An interesting problem that emerged from the observed proper motions was the bell-like shape of the VPs in b direction and the characteristic 2-peak shape of the VP in the l

direction (e.g. Trippe et al., 2008; Schödel et al., 2010; Fritz et al., 2011). This is shown in Fig.1.3. Trippe et al. (2008) considered the 2-peak shape as a sign of rotation. Schödel et al. (2010) tried to fit the VP in b direction to a Gaussian but the fit was not good.

One related unresolved question at that time was whether the NSC is flattened or not. Schödel et al. (2014) by combining imaging data from the IRAC/Spitzer GC survey (Stolovy et al., 2006) showed that the NSC is flattened with a ratio between minor and major axis of $q = 0.71 \pm 0.02$, and estimated a stellar mass of $M_* = 2.5 \pm 0.4 \times 10^7 M_\odot$. In Chapter 2 (Chatzopoulos et al., 2015) we calculate for the first time a self-consistent distribution function for the NSC of the form $f(E, L_z)$ providing also predictions for the VPs, using star counts and kinematic data from Fritz et al. (2014), including 2500 line-of-sight velocities and 10000 proper motions obtained with VLT instruments. First we approximated the NSC as a two component γ model (Tremaine et al., 1994). The first component represents the NSC and has a flattening of $q = 0.73 \pm 0.04$ inferred from star counts and also consistent with the observed kinematics. The second much more flattened component with $q = 0.28$ represents the NSD. Then we calculated the DF of the form $f(E, L_z)$ using the algorithm from (Qian et al., 1995). The DF provided a prediction of the VPs in every direction and showed that the characteristic 2-peak shape of the VPs in l direction is a result of a flattened NSC.

Recently it was suggested that there is a misalignment (Feldmeier et al., 2014; Fritz et al., 2014) of the radial velocity data about $\sim 10^\circ$ to the galactic plane. However this cannot be confirmed for the proper motions (Fritz et al., 2014). In addition there are indications for a rotating substructure perpendicular to the Galactic plane at distance $\sim 20''$. If these findings are confirmed then they would support the merger scenario of the NSC.

In Chapter 2 we find that the NSC can be well approximated as an axisymmetric system of the form $f(E, L_z)$. An axisymmetric system with a DF of the form $f(E, L_z)$ is an isotropic rotator when all three eigenvalues of the dispersion tensor are equal (Binney & Tremaine, 2008). The new data and modeling suggest (Fritz et al., 2014; Chatzopoulos et al., 2015) that the NSC is very close to an isotropic rotator up to $\sim 30''$ and close enough up to $\sim 200''$ with some tangential anisotropy outwards of $30''$.

In Chapter 3 (Chatzopoulos et al., 2015b) we continue the modeling of the NSC by giving a 2^{nd} order description of the VP in l direction. When inspecting the VPs in l direction it is noticeable that the right peak is slightly higher than the left (e.g. Trippe et al., 2008; Schödel et al., 2010; Fritz et al., 2011). This means that seemingly there are more stars in the front of the cluster (positive velocities) than in the back. In addition we give evidence based on photometry and on proper motion data that the observed asymmetry could be a result of dust within the NSC. The measured extinction variation along line-of-sight based on modeling of the dust in conjunction with the $f(E, L_z)$ model is about $A_K = 0.4$. Additionally the photometry data show a weak correlation between the mini-spiral and the dust within the NSC especially with the Western Arc.

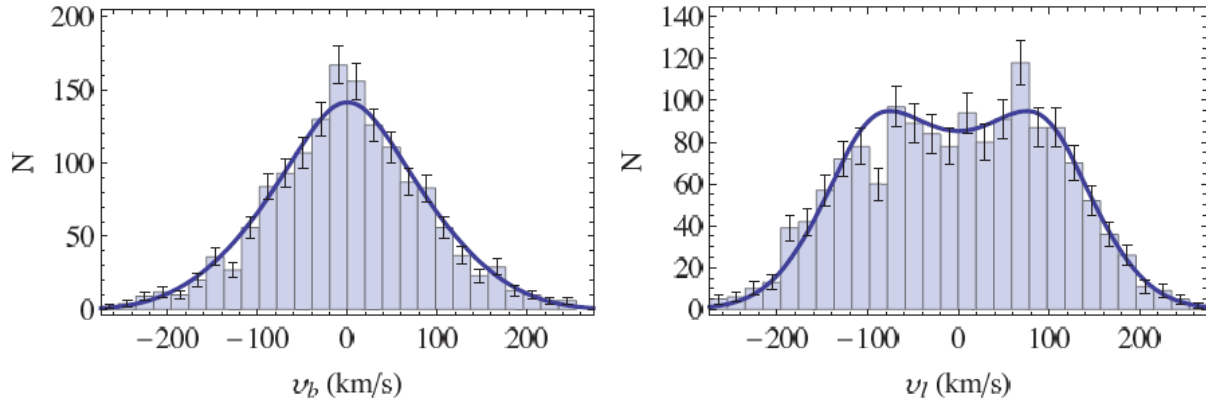


Figure 1.3: This is a sample from chapter 2 that shows the typical shape of the VPs in l and b direction of the NSC. The histograms show the data and the lines show the corresponding modeling from Chapter 2. The characteristic 2-peak shape of the VPs in l direction comes from the flattening of the NSC.

1.3 The Milky Way as a disk galaxy

The key properties of disk galaxies, also commonly called spiral galaxies, are that they are thin, rotate rapidly, and often show spiral structure. A disk galaxy consists of three basic components of visible matter: The disk, the bulge and the stellar halo. We dedicate the rest of this Section to a brief introduction of each one of these components.

1.3.1 The Galactic Disk

The Milky Way's dominant stellar component is the disk since it contains about three quarters of all Galactic Stars (Rix & Bovy, 2013). The Milky Way's disk is usually considered to have two major baryonic components: a thin disk and a thick disk (Gilmore & Reid, 1983). The total density of the disk can be approximated with (Binney & Tremaine, 2008):

$$\rho_d(R, z) = \Sigma_d e^{-R/R_d} \left(\frac{\alpha_0}{2z_0} e^{-|z|/z_0} + \frac{\alpha_1}{2z_1} e^{-|z|/z_1} \right) \quad (1.2)$$

where the first and second terms in the parenthesis represent the thin and thick disk respectively and $\alpha_0 + \alpha_1 = 1$, z_0, z_1 are the scale heights, R_d the scale length and Σ_d central surface density. Its total mass is given by $M_d = 2\pi\Sigma_{d,0}R_d^2$. The stellar mass of the disk's thin component is $m_D \simeq 5 \times 10^{10} M_\odot$ while the mass of the thick component is 10 – 20% of that of the thin disk (McMillan, 2011). Recent papers (e.g. Bovy et al., 2012) suggest larger fraction because the disk is more centrally concentrated which also challenges eq. 1.2. Its mass to light ratio M/L in B, V, I bands is $(M/L)_B = 1.4 \pm 0.2$, $(M/L)_V = 1.5 \pm 0.2$, $(M/L)_I = 1.2 \pm 0.2$ respectively (Flynn et al., 2006). The disk is

a highly flattened structure with an exponential radial scale length of 2.3-3 pc and scale height of $z_0 = 0.3$ kpc for the thin component and $z_1 = 0.9$ kpc for the thick component (Juric et al., 2008; McMillan, 2011). All disk stars orbit in the same direction of rotation, with a small amount of vertical motion. The Galactic disk can be characterized as cold because the stellar velocity dispersions near the sun are $\sigma_z \simeq \sigma_\phi \simeq \sigma_R/1.5 \simeq 25\text{kms}^{-1}$ (Dehnen & Binney, 1998), much smaller than the circular velocity $v \simeq 220\text{kms}^{-1}$. Younger and/or more metal-rich stars tend to be on more nearly circular orbits with lower velocity dispersions. The Sun is only 25 pc above the mid-plane (Juric et al., 2008).

The formation of the disk depends strongly on the amount of angular momentum present in the collapsing gas. The initial angular momentum is believed to have cosmological origin. This is because in the early phase of proto-galactic collapse the gas and the dark matter were mixed and therefore had a similar angular momentum distribution (Fall & Efstathiou, 1980). As the gas cools, it loses energy and sinks deeper into the potential well of the halo. However gas cannot easily lose its angular momentum. The gas with low angular momentum falls into the inner region and supports the formation of the galactic nucleus, the central black hole and perhaps a classical bulge, and additionally forming stars at small radii. In contrast the gas with high angular momentum forms the disk. Whether the angular momentum is truly conserved during the in-fall can be seen from the relation between the resulting disk size and the specific angular momentum λ' of the surrounding dark halo. where:

$$\lambda' = \frac{J}{\sqrt{2}M_{vir}V_{vir}R_{vir}} \quad (1.3)$$

Where R_{vir} , $V^2 = GM_{vir}/R_{vir}$, M_{vir} are the virial radius, virial velocity and virial mass of the dark halo (Bullock et al., 2001). This relation when plotted against the data confirms the cosmological origin of the angular momentum however it seems that some amount of angular momentum is lost during the process (Bullock, 2009). After the disk forms, secular disk evolution becomes important on timescales longer than the infall timescale (Mo et al., 1998).

1.3.2 The Galactic Bulge

In addition to the disk, the Milky Way contains a tightly packed group of stars that is thicker than the disk and comprises $\sim 15\%$ of the total luminosity (Binney & Tremaine, 2008), called a bulge.

The Galactic bulge in contrast to the Galactic center can be observed in the optical. The bulge extends to 10° from the plane where the extinction even in the optical is not so high. The Galactic bulge is dominated by a globular cluster-age, metal-rich stellar population (Rich, 2013). The majority of those metal-rich stars are old with an age of $t = 10 \pm 2.5$ Gyr (Zoccali et al., 2003) a value that has been obtained by comparison of bulge fields with metal-rich globular clusters.

Until recently there was some dispute about whether the Galactic bulge is a classical bulge or a box/peanut (pseudo) bulge. A classical bulge has properties similar to elliptical galaxies and forms through merging of smaller structures while a pseudo-bulge refers to the slow dynamical evolution due to internal processes and interactions with other components like the disk, spiral arms etc. Recent studies suggest that the Galactic bulge resembles mostly a box/peanut bulge with a small classical bulge component of less than 20% by mass (Martinez-Valpuesta & Gerhard, 2011; Wegg & Gerhard, 2013).

The inner MW can be separated (not certain though) into three components that are common to many barred spiral galaxies (Kormendy, 2013). The main component is a box/peanut bulge shape structure with ~ 300 pc vertical scale and $|l| < 10^\circ$, that also contains most of the bulge mass $\sim 1.84 \pm 0.07 \times 10^{10} M_\odot$ (Portail et al., 2015). The second structure with $|l| > 10^\circ$ is a thin structure with mass $\sim 2 \times 10^9 M_\odot$ and is called the long bar with ~ 180 pc scale height (Wegg et al., 2015). The length of the bar is about ~ 5 kpc although still far from certain (López-Corredoira et al., 2007; Wegg et al., 2015) with axes ratios 1:0.35:0.26 (Rattenbury et al., 2007). The near side of the bar is at positive Galactic longitude with angle $\sim 28 - 33^\circ$ (Wegg et al., 2015). Fig. 1.4 shows the geometry of this structure. Whether the long bar is separable from the box/peanut component is still debatable. The third structure is a nuclear bar or disk of extent ~ 100 pc with mass similar to the long bar (Launhardt et al., 2002).

The bulge kinematics are intermediate between a purely rotating system such as the Milky Way disk and a hot, non-rotating system like the Milky Way halo, that is supported by velocity dispersion (Minniti & Zoccali, 2007). The corotation of the bar is about halfway between the Galactic center and the Sun. The rotation of the bar component has been calculated from the relative velocity of OH/IR stars. The resulting value of the pattern speed after adding the circular velocity at the local standard of rest is $59 \pm 10 \pm 5(\text{sys}) \text{kms}^{-1} \text{kpc}^{-1}$ for $R_0 = 8$ kpc and $V_0 = 220 \text{kms}^{-1}$ (circular velocity of the Sun) (Gerhard, 2010). According to the previous value the galactic bar is a fast rotator, however recent estimates (Portail et al., 2015) using dynamical modeling imply a much lower $25 - 30 \text{kms}^{-1} \text{kpc}^{-1}$ pattern speed.

1.3.3 The Stellar Halo

The third luminous and probably the oldest component of the Milky Way is the stellar halo. It is comprised of metal-poor globular clusters and field stars. Approximately 150 globular clusters and about 20 satellite galaxies are located in the Stellar halo (Helmi, 2008). With mass $\sim 10^9 M_\odot$ (Morrison, 1993) the stellar halo contains about 1% of the total mass of the Galaxy. The age of the halo can be estimated from the very metal-poor stars near the solar-neighborhood which have ages of 14 ± 3 Gyr (Hill et al., 2002) and 13.2 Gyr (Frebel et al., 2007).

The density of the stellar halo can be approximated with:

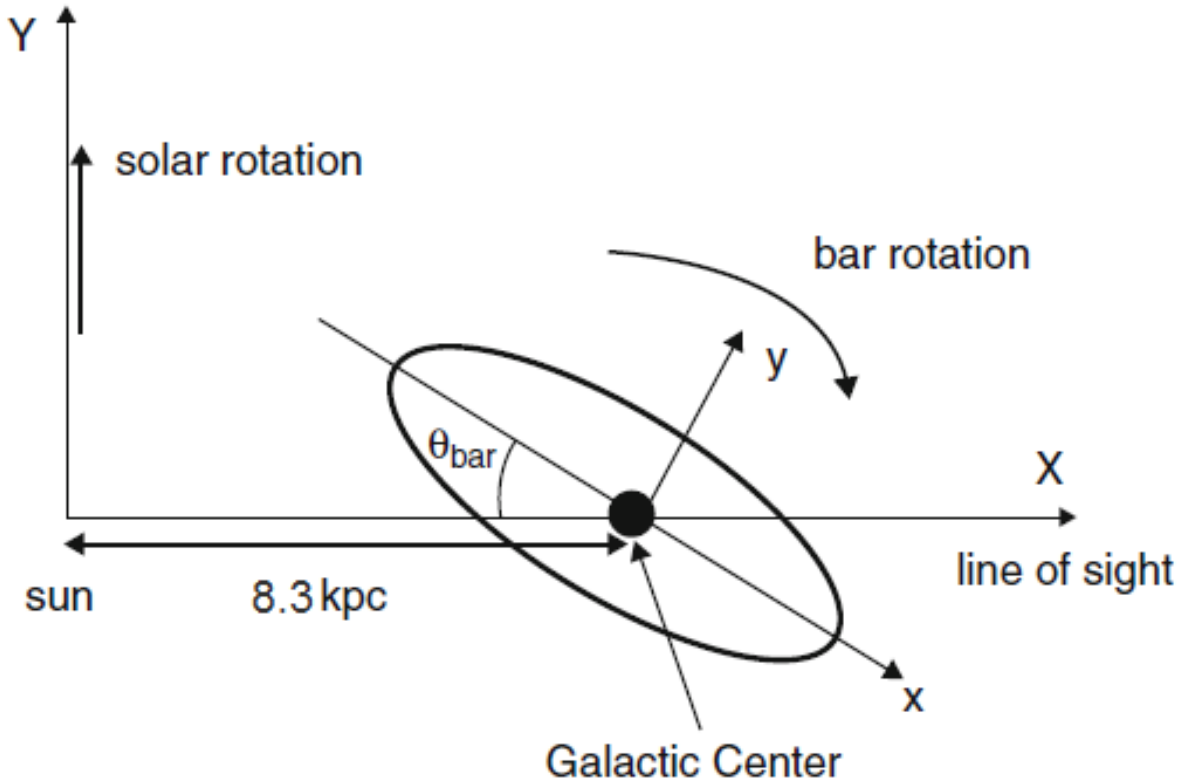


Figure 1.4: The bar geometry and its rotation. The near side of the bar is at positive Galactic longitude with angle $\theta_{bar} \sim 28 - 33^\circ$. The distance is based on the recent estimate from Chapter 2. (adapted from Rich, 2013).

$$\rho(x, y, z) = \rho_0 \frac{(m^2 + a^2)^n}{r_0^n} \quad (1.4)$$

where $m^2 = x^2 + y^2/p^2 + z^2/q^2$, is the triaxial radius ($p = 1$ for axisymmetric), q and p are the minor and intermediate-to-major axis ratios, n is the power-law exponent and has value about $n \sim -2.7$ while $q \sim 0.7$ (e.g., Siegel et al., 2002). The normalization factor ρ_0 is the stellar halo density at distance R_0 which is usually the Sun's galactocentric distance (~ 8 kpc) and is close to $\rho_0 \sim 10^{-4}$ (Fuchs & Jahreiß, 1998; Gould & Flynn, 1998).

The stellar halo shows little sign of rotation and its angular momentum is close to zero in contrast to the disk and the bulge (e.g., Freeman et al., 1987). Specifically solar-neighborhood halo stars show a small prograde rotation $V_\phi \sim 30 - 50 \text{ km s}^{-1}$ (Chiba & Beers, 2000) while there is no strong correlation of rotation with metallicity. Thus the halo is supported almost entirely by its velocity dispersion having a radially elongated velocity ellipsoid $(\sigma_R, \sigma_\phi, \sigma_z) = (141 \pm 11, 106 \pm 9, 94 \pm 8) \text{ km s}^{-1}$ (Chiba & Beers, 2000). However some of its stars are very energetic, reaching out to at least 100 kpc from the galactic center (e.g. Carney et al., 1990).

The metal-poor halo of the Galaxy is very interesting for galaxy formation studies because it is so old: Most of its stars are probably older than 12 Gyr and were probably among the first galactic objects to form (Freeman et al., 2002). There are two available scenarios for the formation of the Galactic halo introduced in the 1960s and 1970s. According to the first one (Eggen & Lynden-Bell., 1962) about 10 Gyr ago the protogalaxy consisting of gas started to fall radially into the center. As the gas fell, condensations formed which were later to become globular clusters. The collapse was very rapid and only $\sim 10^8$ years were required for the gas to attain circular orbits in equilibrium. The second scenario Searle & Zinn (1978) which is now considered the most probable one is based on the fact that there is a lack of radial abundance gradient in the clusters of the halo and these formed in a number of small protogalaxies that subsequently merged to form the present Galactic halo.

1.4 Nuclear star clusters in external disk galaxies

Nuclear star clusters (NSC) exist in the centers of the majority of spiral galaxies of all Hubble types. NSCs are very interesting since several of the most extreme physical phenomena take place within them such as super-massive black holes, active galactic nuclei, star-bursts and extreme stellar densities. Their detection is difficult because it requires high spatial resolution observations that currently are only possible with Hubble Space Telescope (HST) or with very large ground telescopes. Several surveys have been conducted for their detection. Carollo et al. (1998) conducted an analysis of HST/WFC images of 40 early type spiral galaxies (Sa-Sc). They detected central compact sources in about 50% of these galaxies. Böker et al. (2002) acquired new HST I-band images of a sample of 77 nearby late-type spiral galaxies (Scd-Sm) with low inclination. They detected compact central sources in 77% of the sample. Later Côté et al. (2006) revised upward the frequency of NSCs in early type galaxies. By using the ACS Virgo cluster survey program of the HST they obtained high resolution imaging of 100 early-type galaxies (E & S0) of Virgo cluster. They resolved NSCs in about 66% – 82% of the sample but they had no detections in the most luminous giant ellipticals. We note that early type galaxies have much steeper surface densities which makes the detection of NSCs exceedingly difficult.

NSCs share some similarities with globular clusters but also have important differences. Their effective radii typically range from 2 to 10 pc. About 50% of them have effective radius about 2.4 – 5 pc (Rossa et al., 2006) and this makes them as compact as MW globular clusters. Their luminosities typically range from 10^5 to $10^8 L_\odot$ which is on average 4 mag brighter than the old globular clusters with total I-band magnitudes in the range of –8 to –12 mag for the NSCs Böker et al. (2004). The high luminosities are partly because of their young star populations. In general the abundance ratios $[\alpha/Fe]$ of NSCs is lower than globular clusters (Evstigneeva et al., 2007) and therefore they are more metal enriched. With typical dynamical masses of $10^6 - 10^7 M_\odot$ (Walcher et al., 2005), NSCs are much more massive than typical globular clusters and they are the densest stellar systems in the Universe. This is clear in Fig. 1.5 where is plotted the mean projected mass density inside the effective radius against the total mass for various stellar systems where it is

apparent that NSC follow the same scaling relationship with globular clusters and they scale totally differently than bulges.

In general, several NSCs seem to be flattened. Seth et al. (2006) found that three out of nine NSCs that belong to late-type galaxies observed with the HST/ACS were flattened and could fit well with a combination of a spheroid and a disk or ring. Their median axis ratio is 0.81, with $q \sim 0.4$ for NGC 4206 and NGC 4244. This is consistent with the NSC of the MW which is found to be flattened with $q \sim 0.73$ (Schödel et al., 2014; Chatzopoulos et al., 2015) consistent also with the kinematic data as shown in Chapter 2.

The available formation scenarios of NSCs can be split into two main categories: a) The merger scenario where several dense globular clusters migrate close to the center from the outskirts via dynamical friction (Tremaine & Ostriker, 1975) and merge to form a compact stellar system. b) The 'in situ' episodic buildup scenario where stars form locally from in-falling gas towards the center (Schinnerer et al., 2008; Bonnell & Rice, 2008). Next we give more details for each one.

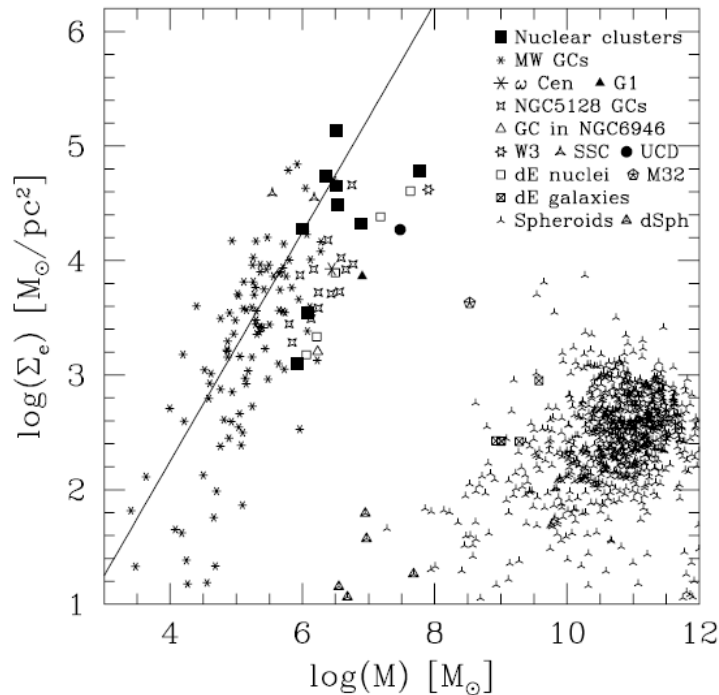


Figure 1.5: Mean projected mass density inside the effective radius against the total mass for various stellar systems. The NCS follow the same scaling as the MW globular clusters although they are much more massive. The scaling of the NSC differs significantly from the spheroids. From Walcher et al. (2005)

The first evidence that a NSC can be formed from in-falling globular clusters came from observations of the nucleus of M31 galaxy in 1975 using a stratosphere balloon. Tremaine & Ostriker (1975) were the first to propose that the nucleus of M31 was grown from the nearby globular clusters spiraling towards the center where they were tidally disrupted by

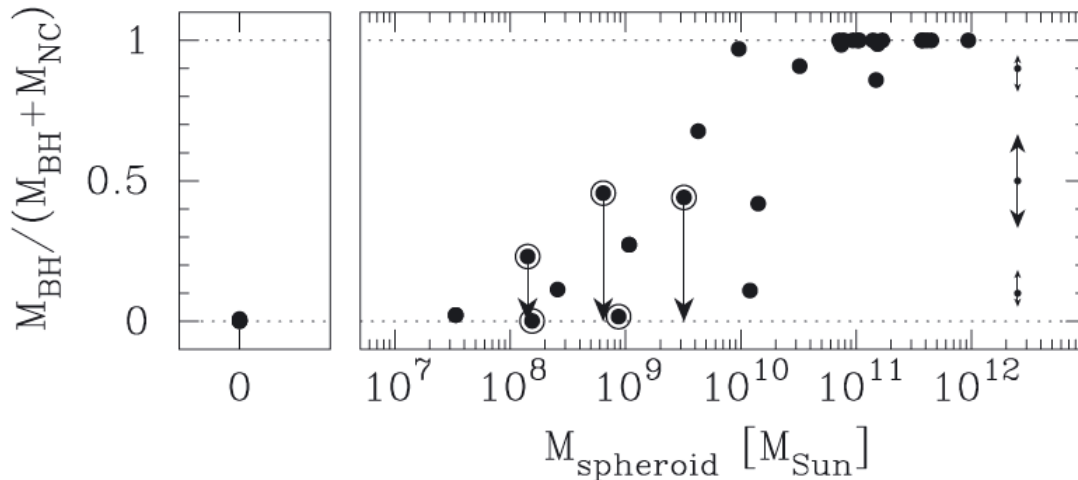


Figure 1.6: The prevalence of the central BH is increasing over the NSCs and is traced by the mass ratio $M_{BH}/(M_{BH} + M_{NSC})$ which appears to depend on the bulge mass M_{sph} of the host galaxy. The spheroids with the highest mass do not contain an NSC. The points with circles have only an upper limit to their BH mass. From Graham & Spitler (2009)

interactions from the growing nucleus. Dynamical friction (Chandrasekhar, 1943) which is the loss of momentum and kinetic energy of a massive body (e.g. globular cluster) moving within a gravitational field generated from several lighter stars, plays an important role in this scenario. By this process the nucleus of M31 with mass of $\sim 5 \times 10^7 M_{\odot}$ can be formed within 10^{10} years. Lotz et al. (2001) examined high resolution images from HST of dE elliptical galaxies seeking for evidence of dynamical friction. By doing Monte Carlo simulations, taking into account also the radial orbital decay from dynamical friction they found that the brighter nuclei may have been formed from the orbital decay of massive clusters. Antonini et al. (2012) investigate the merger scenario by doing N-body simulations for the Galactic NSC. Their simulation starts with several globular clusters in circular orbits at a distance of 20 pc from the center. The clusters decay orbitally in the central region and finally are being disrupted by the SMBH at a distance about ~ 1 pc. At the end of their simulation they find that the formed system has properties similar to the Milky Way NSC, with the exception of the core size, which in the Milky Way is somewhat smaller. By continuing the evolution further they find that the system evolves towards the expected Bahcall - Wolf cusp. Feldmeier et al. (2014) find indications for a rotating substructure within the Milky Way NSC perpendicular to the Galactic plane at a radius 0.8 pc that could support the merger scenario.

The process of NSC formation through infalling gas in the nearby galaxies has been studied recently based on some qualitative millimeter interferometric observations (Schinnerer et al., 2006, 2007) of the CO(1 – 0) and CO(2 – 1) line emission in the central 300 pc of the late-type spiral galaxy NGC 6946. According to this scenario a prolonged influx of molecular gas into the central few pc might take place originating from bar-shaped asymmetries in the disk potential leading to an intense star-burst. However supernova ex-

plosions can expel the remaining gas and even temporarily change the gas inflow resulting in a self-regulating starburst mechanism (Schinnerer et al., 2008).

There is a well known correlation between the black hole mass and bulge luminosity known as $M_{BH} - \sigma$ relation (Ferrarese & Merritt, 2000) which implies a strong link between black hole formation and the properties of the stellar bulge. NSCs seem to obey similar scaling-relations (Ferrarese et al., 2006; Wehner & Harris, 2006) with host galaxy properties as do central supermassive black holes. This is possibly an indication of a common formation mechanism between NSCs and SMBHs. Graham & Spitler (2009) have identified all galaxies with reliable measurements of both NSC mass and SMBH mass. They conclude that the ratio $M_{BH}/(M_{BH} + M_{NSC})$ is a function of bulge mass. This relation is shown in Fig. 1.6. For very large bulges the mass of the black hole is also large but there is a lack of NSC. On the contrary for very small bulges the mass of the SMBH is negligible with respect to the NSC mass.

1.5 Dynamical modeling of Collision-less systems

In Section 1.2 we summarized the main characteristics of the old nuclear star cluster in the Milky Way and in the Section 1.4 we focused on external nuclear clusters and the available formation models. In this Section we examine the methods that can be used to model a nuclear star cluster assumed to be a collisionless system in equilibrium.

1.5.1 The collisionless Boltzmann equation

When we model an astrophysical system like a nuclear star cluster or a galaxy we have to deal with several thousands up to billions of stars. Therefore as in statistical mechanics we need a way to describe the system's macroscopic behavior without focusing on the orbits of individual stars (or molecules of a gas or particles). When we work with a stellar system in equilibrium that possess an adequate number of stars, the system's mass can be considered smoothly distributed in space rather concentrated into point-like stars and close encounters between stars are unimportant. In such a system the potential is approximately smooth. A quantitative way to describe this is the relaxation time (e.g. Binney & Tremaine, 2008). The relaxation time t_{relax} , is the time taken for a star's velocity v to be changed significantly by two-body interactions. When the t_{relax} is much larger than the dynamical time t_{dyn} (i.e. typical orbital period) then we say that the system is collisionless and interactions between stars (or particles) are not important. On the contrary we say that the system is collisional. In this section we focus on collisionless systems in equilibrium.

In order to describe the macroscopic state of a collisionless system we define the distribution function (DF) $f(\vec{x}, \vec{v}, t)$ that depends on phase space coordinates and time. The DF is the probability that at time t a randomly chosen star, has space coordinates in the given range (Binney & Tremaine, 2008). From the definition it follows that a valid DF should always be positive. Since the DF is a probability function the following normalization relation holds.

$$\int f(\vec{x}, \vec{v}, t) d^3\vec{x} d^3\vec{v} = 1 \quad (1.5)$$

For a system in equilibrium, the phase-space density f of the fluid around a given star always remains the same therefore the total time derivative of the DF should be zero.

$$\frac{df}{dt} = 0 \quad (1.6)$$

This equation is called the collisionless Boltzmann equation. Assuming cartesian coordinates and expanding the total derivative we get the following form:

$$\frac{\partial f}{\partial t} + \vec{v} \cdot \frac{\partial f}{\partial \vec{x}} - \frac{\partial \Phi}{\partial \vec{x}} \cdot \frac{\partial f}{\partial \vec{v}} = 0 \quad (1.7)$$

A generalization of the collisionless Boltzmann equation is the following:

$$\frac{df}{dt} = B - D \quad (1.8)$$

where $B(\vec{x}, \vec{v}, t)$ and $D(\vec{x}, \vec{v}, t)$ are the rates per unity phase space volume at which stars are born and die. In the collisionless Boltzmann equation, $B - D$ is set to zero.

One important concept of mechanics is the integral (or constant) of motion which is a quantity that is conserved throughout the motion of a particle or star. It can be easily shown (e.g. Binney & Tremaine, 2008) that an integral of motion is a steady-state solution of the collisionless Boltzmann equation. This leads to the Jeans theorem:

Jeans theorem: *Any steady-state solution of the collisionless Boltzmann equation depends on the phase-space coordinates only through integrals of motion in the given potential, and any function of the integrals yields a steady-state solution of the collisionless Boltzmann equation.*

The Jeans theorem is an important theorem of stellar dynamics because in several cases it allows us to express the DF of a stellar system as a function of its integrals of motions instead of phase-space coordinates. In addition it can lead to intuitive solutions of the Boltzmann equation.

All the available methods used to solve the collisionless Boltzmann equation fall into two categories, numerical methods and analytic (or semi-analytic) ones. The numerical methods are split in orbit and particle methods. The advantages of a numerical method over an analytic one is that it can be more general (e.g. it can even be used to model triaxial system) and it is relatively simpler to implement. One disadvantage is that often it suffers from large errors due to particle noise. For example the modeling of the core of a system

with a particle method is always problematic since only a very small percentage of particles reside close to the center and this results in large errors in the modeled quantities. Another important disadvantage is that the results of a particle based algorithm often depend on implementation details containing underlying assumptions that are difficult to be tested. In other words, unfortunately it is not unlikely two independent codes based on the same method would give different solutions of a problem. In the contrary analytic methods are always smoother, more elegant and they can be tested easier. In my opinion, particle methods should only be used when an analytic method is unavailable for a specific problem. Next follows a very brief introduction to both categories.

1.5.2 Orbit-based and Particle-based methods

One powerful orbit-based technique for constructing the DF of a system in equilibrium was introduced by Schwarzschild (1979). Specifically Schwarzschild devised a simple and yet very useful algorithm to construct a model of a galaxy in equilibrium with a given three-dimensional density distribution $\rho(\vec{x})$ using linear programming technique (Kantorowitsch, 1948). The general steps to apply this method are: (i) We start from an observed surface brightness distribution (SB) which we have to deproject to obtain the 3d density distribution. The deprojected 3d density can be acquired algorithmically (e.g. Magorrian, 1999) or by fitting the data to the projected function of a known parametric model e.g. the family of γ -models (Tremaine et al., 1994). (ii) We integrate the 3d density to calculate the potential. (iii) Once we have the potential we integrate many orbits and generate an orbit library that samples all the phase space that is likely to be occupied by the galaxy. (iv) Finally we construct a model of the observed system using a suitable superposition of the orbits in the orbit library according to the observed quantities (e.g. kinematics and SB).

Now I describe steps (iii) and (iv) in more detail (based on Binney & Tremaine, 2008). We start with a galaxy that has known 3d density $\rho(\vec{x})$. We then partition the space that is occupied by the galaxy into K cells, such that the mass in the j th cell of volume V_j is $m_j = \rho(\vec{x})V_j$. Then we create a library of usually several thousand of orbits choosing carefully the initial conditions so that they sample all the phase space occupied by the galaxy. This set of orbits is called the orbit library. Then we integrate the N orbits of the orbit library in the potential for a period much larger than the crossing time of the galaxy and for each orbit we store the fraction p_{ij} of the time t that the i th orbit spends in the j th cell. The total mass of the galaxy is M and each one of the N orbits contributes $w_i M$ to the total mass where w_i where w_i is an unknown weight. The goal of Schwarzschild's technique

is to constrain the N weights w_i by solving the following set of K linear equations.

$$\begin{aligned} 0 &= m_j - M \sum_{i=1}^N w_i p_{ij} \\ \sum_i w_i &= 1 \\ w_i &\geq 0 \\ \varphi(\vec{w}) &= \sum_i \varphi_i w_i \end{aligned} \tag{1.9}$$

The first of eq. 1.9 is the linear system to be solved. The second and third are additional constraints that come from the normalization of mass $\sum_i m_j = 1$ and to ensure positive solutions for the weights. The fourth equation is an additional constraint that we put in order to limit the infinite set of possible solutions which we do by choosing the solution that maximizes some objective function $\varphi(\vec{w})$. After we solve the system 1.9 through linear programming we can construct the DF that is a solution to the Boltzmann equation for this system as a sum of delta functions with weights w_i . For example for a spherical anisotropic function the DF takes the form (Binney & Tremaine, 2008):

$$f(E, L) = \sum_{i=1}^N w_i f_i, \quad f_i(E, L) = \delta(E - E_i) \delta(L - L_i) \tag{1.10}$$

where E and L are the energy and the angular momentum integrals of motion respectively.

A particle-based or Made-to-measure (M2M) algorithm is similar to an orbit-based method except that instead of orbits we work with individual particles. Probably the most characteristic particle-based method is the algorithm introduced by Syer & Tremaine (1996) (ST96). Here we outline this method since all other particle-based methods in the literature are variations based on it.

An observable of a stellar system is a quantity defined as:

$$Y_j = \int K_j(\vec{z}) f(\vec{z}) d^6 \vec{z} \tag{1.11}$$

where $\vec{z} = (\vec{x}, \vec{v})$ are the phase space coordinates, $f(\vec{z})$ is the DF that satisfies the collisionless Boltzmann equation and K_j is a known kernel. The observables can be any moment of the DF, e.g. the 3d or surface density the mean line-of-sight velocity, dispersions etc. Now suppose that we have a system of N particles each of them having a weight w_i and phase-space positions $z_i(t)$. For this discrete system the observables are:

$$y_j(t) = \sum_{i=1}^N w_i K_j[z_i(t)] \tag{1.12}$$

where the kernels $K_j[z_i(t)]$ are the same functions as before. The goal of the algorithm is to match the observables of the observed system with those of the particle system. To do this we integrate the particles along their fixed orbits in the potential $\Phi(\vec{x})$ that matches that of the stellar system. As in Schwarzschild's method the potential can be calculated from the surface density of the observed system or come from the particles directly. The weights w_i of the particles are updated along their fixed orbits according to the value $\Delta_j(t) = y_j(t)/Y_j - 1$. Specifically if $\Delta_j(t) < 0$ the weights are increased otherwise they are decreased according to:

$$\frac{dw_i(t)}{dt} = -\epsilon w_i(t) \sum_{j=1}^J \frac{K_j[z_i(t)]}{Z_j} \Delta_j(t) \quad (1.13)$$

where ϵ is a small quantity and Z_j is arbitrary for now. This is in principle a linear system of differential equations. The factor w_i on the right side ensures that $dw_i/dt \rightarrow 0$ as $w_i \rightarrow 0$, so that w_i is always positive. After the convergence of the weights we are left with a particle system that is similar to the observed one and which is also a discrete solution of the Boltzmann equation of the observed system. As in Schwarzschild's method the system 1.13 is ill-conditioned since the number of particles exceeds the number of observables. To remove the ill-conditioning ST96 maximized some form of profit function that favors smoothness, such as the entropy $S = -\sum_i w_i \log(w_i/m_i)$ where m_i is a predetermined set of weights. Thus we maximize the function

$$F = \mu S - \frac{1}{2} \chi^2 \quad (1.14)$$

where

$$\chi^2 = \frac{1}{J} \sum_{j=1}^J \Delta_j^2 \quad (1.15)$$

Finally eq. 1.13 is replaced with:

$$\frac{dw_i(t)}{dt} = -\epsilon w_i(t) \left[\mu \frac{\partial S}{\partial w_i} - \sum_{j=1}^J \frac{K_j[z_i(t)]}{Z_j} \Delta_j(t) \right] \quad (1.16)$$

where now $Z_j = Y_j$ by the requirement of eq. 1.14. The constant μ defines the contribution of the entropy term.

1.5.3 Analytic methods

Analytic methods are more robust and more accurate than numerical methods but their main disadvantage is that they are not as general. Again the goal here is to find the partial

(e.g. a number of moments) or the total solution to the collisionless Boltzmann equation that corresponds to the observed system. Analytic methods can be split in two categories. First is Jeans modeling where we try to retrieve some moments of the DF (therefore partial solution) and second is the recovery of the DF (total solution).

We start with Jeans modeling. The simplest case is when the DF depends only on energy E integral and the system is called isotropic. In that case the $0th$ moment of the $f(E)$ is the density of the system. We assume as before that the potential of the system is known from the surface density. The first moments of $f(E)$ can be easily shown to be zero (e.g. Binney & Tremaine, 2008). The second moments are the dispersions which are equal in all directions since the velocity-dispersion tensor is isotropic: $\sigma_{ij}^2 = \overline{v_i v_j} = \sigma \delta_{ij}$ where:

$$\sigma^2(\vec{x}) = \frac{4\pi}{3\rho(\vec{x})} \int_0^\infty dv v^4 f\left(\frac{1}{2}v^2 + \Phi\right) \quad (1.17)$$

Expressions for higher moments can be retrieved similarly by integrating the DF.

The next simplest case is when the DF depends on the energy E and the angular momentum integral $L = |\vec{L}| = rv_t$, where r is the spherical distance and v_t is the tangential velocity, so $v_t^2 = v_\theta^2 + v_\varphi^2$ in spherical coordinates. In this case again the first moments are zero and the system is called spherical anisotropic. For the second moments we have $\sigma_\varphi^2 = \sigma_\theta^2 \neq \sigma_r^2(r)$ and suitable expressions can be found. In this case the Jeans equation takes the form:

$$\frac{d(\overline{\rho v_r^2})}{dr} + 2\frac{\beta}{r}\overline{\rho v_r^2} = -\rho \frac{d\Phi}{dr} \quad (1.18)$$

where β is the anisotropy parameter. We note that in this case eq. 1.18 are not closed in the sense that $\overline{v_r^2}$ and β cannot both be determined from ρ and Φ . For $\beta = 0$ we get the Jeans equation for the spherical isotropic case.

If we relax more the restrictions even more we get the next most complicated DF which depends on E and L_z which is the angular momentum component in the z direction. This system is a flattened one. In this case we can find expressions for the moments of the system by integrating a cylindrical form of the Jeans equation (Binney & Tremaine, 2008). In the second chapter of this work (Chatzopoulos et al., 2015) we use the corresponding Jeans equations to fit the proper motion and line-of-sight velocity dispersions for the mass, the black hole mass and the distance of the nuclear star cluster. For systems of the form $f(E, L_z)$ it is possible to find recursive expressions for any moment of the distribution function Magorrian & Binney (1994).

Even though systems of the form $f(E, L_z)$ are flattened, they are still called semi-anisotropic because the anisotropy parameter defined as $\beta_z = 1 - \overline{v_z^2}/\overline{v_R^2}$ is zero. Cappellari (2008) (C08) presented a simple and efficient anisotropic generalization of the semi-isotropic axisymmetric Jeans modeling assuming that the β_z parameter is constant. The formalism presented in C08 provides the most general Jeans modeling in the literature up to now.

Jeans modeling is a useful method to recover information from an observed system, however it is always better to have the total DF for at least the following reasons (i) Jeans modeling does not ensure self-consistency, in other words it is possible to calculate moments that do not correspond to a positive DF. (ii) we cannot calculate velocity profiles since we do not have all the information (iii) we cannot make a particle model that could be the initial state for ever more general modeling (e.g. M2M). All these problems are solved when we have the DF of the system at our disposal. For a spherical isotropic system the DF can be easily be found from the density and corresponding potential through:

$$f(E) = \frac{1}{\sqrt{8\pi}} \frac{d}{dE} \int_0^E \frac{d\Psi}{\sqrt{E-\Psi}} \frac{d\rho}{\delta\Psi} \quad (1.19)$$

The result is due to Eddington (1916) and it is called Eddington's formula. There is no general Eddington's formula for spherical anisotropic systems but one can get similar expressions by assuming a specific form from anisotropy β (Osipkov, 1979; Merritt, 1985). More general expressions can be obtained e.g. by using the methodology of Gerhard (1991).

For axisymmetric systems that depend on E and L_z , the DF can be split in an even part with respect to L_z and a corresponding odd part $f(E, L_z) = f_+(E, L_z) + f_-(E, L_z) = (1 + g(L_z))f_+(E, L_z)$ where $g(L_z)$ is an odd function with $\max |g(L_z)| < 1$. The 3d density $\rho(r)$ is independent of f_- , while the azimuthal flux $\rho \bar{v}_\phi$ is independent of f_+ . Hunter & Qian (1993) generalized Eddington's formula to an integral on the complex plane that gives the expression for $f_+(E, L_z)$. In Chapter 2 we used this method with suitable $g(L_z)$ in order to calculate the $f(E, L_z)$ of the nuclear star cluster. Unfortunately analytic expressions for distribution functions similar to Eddington's formula more general than $f(E, L_z)$ are not available and in these cases we have to rely on potentials of specific form e.g. Stäckel potential family or on numerical methods such as those described in 1.5.2, or on action integrals.

Chapter 2

The old nuclear star cluster in the Milky Way: dynamics, mass, statistical parallax, and black hole mass

Original publication: S. Chatzopoulos, T.K. Fritz, O. Gerhard, C. Wegg, S. Gillessen, R. Genzel, O. Pfuhl

Abstract: We derive new constraints on the mass, rotation, orbit structure and statistical parallax of the Galactic old nuclear star cluster and the mass of the supermassive black hole. We combine star counts and kinematic data from Fritz et al. (2014), including 2'500 line-of-sight velocities and 10'000 proper motions obtained with VLT instruments. We show that the difference between the proper motion dispersions σ_l and σ_b cannot be explained by rotation, but is a consequence of the flattening of the nuclear cluster. We fit the surface density distribution of stars in the central 1000'' by a superposition of a spheroidal cluster with scale $\sim 100''$ and a much larger nuclear disk component. We compute the self-consistent two-integral distribution function $f(E, L_z)$ for this density model, and add rotation self-consistently. We find that: (i) The orbit structure of the $f(E, L_z)$ gives an excellent match to the observed velocity dispersion profiles as well as the proper motion and line-of-sight velocity histograms, including the double-peak in the v_l -histograms. (ii) This requires an axial ratio near $q_1 = 0.7$ consistent with our determination from star counts, $q_1 = 0.73 \pm 0.04$ for $r < 70''$. (iii) The nuclear star cluster is approximately described by an isotropic rotator model. (iv) Using the corresponding Jeans equations to fit the proper motion and line-of-sight velocity dispersions, we obtain best estimates for the nuclear star cluster mass, black hole mass, and distance $M_*(r < 100'') = (8.94 \pm 0.31)_{\text{stat}} \pm 0.9_{\text{syst}} \times 10^6 M_\odot$, $M_\bullet = (3.86 \pm 0.14)_{\text{stat}} \pm 0.4_{\text{syst}} \times 10^6 M_\odot$, and $R_0 = 8.27 \pm 0.09_{\text{stat}} \pm 0.1_{\text{syst}}$ kpc, where the estimated systematic errors account for additional uncertainties in the dynamical modeling. (v) The combination of the cluster dynamics with the S-star orbits around Sgr A* strongly reduces the degeneracy between black hole mass and Galactic centre distance present in previous S-star studies. A joint statistical analysis with the results of Gillessen et al. (2009) gives $M_\bullet = (4.23 \pm 0.14) \times 10^6 M_\odot$ and $R_0 = 8.33 \pm 0.11$ kpc.

2.1 Introduction

Nuclear star clusters (NSC) are located at the centers of most spiral galaxies (Carollo et al., 1997; Böker et al., 2002). They are more luminous than globular clusters (Böker et al., 2004), have masses of order $\sim 10^6 - 10^7 M_\odot$ (Walcher et al., 2005), have complex star formation histories (Rossa et al., 2006; Seth et al., 2006), and obey scaling-relations with host galaxy properties as do central supermassive black holes (SMBH; Ferrarese et al., 2006; Wehner & Harris, 2006); see Böker (2010) for a review. Many host an AGN, i.e., a SMBH (Seth et al., 2008), and the ratio of NSC to SMBH mass varies widely (Graham & Spitler, 2009; Kormendy, 2013).

The NSC of the Milky Way is of exceptional interest because of its proximity, about 8 kpc from Earth. It extends up to several hundred arcsecs from the center of the Milky Way (Sgr A*) and its mass within 1 pc is $\sim 10^6 M_\odot$ with $\sim 50\%$ uncertainty (Schödel et al., 2009; Genzel et al., 2010). There is strong evidence that the center of the NSC hosts a SMBH of several million solar masses. Estimates from stellar orbits show that the SMBH mass is $M_\bullet = (4.31 \pm 0.36) \times 10^6 M_\odot$ (Schödel et al., 2002; Ghez et al., 2008; Gillessen et al., 2009). Due to its proximity, individual stars can be resolved and number counts can be derived; however, due to the strong interstellar extinction the stars can only be observed in the infrared. A large number of proper motions and line-of-sight velocities have been measured, and analyzed with spherical models to attempt to constrain the NSC dynamics and mass (Haller et al., 1996; Genzel et al., 1996, 2000; Trippe et al., 2008; Schödel et al., 2009; Fritz et al., 2014).

The relaxation time of the NSC within 1 pc is $t_r \sim 10^{10}$ yr (Alexander, 2005; Merritt, 2013), indicating that the NSC is not fully relaxed and is likely to be evolving. One would expect from theoretical models that, if relaxed, the stellar density near the SMBH should be steeply-rising and form a Bahcall & Wolf (1976) cusp. In contrast, observations by Do et al. (2009); Buchholz et al. (2009); Bartko et al. (2010) show that the distribution of old stars near the SMBH appears to have a core. Understanding the nuclear star cluster dynamics may therefore give useful constraints on the mechanisms by which it formed and evolved (Merritt, 2010).

In this work we construct axisymmetric Jeans and two-integral distribution function models based on stellar number counts, proper motions, and line-of-sight velocities. We describe the data briefly in Section 2.2; for more detail the reader is referred to the companion paper of Fritz et al. (2014). In Section 2.3 we carry out a preliminary study of the NSC dynamics using isotropic spherical models, in view of understanding the effect of rotation on the data. In Section 2.4 we describe our axisymmetric models and show that they describe the kinematic properties of the NSC exceptionally well. By applying a χ^2 minimization algorithm, we estimate the mass of the cluster, the SMBH mass, and the NSC distance. We discuss our results and summarize our conclusions in Section 2.5. The Appendix contains some details on our use of the Qian et al. (1995) algorithm to calculate the two-integral distribution function for the fitted density model.

2.2 Dataset

We first give a brief description of the data set used for our dynamical analysis. These data are taken from Fritz et al. (2014) and are thoroughly examined in that paper, which should be consulted for more details. The coordinate system used is a shifted Galactic coordinate system (l^*, b^*) where Sgr A* is at the center and (l^*, b^*) are parallel to Galactic coordinates (l, b) . In the following we always refer to the shifted coordinates but will omit the asterisks for simplicity. The

dataset consists of stellar number densities, proper motions and line-of-sight velocities. We use the stellar number density map rather than the surface brightness map because it is less sensitive to individual bright stars and non-uniform extinction.

The stellar number density distribution is constructed from NACO high-resolution images for $R_{\text{box}} < 20''$, in a similar way as in Schödel et al. (2010), from HST WFC3/IR data for $20'' < R_{\text{box}} < 66''$, and from VISTA-VVV data for $66'' < R_{\text{box}} < 1000''$.

The kinematic data include proper motions for $\sim 10^4$ stars obtained from AO assisted images. The proper motion stars are binned into 58 cells (Figure 2.1; Fritz et al., 2014) according to distance from Sgr A* and the Galactic plane. This binning assumes that the NSC is symmetric with respect to the Galactic plane and with respect to the b -axis on the sky, consistent with axisymmetric dynamical modeling. The sizes of the bins are chosen such that all bins contain comparable numbers of stars, and the velocity dispersion gradients are resolved, i.e., vary by less than the error bars between adjacent bins.

Relative to the large velocity dispersions at the Galactic center (100 km/s), measurement errors for individual stars are typically $\sim 10\%$, much smaller than in typical globular cluster proper motion data where they can be $\sim 50\%$ (e.g., in Omega Cen; van de Ven et al. (2006)). Therefore corrections for these measurement errors are very small.

We also use $\sim 2^5$ radial velocities obtained from SINFONI integral field spectroscopy. The binning of the radial velocities is shown in Fig. 2.2. There are 46 rectangular outer bins as shown in Fig. 2.2 plus 6 small rectangular rings around the center (not shown; see App. E of Fritz et al., 2014). Again the outer bins are chosen such that they contain similar numbers of stars and the velocity dispersion gradients are resolved. The distribution of radial velocity stars on the sky is different from the distribution of proper motion stars, and it is not symmetric with respect to $l = 0$. Because of this and the observed rotation, the binning is different, and extends to both positive and negative longitudes. Both the proper motion and radial velocity binning are also used in Fritz et al. (2014) and some tests are described in that paper.

Finally, we compare our models with (but do not fit to) the kinematics derived from about 200 maser velocities at $r > 100''$ (from Lindquist et al., 1992; Deguchi et al., 2004). As for the proper motion and radial velocity bins, we use the mean velocities and velocity dispersions as derived in Fritz et al. (2014).

The assumption that the NSC is symmetric with respect to the Galactic plane and the $b = 0$ axis is supported by the recent Spitzer/IRAC photometry (Schödel et al., 2014) and by the distribution of proper motions (Fritz et al., 2014). The radial velocity data at intermediate radii instead show an apparent misalignment with respect to the Galactic plane, by $\sim 10^\circ$; see Feldmeier et al. (2014) and Fritz et al. (2014). We show in Section 2.4.2 that, even if confirmed, such a misaligned structure would have minimal impact on the results obtained here with the symmetrised analysis.

2.3 Spherical models of the NSC

In this section we study the NSC using the preliminary assumption that the NSC can be described by an isotropic distribution function (DF) depending only on energy. We use the DF to predict the kinematical data of the cluster. Later we add rotation self-consistently to the model. The advantages of using a distribution function instead of common Jeans modeling are that (i) we can always check if a DF is positive and therefore if the model is physical, and (ii) the DF provides

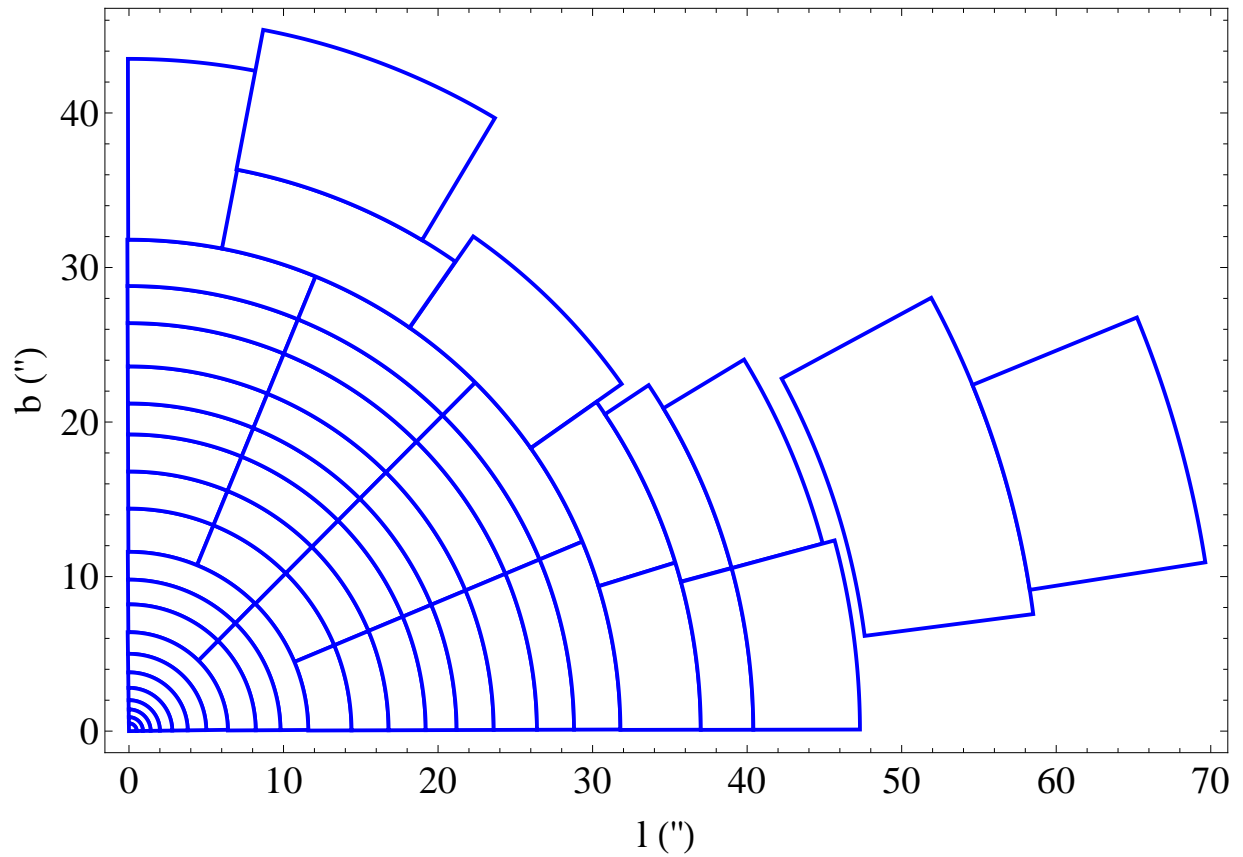


Figure 2.1: Binning of the proper motion velocities. The stars are binned into cells according to their distance from Sgr A* and their smallest angle to the Galactic plane (Fritz et al., 2014).

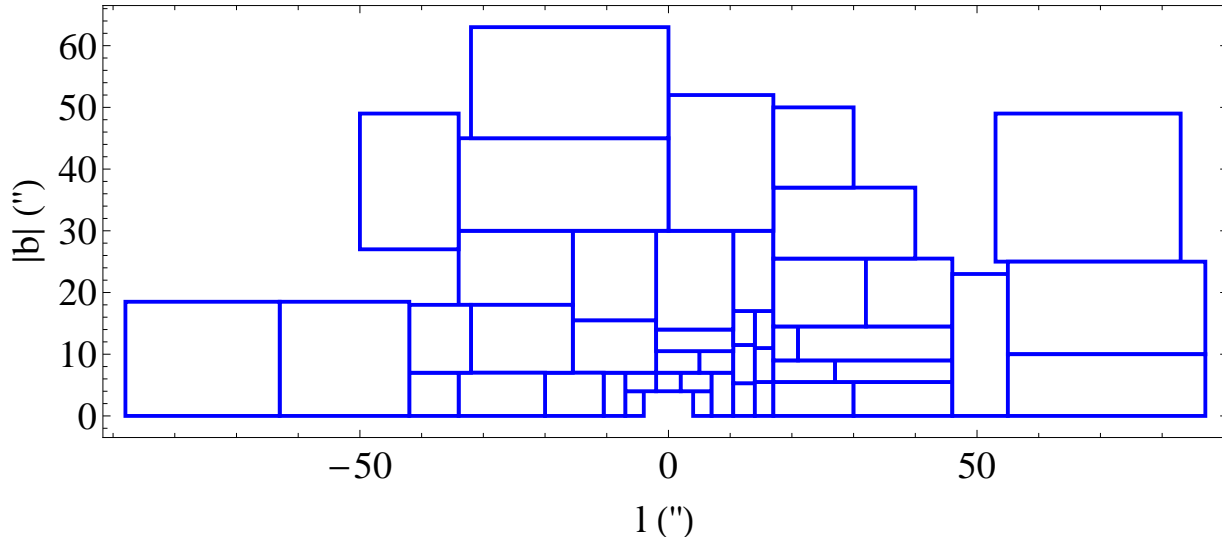


Figure 2.2: Binning of the line-of-sight velocities. The stars are binned into 46 rectangular outer cells plus 6 rectangular rings at the center. The latter are located within the white area around $l = b = 0$ and are not shown in the plot; see App. E of Fritz et al. (2014).

us with all the moments of the system. For the rest of the paper we use (r, θ, φ) for spherical and (R, φ, z) for cylindrical coordinates, with $\theta = 0$ corresponding to the z-axis normal to the equatorial plane of the NSC.

2.3.1 Mass model for the NSC

The first step is to model the surface density. We use the well-known one-parameter family of spherical γ -models (Dehnen, 1993):

$$\rho_\gamma(r) = \frac{3 - \gamma}{4\pi} \frac{M a}{r^\gamma (r + a)^{4-\gamma}}, \quad 0 \leq \gamma < 3 \quad (2.1)$$

where a is the scaling radius and M the total mass. The model behaves as $\rho \sim r^{-\gamma}$ for $r \rightarrow 0$ and $\rho \sim r^{-4}$ for $r \rightarrow \infty$. Dehnen γ models are equivalent to the η -models of Tremaine et al. (1994) under the transformation $\gamma = 3 - \eta$. Special cases are the Jaffe (1983) and Hernquist (1990) models for $\gamma = 2$ and $\gamma = 1$ respectively. For $\gamma = 3/2$ the model approximates de Vaucouleurs $R^{1/4}$ law. In order to improve the fitting of the surface density we use a combination of two γ -models, i.e.

$$\rho(r) = \sum_{i=1}^2 \frac{3 - \gamma_i}{4\pi} \frac{M_i a_i}{r^{\gamma_i} (r + a_i)^{4-\gamma_i}}. \quad (2.2)$$

The use of a two-component model will prove convenient later when we move to the axisymmetric case. The projected density is

$$\Sigma(R_s) = 2 \int_{R_s}^{\infty} \rho(r) r / (r^2 - R_s^2)^{1/2} dr \quad (2.3)$$

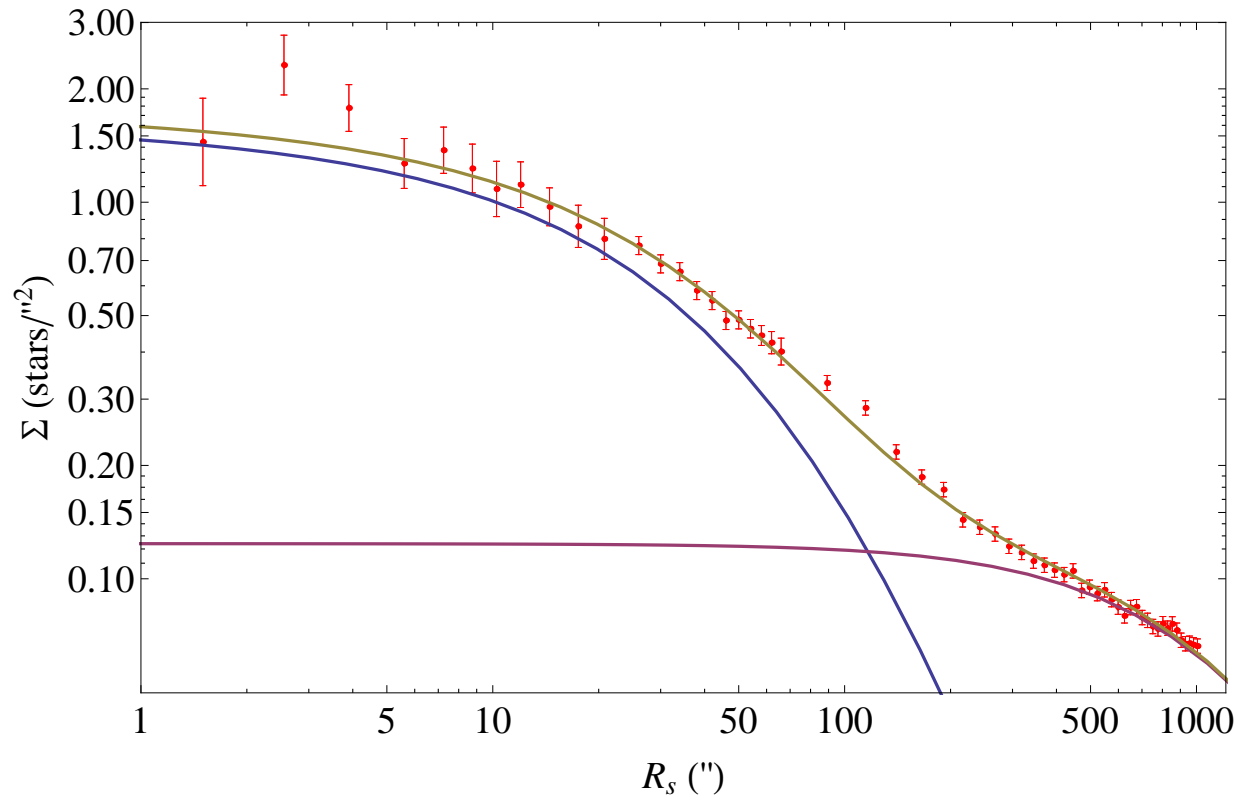


Figure 2.3: A combination of two γ -models gives an accurate approximation to the spherically averaged number density of late-type stars versus radius on the sky (points with error bars). Blue line: inner component, purple line: outer component, brown line: both components.

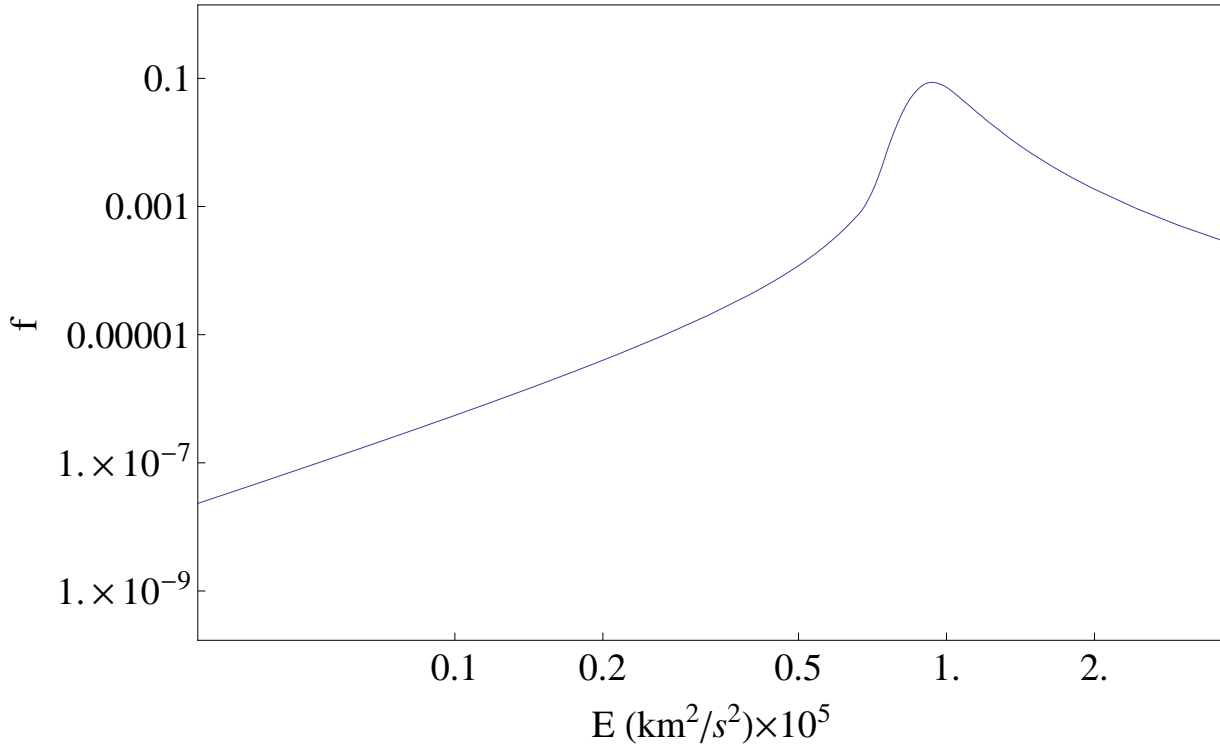


Figure 2.4: Isotropic DF for the two-component spherical model of the NSC in the joint gravitational potential including also a central black hole. Parameters for the NSC are as given in (2.4), and $M_{\bullet}/(M_1 + M_2) = 1.4 \times 10^{-3}$.

and can be expressed in terms of elementary functions for integer γ , or in terms of elliptic integrals for half-integer γ . For arbitrary γ_1 and γ_2 the surface density can only be calculated numerically using equation (2.3). The surface density diverges for $\gamma > 1$ but is finite for $\gamma < 1$.

The projected number density profile of the NSC obtained from the data of Fritz et al. (2014) (see Section 2.2) is shown in Figure 2.3. The inflection point at $R_s \sim 100''$ indicates that the NSC is embedded in a more extended, lower-density component. The surface density distribution can be approximated by a two-component model of the form of equation (2.2), where the six parameters $(\gamma_1, M_1, a_1, \gamma_2, M_2, a_2)$ are fitted to the data subject to the following constraints: The slope of the inner component should be $\gamma_1 > 0.5$ because isotropic models with a black hole and $\gamma_1 < 0.5$ are unphysical (Tremaine et al., 1994), but it should be close to the limiting value of 0.5 to better approximate the observed core near the center (Buchholz et al., 2009). For the outer component $\gamma_2 \ll 0.5$ so that it is negligible in the inner part of the density profile. In addition $M_1 < M_2$ and $a_1 < a_2$. With these constraints we start with some initial values for the parameters and then iteratively minimize χ^2 . The reduced χ^2 resulting from this procedure is

$\chi^2/\nu = 0.93$ for $\nu = 55$ d.o.f. and the corresponding best-fit parameter values are:

$$\begin{aligned} \gamma_1 &= 0.51 & a_1 &= 99'' & \frac{M_2}{M_1} &= 105.45. \\ \gamma_2 &= 0.07 & a_2 &= 2376'' & & \end{aligned} \quad (2.4)$$

Here we provide only the ratio of masses instead of absolute values in model units since the shape of the model depends only on the ratio. The surface density of the final model is overplotted on the data in Figure 2.3.

2.3.2 Spherical model

With the assumption of constant mass-to-light ratio and the addition of the black hole the potential ($\Phi = -\Psi$) will be (Dehnen, 1993)

$$\Psi(r) = \sum_{i=1}^2 \frac{GM_i}{a_i} \frac{1}{(2-\gamma_i)} \left(1 - \left(\frac{r}{r+a} \right)^{2-\gamma_i} \right) + \frac{GM_\bullet}{r} \quad (2.5)$$

where M_\bullet is the mass of the black hole. Since we now know the potential and the density we can calculate the distribution function (DF) numerically using Eddington's formula, as a function of positive energy $E = \Psi - \frac{1}{2}v^2$,

$$f(E) = \frac{1}{\sqrt{8\pi^2}} \left[\int_0^E \frac{d\Psi}{\sqrt{E-\Psi}} \frac{d^2\rho}{d\Psi^2} + \frac{1}{\sqrt{E}} \left(\frac{d\rho}{d\Psi} \right)_{\Psi=0} \right]. \quad (2.6)$$

The 2nd term of the equation vanishes for reasonable behavior of the potential and the double derivative inside the integral can be calculated easily by using the transformation

$$\frac{d^2\rho}{d\Psi^2} = \left[- \left(\frac{d\Psi}{dr} \right)^{-3} \frac{d^2\Psi}{dr^2} \right] \frac{d\rho}{dr} + \left(\frac{d\Psi}{dr} \right)^{-2} \frac{d^2\rho}{dr^2}. \quad (2.7)$$

Figure 2.4 shows the DF of the two components in their joint potential plus that of a black hole with mass ratio $M_\bullet/(M_1 + M_2) = 1.4 \times 10^{-3}$. The DF is positive for all energies. We can test the accuracy of the DF by retrieving the density using

$$\rho(r) = 4\pi \int_0^\Psi dE f(E) \sqrt{\Psi - E} \quad (2.8)$$

and comparing it with equation (2.2). Both agree to within 0.1%. The DF has the typical shape of models with a shallow cusp of $\gamma < \frac{3}{2}$. It decreases as a function of energy both in the neighborhood of the black hole and also for large energies. It has a maximum near the binding energy of the stellar potential well (Baes et al., 2005).

For a spherical isotropic model the velocity ellipsoid (Binney & Tremaine, 2008) is a sphere of radius σ . The intrinsic dispersion σ can be calculated directly using

$$\sigma^2(r) = \frac{4\pi}{3\rho(r)} \int_0^\infty dv v^4 f\left(\frac{1}{2}v^2 - \Psi\right). \quad (2.9)$$

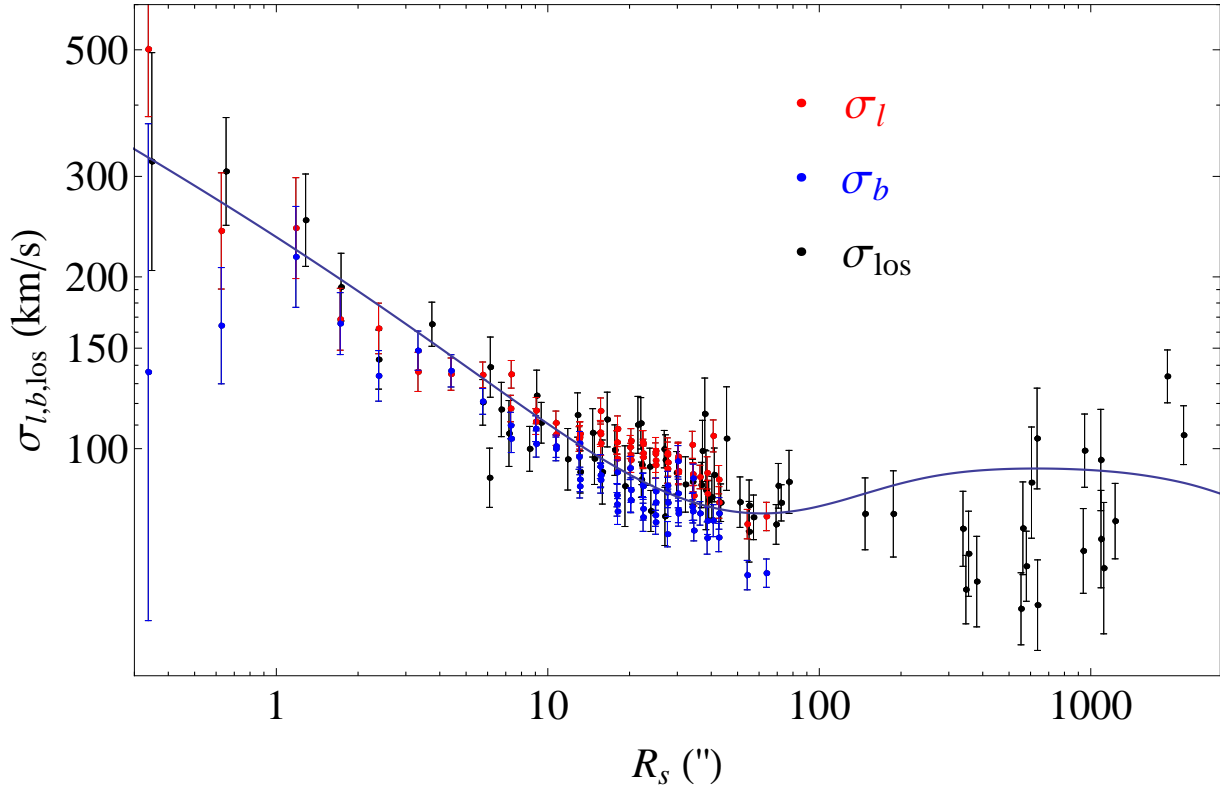


Figure 2.5: Line-of-sight velocity dispersion σ_{los} of the two-component spherical model with black hole, compared to the observed line-of-sight dispersions (black) and the proper motion dispersions in l (red) and b (blue). The line-of-sight data includes the outer maser data, and for the proper motions a canonical distance of $R_0 = 8$ kpc is assumed.

The projected dispersion is then given by:

$$\Sigma(R_s)\sigma_P^2(R_s) = 2 \int_{R_s}^{\infty} \sigma^2(r) \frac{\rho(r)r}{\sqrt{r^2 - R_s^2}} dr. \quad (2.10)$$

In Figure 2.5 we see how our two-component model compares with the kinematical data using the values $R_0 = 8$ kpc for the distance to the Galactic centre, $M_{\bullet} = 4 \times 10^6 M_{\odot}$ for the black hole mass, and $M_*(r < 100'') = 5 \times 10^6 M_{\odot}$ for the cluster mass inside $100''$. The good match of the data up to $80''$ suggests that the assumption of constant mass-to-light ratio for the cluster is reasonable. Later-on we will see that a flattened model gives a much better match also for the maser data.

2.3.3 Adding self-consistent rotation to the spherical model

We describe here the effects of adding self-consistent rotation to the spherical model, but much of this also applies to the axisymmetric case which will be discussed in Section 2.4. We assume that the rotation axis of the NSC is aligned with the rotation axis of the Milky Way disk. We also use a cartesian coordinate system (x, y, z) where z is parallel to the axis of rotation as before, y is along the line of sight, and x is along the direction of negative longitude, with the center of the NSC located at the origin. The proper motion data are given in Galactic longitude l and Galactic latitude b angles, but because of the large distance to the center, we can assume that $x \parallel l$ and $z \parallel b$.

Whether a spherical system can rotate has been answered in Lynden Bell (1960). Here we give a brief review. Rotation in a spherical or axisymmetric system can be added self-consistently by reversing the sense of rotation of some of its stars. Doing so, the system will remain in equilibrium. This is equivalent with adding to the DF a part that is odd with respect to L_z . The addition of an odd part does not affect the density (or the mass) because the integral of the odd part over velocity space is zero. The most effective way to add rotation to a spherical system is by reversing the sense of rotation of all of its counterrotating stars. This corresponds to adding $f_-(E, L^2, L_z) = \text{sign}(L_z)f(E, L^2)$ (Maxwell's daemon, Lynden Bell, 1960) to the initially non-rotating DF, and generates a system with the maximum allowable rotation. The general case of adding rotation to a spherical system can be written $f'(E, L^2, L_z) = (1 + g(L_z))f(E, L^2)$ where $g(L_z)$ is an odd function with $\max|g(L_z)| < 1$ to ensure positivity of the DF. We notice that the new distribution function is a three-integral DF. In this case the density of the system is still rotationally invariant but f_- is not.

In Figure 2.5 we notice that the projected velocity dispersion in the l direction is larger than the dispersion in the b direction which was first found by Trippe et al. (2008). This is particularly apparent for distances larger than $10''$. A heuristic attempt to explain this difference was made in Trippe et al. (2008) where they imposed a rotation of the form $v_\varphi(r, \theta)$ along with their Jeans modeling, as a proxy for axisymmetric modeling. Here we show that for a self-consistent system the difference in the projected l and b dispersions cannot be explained by just adding rotation to the cluster.

Specifically, we show that adding an odd part to the distribution function does not change the proper motion dispersion σ_x . The dispersion along the x axis is $\sigma_x^2 = \overline{v_x^2} - \bar{v}_x^2$. Writing v_x in spherical velocity components (see the beginning of this section for the notation),

$$v_x = v_R \frac{x}{R} - v_\varphi \frac{y}{R} = v_r \sin \theta \frac{x}{R} + v_\theta \cos \theta \frac{x}{R} - v_\varphi \frac{y}{R} \quad (2.11)$$

we see that

$$\begin{aligned} \overline{v_x^2} &= \int dv_r \int dv_\theta \int dv_\varphi v_x^2 (1 + g(L_z)) f_+ = \\ &= \int dv_r \int dv_\theta \int dv_\varphi v_x^2 f_+ + 0. \end{aligned} \quad (2.12)$$

The second term vanishes because $f_+(E, L^2)g(L_z)$ is even in v_r , v_θ and odd in v_φ , so that the integrand for all terms of $f_+g v_x^2$ is odd in at least one velocity variable. We also have

$$\begin{aligned} \bar{v}_x &= \int dv_r \int dv_\theta \int dv_\varphi v_x (1 + g(L_z)) f_+ = \\ &= 0 - \int dv_r \int dv_\theta \int dv_\varphi v_\varphi \frac{y}{R} f_+ g. \end{aligned} \quad (2.13)$$

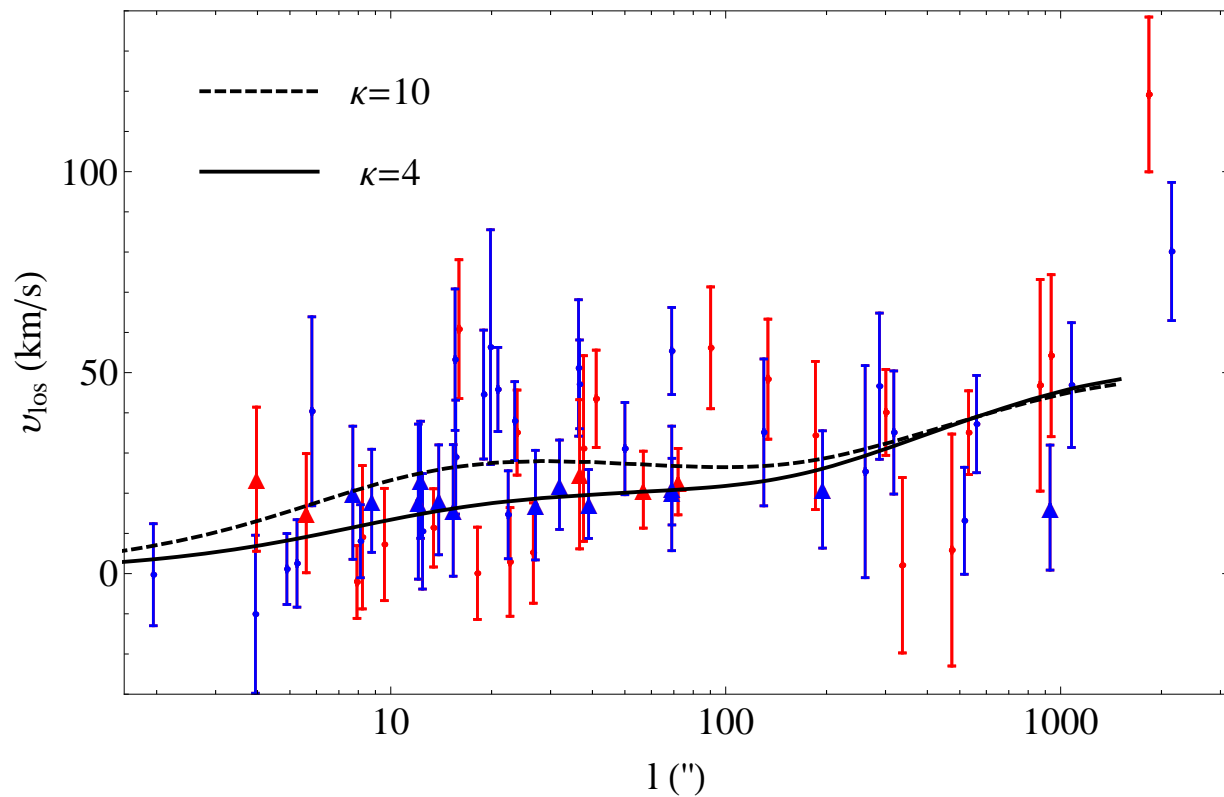


Figure 2.6: Mean line-of-sight velocity data compared to the prediction of the two-component spherical model with added rotation for $F = -0.90$ and two κ values for illustration. Each data point corresponds to a cell from Figure 2.2. Velocities at negative l have been folded over with their signs reversed and are shown in red. The plot also includes the maser data at $R_s > 100''$. The model prediction is computed for $b = 20''$. For comparison, cells with centers between $b = 15''$ and $b = 25''$ are highlighted with filled triangles.

The first part is zero because $v_x f_+$ is odd. The second part is different from zero; however when projecting \bar{v}_φ along the line-of-sight this term also vanishes because $f_+ g$ is an even function of y when the integration is in a direction perpendicular to the L_z angular momentum direction. Hence the projected mean velocity \bar{v}_x is zero, and the velocity dispersion $\sigma_x^2 = \bar{v}_x^2$ is unchanged.

An alternative way to see this is by making a particle realization of the initial DF (e.g. Aarseth et al., 1974). Then we can add rotation by reversing the sign of L_z of a percentage of particles using some probability function which is equivalent to changing the signs of v_x and v_y of those particles. \bar{v}_x^2 will not be affected by the sign change and the \bar{v}_x^2 averaged over the line-of-sight will be zero because for each particle at the front of the system rotating in a specific direction there will be another particle at the rear of the system rotating in the opposite direction. In this work we do not use particle models to avoid fluctuations due to the limited number of particles near the center.

For the odd part of the DF we choose the two-parameter function from Qian et al. (1995). This is a modified version of Dejonghe (1986) which was based on maximum entropy arguments:

$$g(L_z) = G(\eta) = F \frac{\tanh(\kappa\eta/2)}{\tanh(\kappa/2)} \quad (2.14)$$

where $\eta = L_z/L_m(E)$, $L_m(E)$ is the maximum allowable value of L_z at a given energy, and $-1 < F < 1$ and $\kappa > 0$ are free parameters. The parameter F works as a global adjustment of rotation while the parameter κ determines the contributions of stars with different L_z ratios. Specifically for small κ only stars with high L_z will contribute while large κ implies that all stars irrespective of their L_z contribute to rotation. For $F=1$ and $\kappa \gg 0$, $g(L_z) = \text{sign}(L_z)$ which corresponds to maximum rotation.

From the resulting distribution function $f(E, L_z)$ we can calculate $\bar{v}_\varphi(R, z)$ in cylindrical coordinates using the equation

$$\bar{v}_\varphi(R, z) = \frac{4\pi}{\rho R^2} \int_0^\Psi dE \int_0^{R\sqrt{2(\Psi-E)}} f_-(E, L_z) L_z dL_z. \quad (2.15)$$

To find the mean line-of-sight velocity versus Galactic longitude l we have to project equation (2.15) to the sky plane

$$v_{\text{los}}(x, z) = \frac{2}{\Sigma} \int_x^\infty \bar{v}_\varphi(R, z) \frac{x \rho(R, z) R dR}{R \sqrt{R^2 - x^2}}. \quad (2.16)$$

Figure 2.6 shows the mean line-of-sight velocity data vs Galactic longitude l for $F = -0.9$ and two κ values for the parameters in equation (2.14). Later in the axisymmetric section we constrain these parameters by fitting. Each data point corresponds to a cell from Figure 2.2. The maser data ($r > 100''$) are also included. The signs of velocities for negative l are reversed because of the assumed symmetry. The line shows the prediction of the model with parameters determined with equation (2.16). Figure 2.2 shows that the line-of-sight velocity cells extend from $b=0$ to up to $b = 50''$, but most of them lie between 0 and $b = 20''$. For this reason we compute the model prediction at an average value of $b = 20''$.

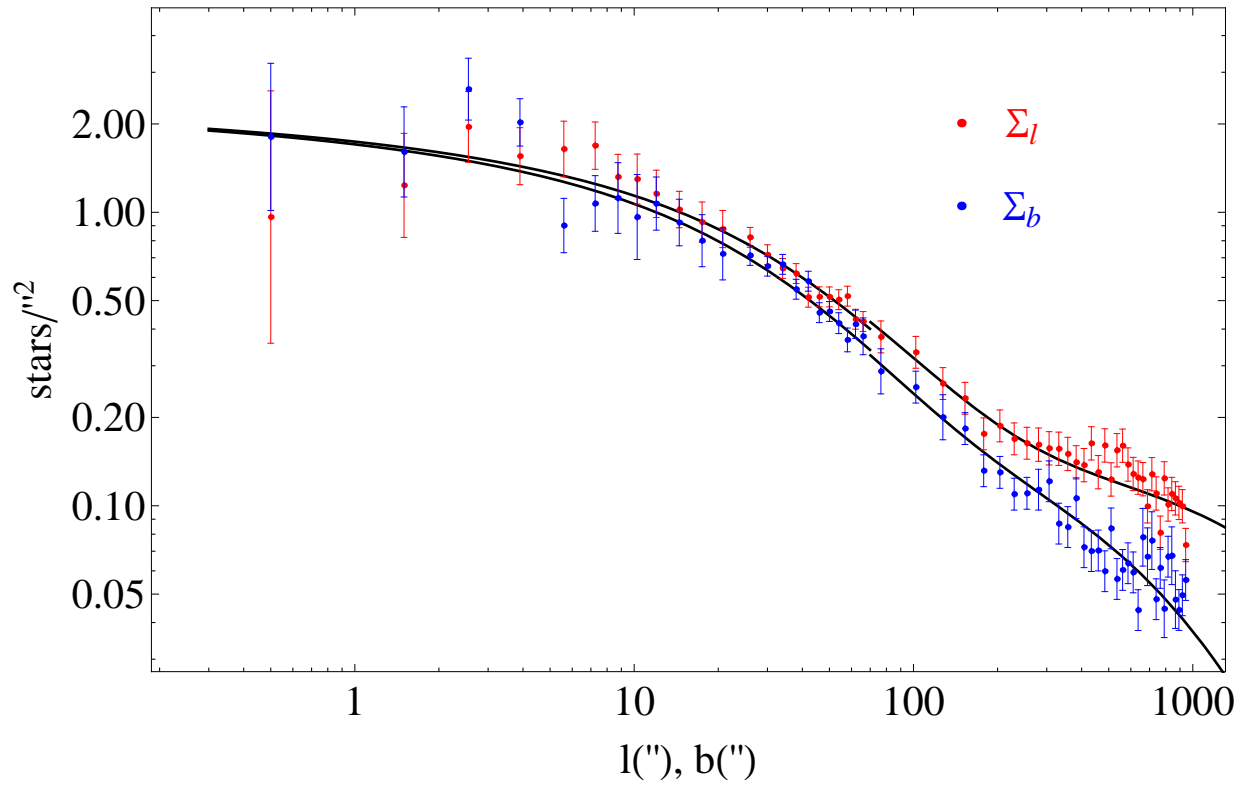


Figure 2.7: Axisymmetric two-component model for the surface density of the nuclear cluster. The points with error bars show the number density of late-type stars along the l and b directions (Fritz et al., 2014) in red and blue respectively. The blue lines show the model that gives the best fit to the surface density data with parameters as in 2.19.

2.4 Axisymmetric modeling of the NSC

We have seen that spherical models cannot explain the difference between the velocity dispersions along the l and b directions. The number counts also show that the cluster is flattened; see Figure 2.7 and Fritz et al. (2014). Therefore we now continue with axisymmetric modeling of the nuclear cluster. The first step is to fit the surface density counts with an axisymmetric density model. The available surface density data extend up to $1000''$ in the l and b directions. For comparison, the proper motion data extend to $\sim 70''$ from the centre (Figure 2.1). We generalize our spherical two-component γ -model from equation (2.2) to a spheroidal model given by

$$\rho(R, z) = \sum_{i=1}^2 \frac{3 - \gamma_i}{4\pi q_i} \frac{M_i a_i}{m_i^{\gamma_i} (m_i + a_i)^{4 - \gamma_i}} \quad (2.17)$$

where $m_i^2 = R^2 + z^2/q_i^2$ is the spheroidal radius and the two new parameters $q_{1,2}$ are the axial ratios (prolate > 1 , oblate < 1) of the inner and outer component, respectively. Note that the method can be generalized to N components. The mass of a single component is given by $4\pi q_i \int_0^\infty m_i^2 \rho(m_i) dm_i$. From Figure 2.7 we expect that the inner component will be more spherical than the outer component, although when the density profile gets flatter near the center it becomes more difficult to determine the axial ratio. In Figure 2.7 one also sees that the stellar surface density along the l direction is larger than along the b direction. Thus we assume that the NSC is an oblate system. To fit the model we first need to project the density and express it as a function of l and b . The projected surface density as seen edge on is

$$\Sigma(x, z) = 2 \int_x^\infty \frac{\rho(R, z) R}{\sqrt{R^2 - x^2}} dR. \quad (2.18)$$

In general, to fit equation (2.18) to the data we would need to determine the eight parameters $\gamma_{1,2}$, $M_{1,2}$, $a_{1,2}$, $q_{1,2}$. However, we decided to fix a value for q_2 because the second component is not very well confined in the 8-dimensional parameter space (i.e. there are several models each with different q_2 and similar χ^2). We choose $q_2 = 0.28$, close to the value found in Fritz et al. (2014). For similar reasons, we also fix the value of γ_2 to that used in the spherical case. The minimum value of γ_1 for a semi-isotropic axisymmetric model with a black hole cannot be smaller than 0.5 (Qian et al., 1995), as in the spherical case. For our current modeling we treat γ_1 as a free parameter. Thus six free parameters remain. To fit these parameters to the data in Fig. 2.7 we apply a Markov chain Monte Carlo algorithm. For comparing the model surface density (2.18) to the star counts we found it important to average over angle in the inner conical cells to prevent an underestimation of the q_1 parameter. The values obtained with the MCMC algorithm for the NSC parameters and their errors are:

$$\begin{aligned} \gamma_1 &= 0.71 \pm 0.12 & a_1 &= 147.6'' \pm 27'' & q_1 &= 0.73 \pm 0.04 \\ \gamma_2 &= 0.07 & a_2 &= 4572'' \pm 360'' & q_2 &= 0.28 \\ M_2/M_1 &= 101.6 \pm 18 \end{aligned} \quad (2.19)$$

The reduced χ^2 that corresponds to these parameter values is $\chi^2/\nu_{SD} = 0.99$ for $\nu_{SD} = 110$ d.o.f. Here we note that there is a strong correlation between the parameters a_2 and M_2 . The

flattening of the inner component is very similar to the recent determination from Spitzer/IRAC photometry (0.71 ± 0.02 , Schödel et al., 2014) but slightly more flattened than the best value given by Fritz et al. (2014), 0.80 ± 0.04 . The second component is about 100 times more massive than the first, but also extends more than one order of magnitude further.

Assuming constant mass-to-light ratio for the star cluster, we determine its potential using the relation from Qian et al. (1995), which is compatible with their contour integral method (i.e. it can be used for complex R^2 and z^2). The potential for a single component i is given by:

$$\begin{aligned} \Psi_i(R, z) = & \Psi_{0i} - \frac{2\pi G q_i}{e_i} \int_0^\infty \rho_i(U) \left[\frac{R^2}{(1+u)^2} + \frac{z^2}{(q_i^2+u)^2} \right] \\ & \times (\arcsin e_i - \arcsin \frac{e_1}{\sqrt{1+u}}) du \end{aligned} \quad (2.20)$$

with $e_i = \sqrt{1 - q_i^2}$, $U = \frac{R^2}{1+u} + \frac{z^2}{q_i^2+u}$, and where Ψ_{0i} is the central potential (for a review of the potential theory of ellipsoidal bodies consider Chandrasekhar (1969)). The total potential of the two-component model is

$$\Psi(R, z) = \sum_{i=1}^2 \Psi_i(R, z) + \frac{GM_\bullet}{\sqrt{R^2 + z^2}}. \quad (2.21)$$

2.4.1 Axisymmetric Jeans modeling

Here we first continue with axisymmetric Jeans modeling. We will need a large number of models to determine the best values for the mass and distance of the NSC, and for the mass of the embedded black hole. We will use DFs for the detailed modeling in Section 4.3, but this is computationally expensive, and so a large parameter study with the DF approach is not currently feasible. In Section 4.3 we will show that a two-integral (2I) distribution function of the form $f(E, L_z^2)$ gives a very good representation to the histograms of proper motions and line-of-sight velocities for the nuclear star cluster in all bins. Therefore we can assume for our Jeans models that the system is semi-isotropic, i.e., isotropic in the meridional plane, $\overline{v_z^2} = \overline{v_R^2}$. From the tensor virial theorem (Binney & Tremaine, 2008) we know that for 2I-models $\overline{v_\Phi^2} > \overline{v_R^2}$ in order to produce the flattening. In principle, for systems of the form $f(E, L_z)$ it is possible to find recursive expressions for any moment of the distribution function (Magorrian & Binney, 1994) if we know the potential and the density of the system. However, here we will confine ourselves to the second moments, since later we will recover the distribution function. By integrating the Jeans equations we get relations for the independent dispersions (Nagai & Miyamoto, 1976):

$$\begin{aligned} \overline{v_z^2}(R, z) = \overline{v_R^2}(R, z) &= -\frac{1}{\rho(R, z)} \int_z^\infty dz' \rho(R, z') \frac{\partial \Psi}{\partial z'} \\ \overline{v_\varphi^2}(R, z) = \overline{v_R^2}(R, z) &+ \frac{R}{\rho(R, z)} \frac{\partial(\rho v_R^2)}{\partial R} - R \frac{\partial \Psi}{\partial R} \end{aligned} \quad (2.22)$$

The potential and density are already known from the previous section. Once $\overline{v_z^2}$ is found it can be used to calculate $\overline{v_\varphi^2}$. The intrinsic dispersions in l and b direction are given by the equations:

$$\begin{aligned} \sigma_b^2 &= \overline{v_z^2} \\ \sigma_l^2 = \overline{v_x^2} &= \overline{v_R^2} \sin^2 \theta + \overline{v_\varphi^2} \cos^2 \theta \\ \overline{v_{\text{los}}^2} = \overline{v_y^2} &= \overline{v_R^2} \cos^2 \theta + \overline{v_\varphi^2} \sin^2 \theta \end{aligned} \quad (2.23)$$

38 2. The old nuclear star cluster in the Milky Way: dynamics, M_0 , R_0 , M_{BH}

where $\sin^2\theta = x^2/R^2$ and $\cos^2\theta = 1 - x^2/R^2$. Projecting the previous equations along the line of sight we have:

$$\begin{aligned}
 \Sigma\sigma_l^2(x, z) &= \\
 2 \int_x^\infty \left[\overline{v_R^2} \frac{x^2}{R^2} + \overline{v_\varphi^2} \left(1 - \frac{x^2}{R^2} \right) \right] \frac{\rho(R, z)}{\sqrt{R^2 - x^2}} dR, \\
 \Sigma\sigma_b^2(x, z) &= \\
 2 \int_x^\infty \overline{v_z^2}(R, z) \frac{\rho(R, z)}{\sqrt{R^2 - x^2}} dR, \\
 \Sigma v_{\text{los}}^2(x, z) &= \\
 2 \int_x^\infty \left[\overline{v_R^2} \left(1 - \frac{x^2}{R^2} \right) + \overline{v_\varphi^2} \frac{x^2}{R^2} \right] \frac{\rho(R, z)}{\sqrt{R^2 - x^2}} dR,
 \end{aligned} \tag{2.24}$$

where we note that the last quantity in (2.23) and (2.24) is the 2^{nd} moment and not the line-of-sight velocity dispersion.

In order to define our model completely, we need to determine the distance R_0 and mass M_* of the cluster and the black hole mass M_\bullet . To do this we apply a χ^2 minimization technique matching all three velocity dispersions in both sets of cells, using the following procedure. First we note that the inclusion of self-consistent rotation to the model will not affect its mass. This means that for the fitting we can use $\overline{v_{\text{los}}^2}^{-1/2}$ for each cell of Figure 2.2. Similarly, since our model is axisymmetric we should match to the $\overline{v_{l,b}^2}^{-1/2}$ for each proper motion cell; the $\overline{v_{l,b}}$ terms should be and indeed are negligible. Another way to see this is that since the system is axially symmetric, the integration of $\overline{v_{l,b}}$ along the line-of-sight should be zero because the integration would cancel out for positive and negative y .

With this in mind we proceed as follows, using the cluster's density parameters¹ as given in (2.19). First we partition the 3d space (R_0 , M_* , M_\bullet) into a grid with resolution $20 \times 20 \times 20$. Then for each point of the grid we calculate the corresponding χ^2 using the velocity dispersions from all cells in Figs. 2.1 and 2.2, excluding the two cells at the largest radii (see Fig. 2.8). We compare the measured dispersions with the model values obtained from equations (2.24) for the centers of these cells. Then we interpolate between the χ^2 values on the grid and find the minimum of the interpolated function, i.e., the best values for (R_0 , M_* , M_\bullet). To determine statistical errors on these quantities, we first calculate the Hessian matrix from the curvature of χ^2 surface at the minimum, $\partial\chi^2/\partial p_i\partial p_j$. The statistical variances will be the diagonal elements of the inverted matrix.

With this procedure we obtain a minimum reduced $\chi^2/\nu_{\text{Jeans}} = 1.07$ with $\nu_{\text{Jeans}} = 161$ degrees of freedom, for the values

$$\begin{aligned}
 R_0 &= 8.27 \text{ kpc} \\
 M_*(m < 100'') &= 7.73 \times 10^6 M_\odot \\
 M_\bullet &= 3.86 \times 10^6 M_\odot,
 \end{aligned} \tag{2.25}$$

where

$$M_*(m) \equiv \int_0^m 4\pi m^2 [q_1\rho_1(m) + q_2\rho_2(m)] dm, \tag{2.26}$$

and the value given for M_* in (2.25) is not the total cluster mass but the stellar mass within elliptical radius $100''$. In Section 2.4.2 we will consider in more detail the determination of these

¹It is computationally too expensive to simultaneously also minimize χ^2 over the density parameters.

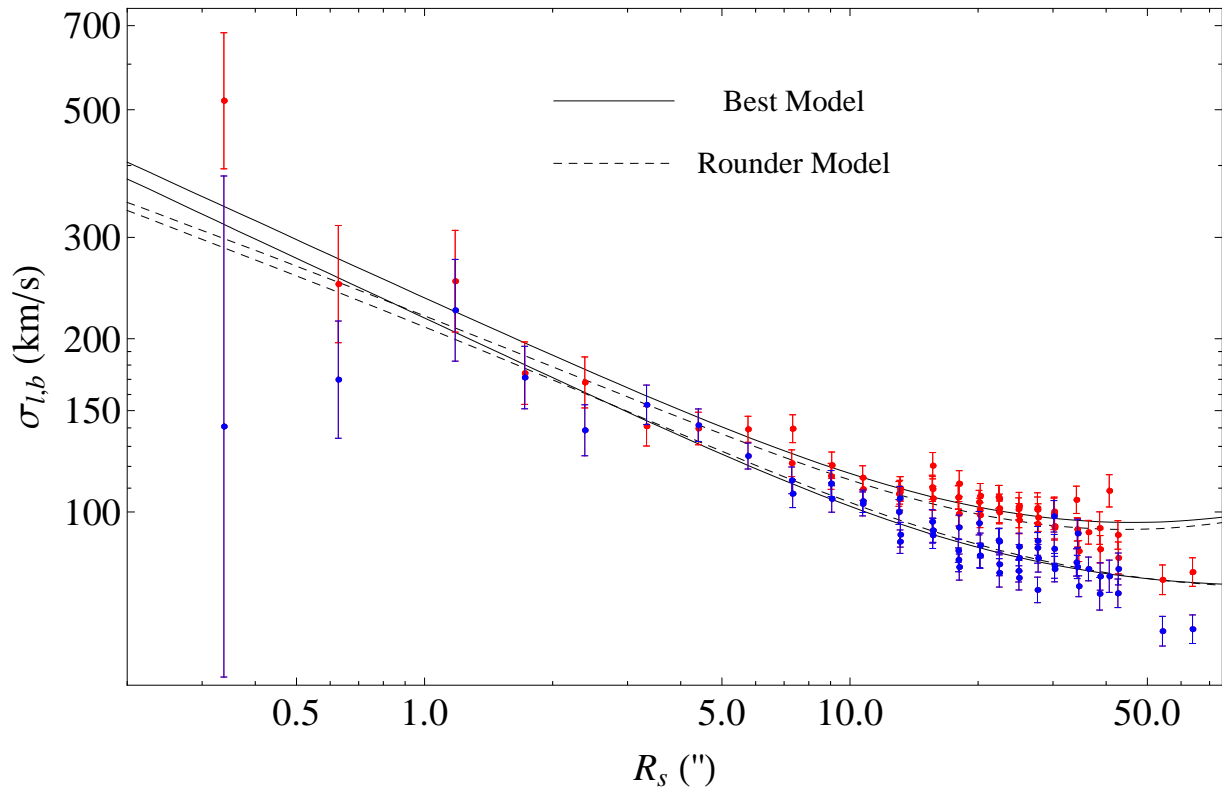


Figure 2.8: Velocity dispersions σ_l and σ_b compared to axisymmetric, semi-isotropic Jeans models. The measured dispersions σ_l (red points with error bars) and σ_b (blue points) for all cells are plotted as a function of their two-dimensional radius on the sky, with the Galactic centre at the origin. The black lines show the best model; the model velocity dispersions are averaged over azimuth on the sky. The dashed black lines show the same quantities for a model which has lower flattening ($q_1 = 0.85$ vs $q_1 = 0.73$) and a smaller central density slope (0.5 vs 0.7).

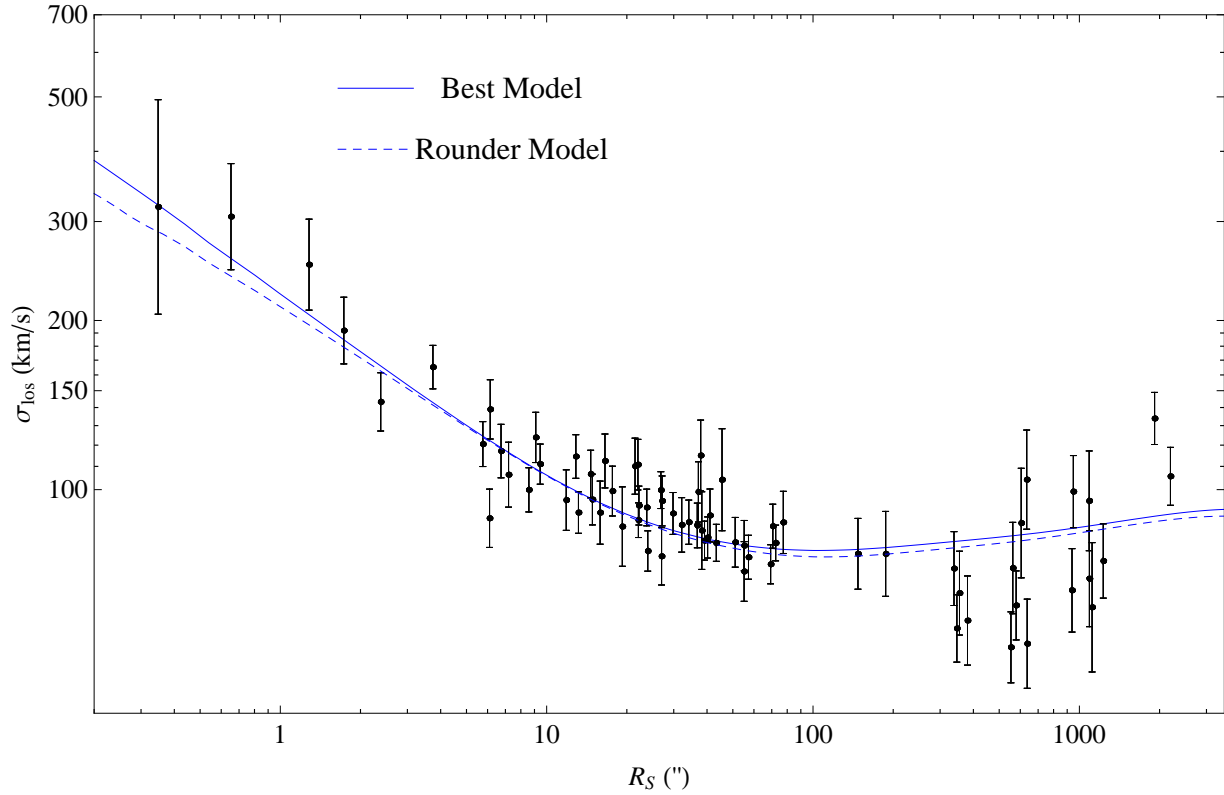


Figure 2.9: Root mean square line-of-sight velocities compared with the best model, as a function of two-dimensional radius on the sky as in Fig. 2.8. In both plots the stellar mass of the NSC is $7.73 \times 10^6 M_\odot$ within $m < 100''$, the black hole mass is $3.86 \times 10^6 M_\odot$, and the distance is 8.3 kpc (equation 2.25). All the maser data are included in the plot.

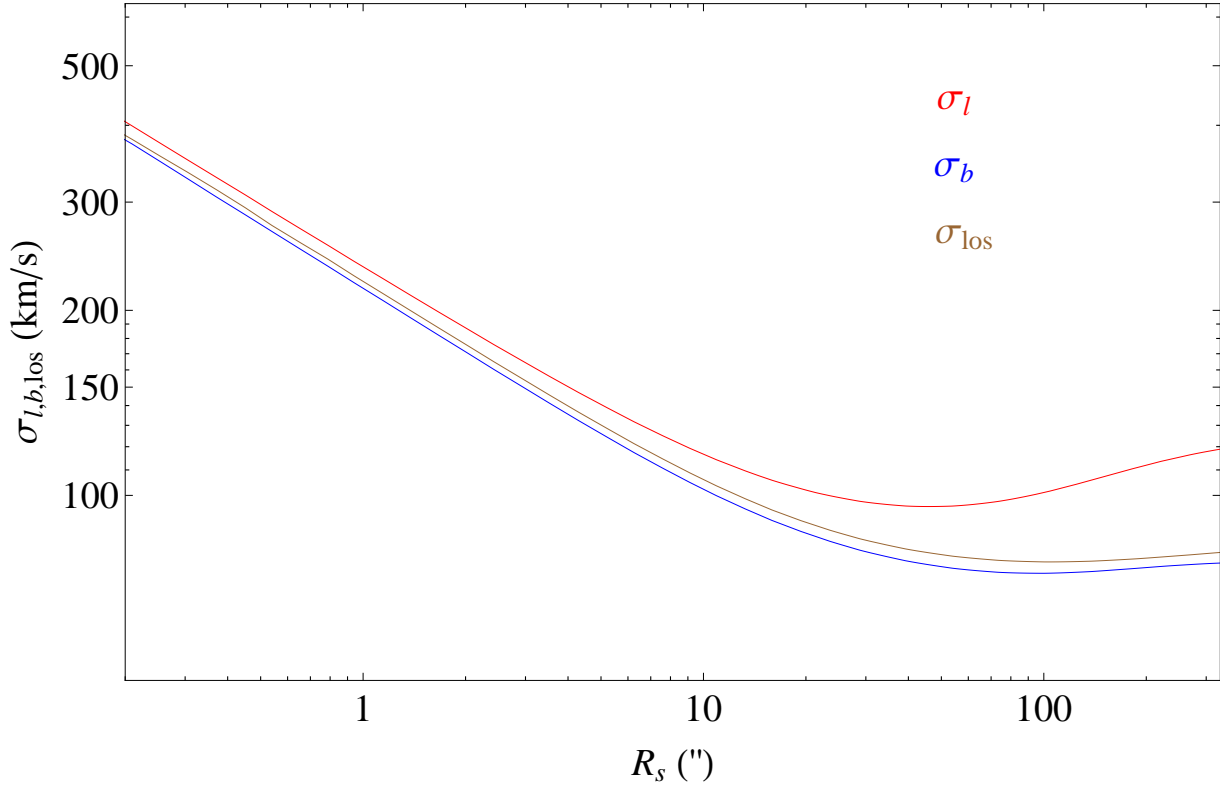


Figure 2.10: All three projected velocity dispersions compared. Red: σ_l , Blue: σ_b , Brown: $\sigma_{\text{los}} = v_{\text{los}}^2$. Note that σ_b is slightly lower than σ_{los} . The difference between σ_b and σ_l comes from the flattening of both the inner and outer components of the model.

parameters and their errors. The model with density parameters as in (2.19) and dynamical parameters as in (2.25) will be our best model. In Section 2.4.3 we will see that it also gives an excellent prediction to the velocity histograms.

First, we now look at the comparison of this model with the velocity data. Figure 2.8 shows how the azimuthally averaged dispersions σ_l and σ_b compare with the measured proper motion dispersions. Figure 2.9 shows how this best model, similarly averaged, compares with the line-of-sight mean square velocity data. The maser data are also included in the plot. It is seen that the model fits the data very well, in accordance with its $\chi^2/\nu_{\text{Jeans}} = 1.07$ per cell. Figure 2.10 shows how all three projected dispersions of the model compare. σ_b is slightly lower than σ_{los} due to projection effects. The fact that all three velocity dispersion profiles in Figs. 2.8, 2.9 are fitted well by the model suggests that the assumed semi-isotropic dynamical structure is a reasonable approximation.

The model prediction in Fig. 2.8 is similar to Figure 11 of Trippe et al. (2008) but the interpretation is different. As shown in the previous section, the difference in projected dispersions

cannot be explained by imposing rotation on the model. Here we demonstrated how the observational finding $\sigma_l > \sigma_b$ can be quantitatively reproduced by flattened axisymmetric models of the NSC and the surrounding nuclear disk.

Most of our velocity data are in the range $7''$ - $70''$, i.e., where the inner NSC component dominates the potential. In order to understand the dynamical implications of these data on the flattening of this component, we have also constructed several density models in which we fixed q_1 to values different from the $q_1 = 0.73$ obtained from star counts. In each case we repeated the fitting of the dynamical parameters as in (2.25). We found that models with q_1 in a range from ~ 0.69 to ~ 0.74 gave comparable fits (χ^2/ν) to the velocity dispersion data as our nominal best model but that a model with $q_1 = 0.77$ was noticeably worse. We present an illustrative model with flattening about half-way between the measured $q_1 = 0.73$ and the spherical case, for which we set $q_1 = 0.85$. This is also close to the value given by (Fritz et al., 2014), $q_1 = 0.80 \pm 0.04$. We simultaneously explore a slightly different inner slope, $\gamma_1 = 0.5$. We then repeat the fitting of the starcount density profile in Fig. 2.7 (model not shown), keeping also γ_2 and q_2 fixed to the previous values, and varying the remaining parameters. Our rounder comparison model then has the following density parameters:

$$\begin{aligned} \gamma_1 = 0.51 & \quad a_1 = 102.6'' & \quad q_1 = 0.85 & \quad \frac{M_2}{M_1} = 109.1 \\ \gamma_2 = 0.07 & \quad a_2 = 4086'' & \quad q_2 = 0.28 & \end{aligned} \quad (2.27)$$

The best reduced χ^2 that we obtain for the velocity dispersion profiles with these parameters is $\chi^2/\nu_{\text{Jeans}} = 1.16$ and corresponds to the values

$$\begin{aligned} R_0 &= 8.20 \text{ kpc} \\ M_*(m < 100'') &= 8.31 \times 10^6 M_\odot \\ M_\bullet &= 3.50 \times 10^6 M_\odot, \end{aligned} \quad (2.28)$$

Compared to the best and more flattened model, the cluster mass has increased and the black hole mass has decreased. The sum of both masses has changed only by 2% and the distance only by 1%. In Figures 2.8, 2.9 we see how the projected velocity dispersions of this model compare with our best model. The main difference seen in σ_l comes from the different flattening of the inner component, and the smaller slope of the dispersions near the center of the new model is because of its smaller central density slope.

2.4.2 Distance to the Galactic Center, mass of the star cluster, and mass of the black hole

We now consider the determination of these parameters from the NSC data in more detail. Fig 2.11 shows the marginalized χ^2 -plot for the NSC model as given in equation (2.19), for pairs of two parameters (R_0, M_\bullet) , (M_\bullet, M_*) , (R_0, M_*) , as obtained from fitting the Jeans dynamical model to the velocity dispersion profiles. The figure shows contour plots for constant $\chi^2/\nu_{\text{Jeans}}$ with 1σ , 2σ and 3σ in the three planes for the two-dimensional distribution of the respective parameters. We notice that the distance R_0 has the smallest relative error.

The best-fitting values for (R_0, M_*, M_\bullet) are given in equation (2.25); these values are our best estimates based on the NSC data alone. For the dynamical model with these parameters and the surface density parameters given in (2.19), the flattening of the inner component inferred from

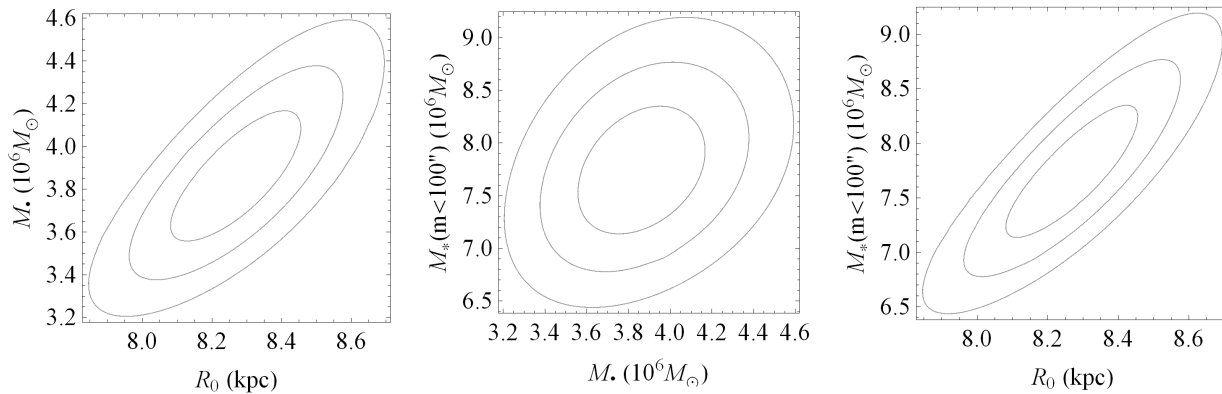


Figure 2.11: Contour plots for the marginalized χ^2 in the three parameter planes (R_0, M_\bullet) , (M_\bullet, M_*) , (R_0, M_*) . Contours are plotted at confidence levels corresponding to 1σ , 2σ and 3σ of the joint probability distribution. The minimum corresponds to the values $R_0 = 8.27\text{kpc}$, $M_*(m < 100'') = 7.73 \times 10^6 M_\odot$, $M_\bullet = 3.86 \times 10^6 M_\odot$, with errors discussed in Section 2.4.2.

the surface density data is consistent with the dynamical flattening, which is largely determined by the ratio of σ_l/σ_b and the tensor virial theorem.

Statistical errors are determined from the Hessian matrix for this model. Systematic errors can arise from uncertainties in the NSC density structure, from deviations from the assumed axisymmetric two-integral dynamical structure, from dust extinction within the cluster (see Section 2.5), and other sources. We have already illustrated the effect of varying the cluster flattening on (R_0, M_\bullet, M_*) with our second, rounder model. We have also tested how variations of the cluster density structure (a_2, q_2, M_2) beyond $500''$ impact the best-fit parameters, and found that these effects are smaller than those due to flattening variations.

We have additionally estimated the uncertainty introduced by the symmetrisation of the data if the misalignment found by Feldmeier et al. (2014); Fritz et al. (2014) were intrinsic to the cluster, as follows. We took all radial velocity stars and rotated each star by 10° clockwise on the sky. Then we resorted the stars into our radial velocity grid (Fig. 2.2). Using the new values v_{los}^2 obtained in the cells we fitted Jeans models as before. The values we found for R_0 , M_* , M_\bullet with these tilted data differed from those in equation (2.25) by $\Delta R_0 = -0.02$ kpc, $\Delta M_*(m < 100'') = -0.15 \times 10^6 M_\odot$, and $\Delta M_\bullet = +0.02 \times 10^6 M_\odot$, respectively, which are well within the statistical errors.

Propagating the errors of the surface density parameters from the MCMC fit and taking into account the correlation of the parameters, we estimate the systematic uncertainties from the NSC density structure to be ~ 0.1 kpc in R_0 , $\sim 6\%$ in M_\bullet , and $\sim 8\%$ $M_*(m < 100'')$. We will see in Section 2.4.3 below that the DF for our illustrative rounder NSC model gives a clearly inferior representation of the velocity histograms than our best kinematic model, and also that the systematic differences between both models appear comparable to the residual differences between our preferred model and the observed histograms. Therefore we take the differences between these models, $\sim 10\%$ in M_* , $\sim 10\%$ in M_\bullet , and $\sim 0.1\text{kpc}$ in R_0 , as a more conservative

estimate of the dynamical modeling uncertainties, so that finally

$$\begin{aligned} R_0 &= 8.27 \pm 0.09|_{\text{stat}} \pm 0.1|_{\text{syst}} \text{ kpc} \\ M_*(m < 100'') &= (7.73 \pm 0.31|_{\text{stat}} \pm 0.8|_{\text{syst}}) \times 10^6 M_\odot \\ M_\bullet &= (3.86 \pm 0.14|_{\text{stat}} \pm 0.4|_{\text{syst}}) \times 10^6 M_\odot. \end{aligned} \quad (2.29)$$

We note several other systematic errors which are not easily quantifiable and so are not included in these estimates, such as inhomogeneous sampling of proper motions or line-of-sight velocities, extinction within the NSC, and the presence of an additional component of dark stellar remnants.

Based on our best model, the mass of the star cluster within $100''$ converted into spherical coordinates is $M_*(r < 100'') = (8.94 \pm 0.32|_{\text{stat}} \pm 0.9|_{\text{syst}}) \times 10^6 M_\odot$. The model's mass within the innermost pc ($25''$) is $M_*(m < 1\text{pc}) = 0.729 \times 10^6 M_\odot$ in spheroidal radius, or $M_*(r < 1\text{pc}) = 0.89 \times 10^6 M_\odot$ in spherical radius. The total mass of the inner NSC component is $M_1 = 6.1 \times 10^7 M_\odot$. Because most of this mass is located beyond the radius where the inner component dominates the projected star counts, the precise division of the mass in the model between the NSC and the adjacent nuclear disk is dependent on the assumed slope of the outer density profile of NSC, and is therefore uncertain.

The distance and the black hole mass we found differ by 0.7% and 12%, respectively, from the values $R_0 = 8.33 \pm 0.17|_{\text{stat}} \pm 0.31|_{\text{syst}}$ kpc and $M_\bullet = 4.31 \pm 0.36 \times 10^6 M_\odot$ for $R_0 = 8.33$ kpc, as determined by Gillessen et al. (2009) from stellar orbits around Sgr A*. Figure 2.12 shows the 1σ to 3σ contours of marginalized χ^2 for (R_0, M_\bullet) jointly from stellar orbits (Gillessen et al., 2009), for the NSC model of this paper, and for the combined modeling of both data sets. The figure shows that both analyses are mutually consistent. When marginalized over M_* and the respective other parameter, the combined modeling gives, for each parameter alone, $R_0 = 8.33 \pm 0.11$ kpc and $M_\bullet = 4.23 \pm 0.14 \times 10^6 M_\odot$. We note that these errors for R_0 and M_\bullet are both dominated by the distance error from the NSC modeling. Thus our estimated additional systematic error of 0.1 kpc for R_0 in the NSC modeling translates to a similar additional error in the combined R_0 measurement and, through the SMBH mass-distance relation given in Gillessen et al (2009), to an additional uncertainty $\simeq 0.1 \times 10^6 M_\odot$ in M_\bullet . We see that the combination of the NSC and S-star orbit data is a powerful means for decreasing the degeneracy between the SMBH mass and Galactic center distance in the S-star analysis.

2.4.3 Two-integral distribution function for the NSC.

Now we have seen the success of fitting the semi-isotropic Jeans models to all three velocity dispersion profiles of the NSC, and determined its mass and distance parameters, we proceed to calculate two-integral (2I) distribution functions. We use the contour integral method of Hunter & Qian (1993, HQ) and Qian et al. (1995). A 2I DF is the logical, next-simplest generalization of isotropic spherical models. Finding a positive DF will ensure that our model is physical. Other possible methods to determine $f(E, L_z)$ include reconstructing the DF from moments (Magorrian, 1995), using series expansions as in Dehnen & Gerhard (1994), or grid-based quadratic programming as in Kuijken (1995). We find the HQ method the most suitable since it is a straightforward generalization of Eddington's formula. The contour integral is given by:

$$f_+(E, L_z) = \frac{1}{4\pi^2 i \sqrt{2}} \oint \frac{d\xi}{(\xi - E)^{1/2}} \tilde{\rho}_{11} \left(\xi, \frac{L_z^2}{2(\xi - E)^{1/2}} \right) \quad (2.30)$$

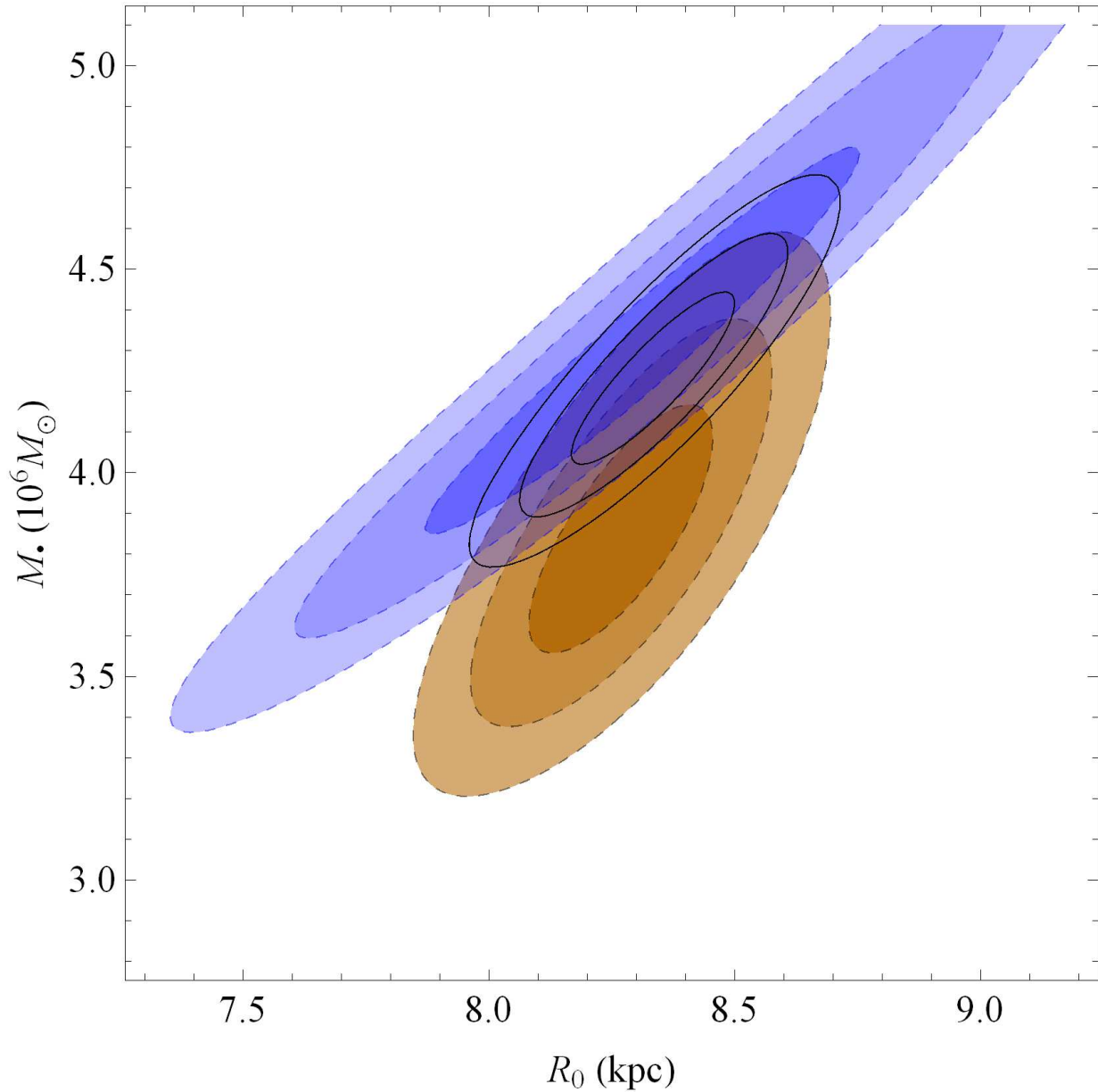


Figure 2.12: Blue: χ^2 contours in the (R_0, M_\bullet) plane from stellar orbits of S-stars, as in Figure 15 of Gillessen et al. (2009), at confidence levels corresponding to 1σ , 2σ , 3σ for the joint probability distribution. Brown: Corresponding χ^2 contours from this work. Black: Combined contours after adding the χ^2 values.

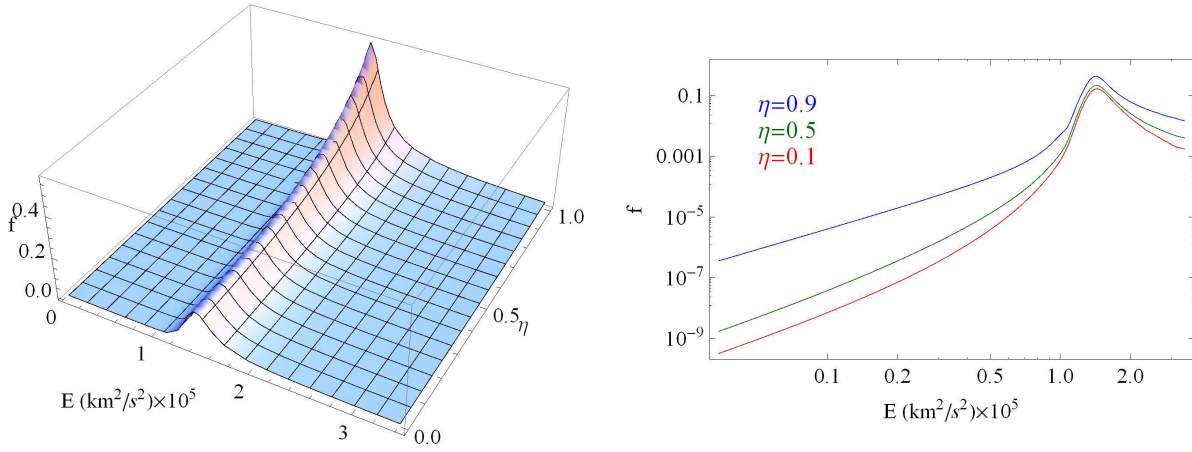


Figure 2.13: We used the HQ algorithm to calculate the 2I-DF for our best Jeans model. The left plot shows the DF in E and $\eta = L_z/L_{z\max}(E)$ space. The DF is an increasing function of η . The right plot shows the projection of the DF on energy space for several values of η . The shape resembles that of the spherical case in Figure 2.4.

where $\tilde{\rho}_{11}(\Psi, R) = \frac{\partial^2}{\partial \Psi^2} \rho(\Psi, R)$. Equation (2.30) is remarkably similar to Eddington's formula. Like in the spherical case the DF is even in L_z . The integration for each (E, L_z) pair takes place on the complex plane of the potential ξ following a closed path (i.e. an ellipse) around the special value Ψ_{env} . For more information on the implementation and for a minor improvement over the original method see Appendix A. We find that a resolution of (120×60) logarithmically placed cells in the (E, L_z) space is adequate to give us relative errors of the order of 10^{-3} when comparing with the zeroth moment, i.e., the density, already known analytically, and with the second moments, i.e., the velocity dispersions from Jeans modeling.

The gravitational potential is already known from equations (2.20) and (2.21). For the parameters (cluster mass, black hole mass, distance) we use the values given in (2.25). Figure 2.13 shows the DF in (E, L_z) space. The shape resembles that of the spherical case (Fig. 2.4). The DF is a monotonically increasing function of $\eta = L_z/L_{z\max}(E)$ and declines for small and large energies. The DF contains information about all moments and therefore we can calculate the projected velocity profiles (i.e., velocity distributions, hereafter abbreviated VPs) in all directions. The normalized VP in the line-of-sight (los) direction y is

$$VP(v_{\text{los}}; x, z) = \frac{1}{\Sigma} \iiint_{E>0} f(E, L_z) dv_x dv_z dy. \quad (2.31)$$

Using polar coordinates in the velocity space $(v_x, v_z) \rightarrow (v_{\perp}, \varphi)$ where $v_x = v_{\perp} \cos \varphi$ and $v_z = v_{\perp} \sin \varphi$ we find

$$VP(v_{\text{los}}; x, z) = \frac{1}{2\Sigma} \int_{y_1}^{y_2} dy \int_0^{2\Psi - v_{\text{los}}^2} dv_{\perp}^2 \int_0^{2\pi} d\varphi f(E, L_z) \quad (2.32)$$

where

$$\begin{aligned} E &= \Psi(x, y, z) - \frac{1}{2}(v_{\text{los}}^2 + v_{\perp}^2), \\ L_z &= xv_{\text{los}} - yv_{\perp} \cos \varphi. \end{aligned} \tag{2.33}$$

and $y_{1,2}$ are the solutions of $\Psi(x, y, z) - v_{\text{los}}^2/2 = 0$. Following a similar path we can easily find the corresponding integrals for the VPs in the l and b directions.

The typical shape of the VPs in the l and b directions within the area of interest ($r < 100''$) is shown in Figure 2.14. We notice the characteristic two-peak shape of the VP along l that is caused by the near-circular orbits of the flattened system. Because the front and the back of the axisymmetric cluster contribute equally, the two peaks are mirror-symmetric, and adding rotation would not change their shapes.

The middle panels of Figure 2.15 and Figures 2.21 and 2.22 in Appendix B show how our best model (with parameters as given in (2.19) and (2.27)) predicts the observed velocity histograms for various combinations of cells. The reduced χ^2 for each histogram is also provided. The prediction is very good both for the VPs in v_l and v_b . Specifically, for the l proper motions our flattened cluster model predicts the two-peak structure of the data pointed out by several authors (Trippe et al., 2008; Schödel et al., 2009; Fritz et al., 2014). In order to calculate the VP from the model for each cell we averaged over the VP functions for the center of each cell weighted by the number of stars in each cell and normalized by the total number of stars in all the combined cells.

Figure 2.15 compares two selected v_l -VPs for our two main models with the data. The left column shows how the observed velocity histograms (VHs) for corresponding cells compare to the model VPs for the less flattened model with parameters given in (2.27) and (2.28), the middle column compares with the same VPs from our best model with parameters given in (2.19) and (2.25). Clearly, the more flattened model with $q_1 = 0.73$ fits the shape of the data much better than the more spherical model with $q_1 = 0.85$, justifying its use in Section 2.4.2.

This model is based on an even DF in L_z and therefore does not yet have rotation. To include rotation, we will (in Section 4.4) add an odd part to the DF, but this will not change the even parts of the model's VPs. Therefore, we can already see whether the model is also a good match to the observed los velocities by comparing it to the even parts of the observed los VHs. This greatly simplifies the problem since we can think of rotation as independent, and can therefore adjust it to the data as a final step. Figure 2.23 shows how the even parts of the VHs from the los data compare with the VPs of the 2I model. Based on the reduced χ^2 , the model provides a very good match. Possible systematic deviations are within the errors. The los VHs are broader than those in the l direction because the los data contain information about rotation (the broader the even part of the symmetrized los VHs, the more rotation the system possesses, and in extreme cases they would show two peaks).

2.4.4 Adding rotation to the axisymmetric model: is the NSC an isotropic rotator?

As in the spherical case, to model the rotation we add an odd part in L_z to the initial even part of the distribution function, so that the final DF takes the form $f(E, L_z) = (1 + g(L_z))f(E, L_z)$. We use again equation (2.14); this adds two additional parameters (κ, F) to the DF. Equation (2.16) gives the mean los velocity vs Galactic longitude. In order to constrain the parameters (κ, F) we

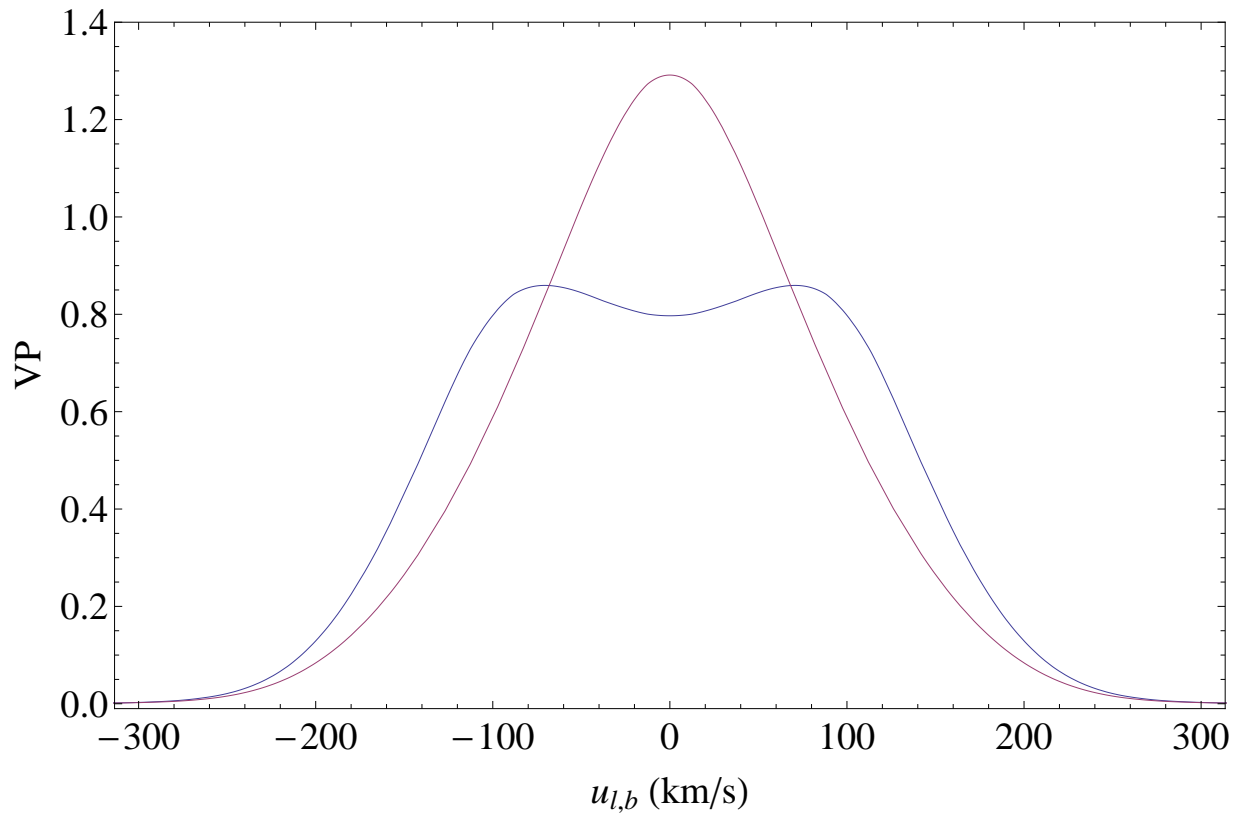


Figure 2.14: Typical velocity distributions for l and b -velocities within the area of interest ($r < 100''$). The red line shows the VPs in the b direction, the blue line in the l direction. The VPs along l show the characteristic two-peak-shape pointed out from the data by several authors (Schödel et al., 2007; Trippe et al., 2008; Fritz et al., 2014).

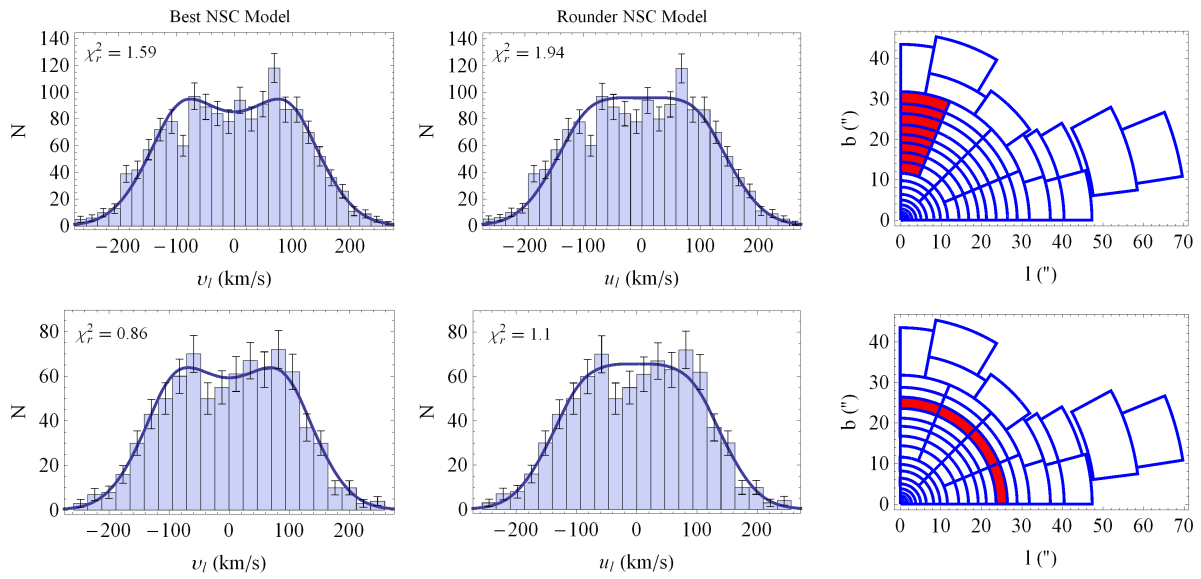


Figure 2.15: Predicted distributions of v_l velocity compared to the observed histograms. In each row, model VPs and observed VHs are shown averaged over the cells indicated in red in the right column, respectively. Left column: predictions for the less flattened model which we use as an illustration model, i.e., for parameters given in (26) and (27). Middle column: predicted VPs for our best model with parameters given in (18) and (24). This more flattened model with $q_1 = 0.73$ fits the data much better than the rounder cluster model with $q_1 = 0.85$.

fitted the mean los velocity from equation (2.16) to the los velocity data for all cells in Fig. 2.2. The best parameter values resulting from this 2D-fitting are $\kappa = 2.8 \pm 1.7$, $F = 0.85 \pm 0.15$ and $\chi_r^2 = 1.25$. Figure 2.24 shows that the VPs of this rotating model compare well with the observed los VHS.

An axisymmetric system with a DF of the form $f(E, L_z)$ is an isotropic rotator when all three eigenvalues of the dispersion tensor are equal (Binney & Tremaine, 2008) and therefore

$$\overline{v_\varphi^2} = \overline{v_\varphi^2} - \overline{v_R^2}. \quad (2.34)$$

In order to calculate $\overline{v_\varphi}$ from equation (2.34) it is not necessary for the DF to be known since $\overline{v_\varphi^2}$ and $\overline{v_R^2}$ are already known from the Jeans equations (2.22). Figure 2.16 shows the fitted u_{los} velocity from the DF against the isotropic rotator case calculated from equation (2.34), together with the mean los velocity data. The two curves agree well within $\sim 30''$, and also out to $\sim 200''$ they differ only by ~ 10 km/s. Therefore according to our best model the NSC is close to an isotropic rotator, with slightly lower rotation and some tangential anisotropy outwards of $30''$.

2.5 Discussion

In this work we presented a dynamical analysis of the Milky Way’s nuclear star cluster (NSC), based on $\sim 10'000$ proper motions, $\sim 2'700$ radial velocities, and new star counts from the companion paper of Fritz et al. (2014). We showed that an excellent representation of the kinematic data can be obtained by assuming a constant mass-to-light ratio for the cluster, and modeling its dynamics with axisymmetric two-integral distribution functions (2I-DFs), $f(E, L_z)$. The DF modeling allows us to see whether the model is physical, i.e., whether the DF is positive, and to model the proper motion (PM) and line-of-sight (los) velocity histograms (VHS). One open question until now has been the nature of the double peaked VHS of the v_l -velocities along Galactic longitude, and the bell-shaped VHS of v_b along Galactic latitude, which cannot be fitted by Gaussians (Schödel et al., 2009). Our 2I DF approximation of the NSC gives an excellent prediction for the observed shapes of the v_l -, v_b , and v_{los} -VHS. The models show that the double-peaked shape of the v_l -VHS is a result of the flattening of the NSC, and suggest that the cluster’s dynamical structure is close to an isotropic rotator. Because both PMs and los-velocities enter the dynamical models, we can use them also to constrain the distance to the GC, the mass of the NSC, and the mass of the Galactic centre black hole. To do this efficiently, we used the semi-isotropic Jeans equations corresponding to 2I-DFs. In this section, we discuss these issues in more detail.

2.5.1 The dynamical structure of the NSC

The star count map derived in Fritz et al. (2014) suggests two components in the NSC density profile, separated by an inflection point at about $\sim 200'' \sim 8$ pc (see Fig. 2.7 above). To account for this we constructed a two-component dynamical model for the star counts in which the two components are described as independent γ -models. The inner, rounder component can be considered as the proper NSC, as in Fritz et al. (2014), while the outer, much more flattened component may represent the inner parts of the nuclear stellar disk (NSD) described in Launhardt et al. (2002).

The scale radius of the inner component is $\sim 100''$, close to the radius of influence of the SMBH, $r_h \sim 90''$ (Alexander, 2005). The profile flattens inside $\sim 20''$ to a possible core (Buchholz

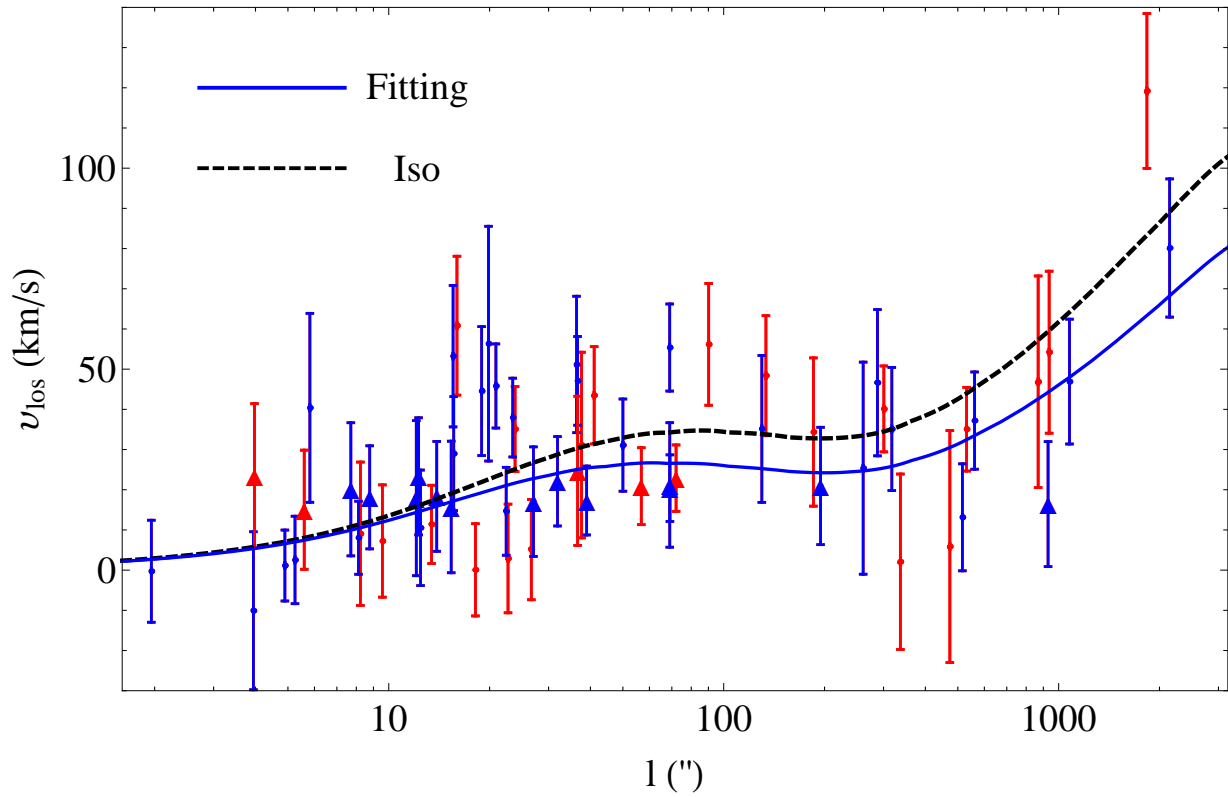


Figure 2.16: Best fitting model from the 2I DF compared to the isotropic rotator model. Each data point corresponds to a cell from Figure 2.2. Velocities at negative l have been folded over with their signs reversed and are shown in red. The plot also includes the maser data at $R_s > 100''$. The predictions of both models are computed for $b = 20''$. For comparison, cells with centers between $b = 15''$ and $b = 25''$ are highlighted with full triangles.

et al., 2009; Fritz et al., 2014) but the slope of the three-dimensional density profile for the inner component is not well-constrained.

The flattening for the inner NSC component inferred from star counts is $q_1 = 0.73 \pm 0.04$, very close to the value of $q = 0.71 \pm 0.02$ found recently from Spitzer multi-band photometry (Schödel et al., 2014). It is important that these determinations agree with the dynamical flattening of our best Jeans dynamical models: the dynamical flattening is robust because it is largely determined by the ratio of σ_b/σ_l and the tensor virial theorem. Because star counts, photometric, and dynamical values for the inner NSC flattening agree, this parameter can now be considered securely determined.

Assuming constant mass-to-light ratio for the NSC, we found that a 2I-DF model gives an excellent description of the proper motion and los velocity dispersions and VHS, in particular of the double-peaked distributions in the v_l -velocities. This double-peaked structure is a direct consequence of the flattening of the star cluster; the detailed agreement of the model VPs with the observed histograms therefore confirms the value $q_1 = 0.73$ for the inner cluster component. For an axisymmetric model rotation cannot be seen directly in the proper motion VHS when observed edge-on, as is the case here, but is apparent only in the los velocities. When a suitable odd part of the DF is added to include rotation, the 2I-DF model also gives a very good representation of the skewed los VHS. From the amplitude of the required rotation we showed that the NSC can be approximately described as an isotropic rotator model, rotating slightly slower than that outside $\sim 30''$.

Individual VHS are generally fitted by this model within the statistical errors, but on closer examination the combined v_l VHS show a slightly lower peak at negative velocities, as already apparent in the global histograms of Trippe et al. (2008); Schödel et al. (2009). Fig. 2.17 suggests that differential extinction of order ~ 0.2 mag within the cluster may be responsible for this small systematic effect, by causing some stars from the back of the cluster to fall out of the sample. The dependence of mean extinction on v_l independently shows that the NSC must be rotating, which could otherwise only be inferred from the los velocities. In subsequent work, we will model the effect of extinction on the inferred dynamics of the NSC. This will then also allow us to estimate better how important deviations from the 2I-dynamical structure are, i.e., whether three-integral dynamical modeling (e.g., De Lorenzi et al., 2013) would be worthwhile.

2.5.2 Mass of the NSC

The dynamical model results in an estimate of the mass of the cluster from our dataset. Our fiducial mass value is $M_*(m < 100'') = (7.73 \pm 0.31|_{\text{stat}} \pm 0.8|_{\text{syst}}) \times 10^6 M_\odot$ interior to a spheroidal major axis distance $m = 100''$. This corresponds to an enclosed mass within 3-dimensional radius $r = 100''$ of $M_*(r < 100'') = (8.94 \pm 0.31|_{\text{stat}} \pm 0.9|_{\text{syst}}) \times 10^6 M_\odot$.

The fiducial mass $M_*(r < 100'')$ for the best axisymmetric model is larger than that obtained with spherical models. The constant M/L spherical model with density parameters as in Section 3, for $R_0 = 8.3$ kpc and the same black hole mass has $M_*(r < 100'') = 6.6 \times 10^6 M_\odot$.

There are two reasons for this difference: (i) At $\sim 50''$ where the model is well-fixed by kinematic data the black hole still contributes more than half of the interior mass. In this region, flattening the cluster at constant mass leaves σ_l and σ_{los} approximately constant, but decreases σ_b to adjust to the shape. To fit the same observed data, the NSC mass must be increased. (ii) Because of the increasing flattening with radius, the average density of the axisymmetric

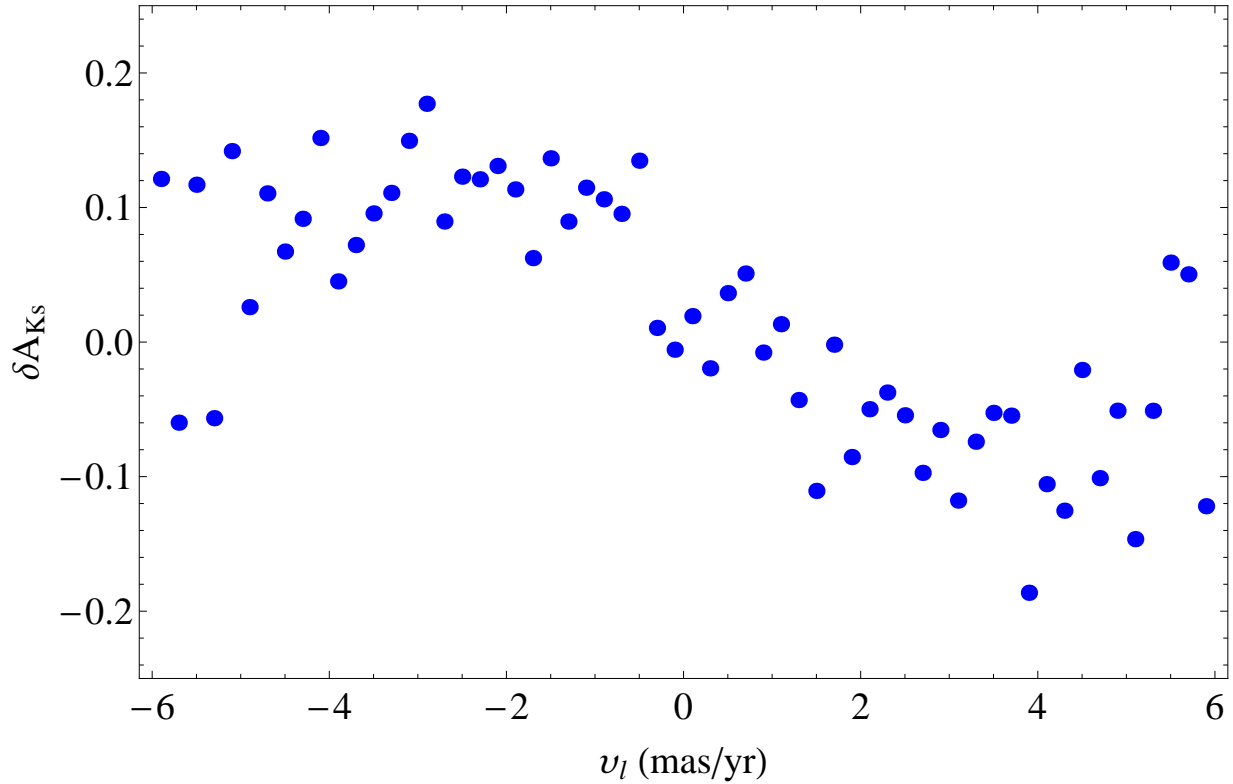


Figure 2.17: Average differential extinction of nuclear cluster stars plotted as a function of v_l proper motion. The differential extinction is inferred from the difference in the color of a star to the median color of its 16 nearest neighbours, using the extinction law of Fritz et al. (2011), and correcting also for the weak color variation with magnitude. For this plot we use all the proper motion stars in the central and extended fields of Fritz et al. (2014) and bins of 0.2 mas/yr. The differential extinction is larger for stars with negative l -proper motions which occur preferentially at the back of the cluster.

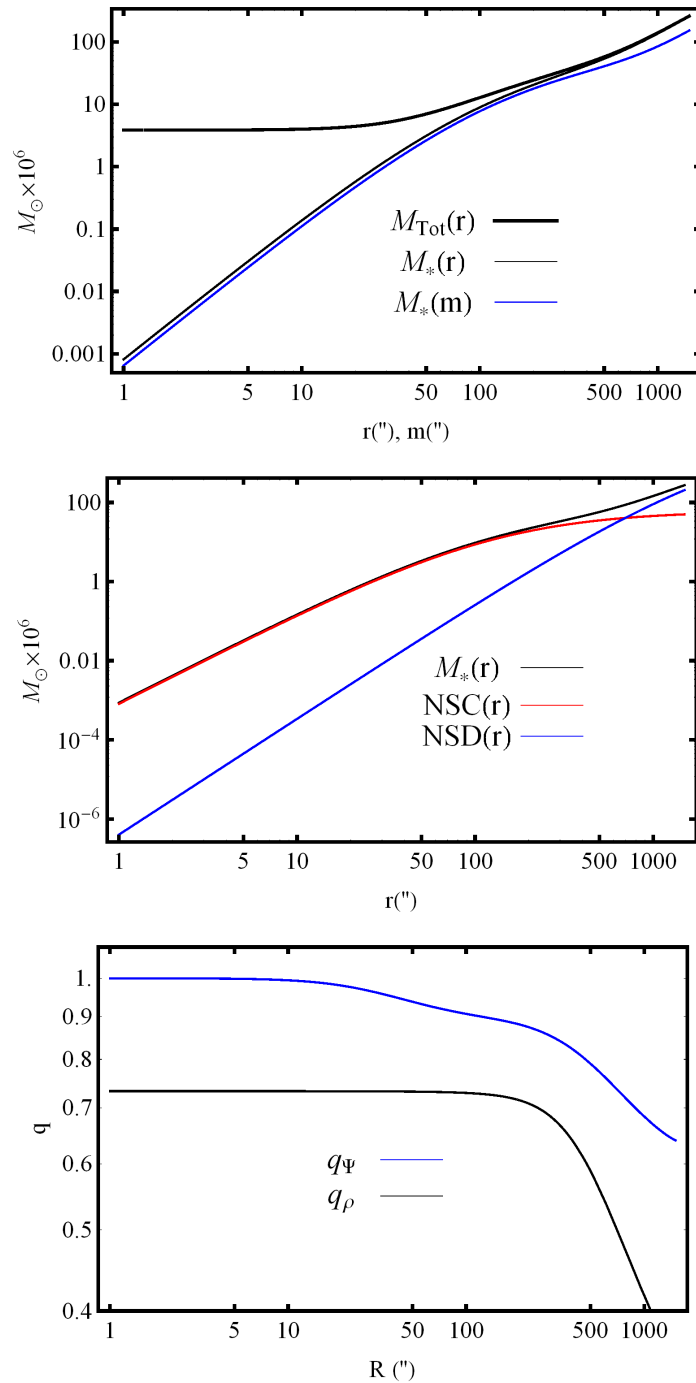


Figure 2.18: Upper panel: Enclosed mass of the NSC, as function of three-dimensional radius r and spheroidal radius m , and total enclosed mass including the black hole. Middle panel: Enclosed mass of the inner component of the NSC (inner component M_1), the NSD (outer component M_2), and total enclosed stellar mass, as function of three-dimensional radius r . Lower panel: Axis ratios of the stellar density and total potential as functions of the cylindrical radius R .

model decreases faster than that of the spherical density fit; thus for the same observed velocity dispersion profiles a larger binding mass for the NSC is required.

Figure 2.18 shows the enclosed stellar mass within the spheroidal radius m as in equation (2.26), as well as the mass within the spherical radius r . E.g., the mass within 1 pc ($25''$) is $M_*(r < 1\text{pc} \sim 25'') = 0.89 \times 10^6 M_\odot$. This is compatible with the spherical modeling of Schödel et al. (2009) who gave a range of $0.6 - 1.7 \times 10^6 M_\odot$, rescaled to $R_0 = 8.3$ kpc, with the highest mass obtained for their isotropic, constant M/L model. According to Fig. 2.18, at $r \simeq 30'' = 1.2$ pc the NSC contributes already $\simeq 25\%$ of the interior mass ($\simeq 45\%$ at $r \simeq 50'' = 2$ pc), and beyond $r \simeq 100'' = 4$ pc it clearly dominates.

An important point to note is that the cluster mass does not depend on the net rotation of the cluster but only on its flattening. This is because to add rotation self-consistently to the model we need to add an odd part to the DF which does not affect the density or the proper motion dispersions σ_l and σ_b .

Our NSC mass model can be described as a superposition of a moderately flattened nuclear cluster embedded in a highly flattened nuclear disk. The cumulative mass distributions of the two components are shown in the middle panel of Figure 2.18. The NSD starts to dominate at about $800''$ which is in good agreement with the value found by Launhardt et al. (2002).

Approximate local axis ratios for the combined density and for the total potential including the central black hole are shown in the lower panel of Fig. 2.18. Here we approximate the axial ratio of the density at radius R by solving the equation $\rho(R, 0) = \rho(0, z)$ for z and writing $q_\rho = z/R$, and similarly for q_Ψ . The density axis ratio $q_\rho(R)$ shows a strong decrease between the regions dominated by the inner and outer model components. The equipotentials are everywhere less flattened. At the center, $q_\Psi = 1$ because of the black hole; the minimum value is not yet reached at $1000''$. Therefore, we can define the NSC proper as the inner component of this model, similar to Fritz et al. (2014).

The total mass of the inner component, $M_1 = 6.1 \times 10^7 M_\odot$ (Section 2.4.2), is well-determined within similar relative errors as $M_*(m < 100'')$. However, identifying M_1 with the total mass of the Galactic NSC at the center of the nuclear disk has considerable uncertainties: because the outer NSD component dominates the surface density outside $100'' - 200''$, the NSC density profile slope at large radii is uncertain, and therefore the part of the mass outside $\sim 200''$ ($\sim 64\%$ of the total) is also uncertain. A minimal estimate for the mass of the inner NSC component is its mass within $200''$ up to where it dominates the star counts. This gives $M_{\text{NSC}} > 2 \times 10^7 M_\odot$.

Finally, we use our inferred dynamical cluster mass to update the K-band mass-to-light ratio of the NSC. The best-determined mass is within $100''$. Comparing our $M_*(r < 100'') = (8.94 \pm 0.31)_{\text{stat}} \pm 0.9_{\text{sys}} \times 10^6 M_\odot$ with the K-band luminosity of the old stars derived in Fritz et al. (2014), $L_{100''} = (12.12 \pm 2.58) \times 10^6 L_{\odot, \text{Ks}}$, we obtain $M/L_{\text{Ks}} = (0.76 \pm 0.18) M_\odot / L_{\odot, \text{Ks}}$. The error is dominated by the uncertainty in the luminosity (21%, compared to a total 10% in mass from adding statistical and systematic errors in quadrature). The inferred range is consistent with values expected for mostly old, solar metallicity populations with normal IMF (e.g., Courteau et al., 2013; Fritz et al., 2014).

2.5.3 Evolution of the NSC

After ~ 10 half mass relaxation times t_{rh} a dense nuclear star cluster will eventually evolve to form a Bahcall-Wolf cusp with slope $\gamma = 7/4$ (Merritt, 2013); for rotating dense star clusters

around black holes this was studied by Fiestas & Spurzem (2010). The minimum allowable inner slope for a spherical system with a black hole to have a positive DF is $\gamma = 0.5$. From the data it appears that the Galactic NSC instead has a core (Buchholz et al., 2009; Fritz et al., 2014), with the number density possibly even decreasing very close to the center ($r < 0.3$ pc). This is far from the expected Bahcall-Wolf cusp, indicating that the NSC is not fully relaxed. It is consistent with the relaxation time of the NSC being of order 10 Gyr everywhere in the cluster (Merritt, 2013).

From Fig. 2.16 we see that the rotational properties of the Milky Way’s NSC are close to those of an isotropic rotator. Fiestas et al. (2012) found that relaxation in rotating clusters causes a slow ($\sim 3t_{rh}$) evolution of the rotation profile. Kim et al. (2008) found that it also drives the velocity dispersions towards isotropy; in their initially already nearly isotropic models this happens in $\sim 4t_{rh}$. On a similar time-scale the cluster becomes rounder (Einsel & Spurzem, 1999). Comparing with the NSC relaxation time suggests that these processes are too slow to greatly modify the dynamical structure of the NSC, and thus that its properties were probably largely set up at the time of its formation.

The rotation-supported structure of the NSC could be due to the rotation of the gas from which its stars formed, but it could also be explained if the NSC formed from merging of globular clusters. In the latter model, if the black hole is already present, the NSC density and rotation after completion of the merging phase reflects the distribution of disrupted material in the potential of the black-hole (e.g. Antonini et al., 2012). Subsequently, relaxation would lead to shrinking of the core by a factor of ~ 2 in 10 Gyr towards a value similar to that observed (Merritt, 2010). In the simulations of Antonini et al. (2012), the final relaxed model has an inner slope of $\gamma = 0.45$, not far from our models (note that in flattened semi-isotropic models the minimum allowed slope for the density is also 0.5 (Qian et al., 1995)). Their cluster also evolved towards a more spherical shape, however, starting from a configuration with much less rotation and flattening than we inferred here for the present Milky Way NSC. Similar models with a net rotation in the initial distribution of globular clusters could lead to a final dynamical structure more similar to the Milky Way NSC.

2.5.4 Distance to the Galactic center

From our large proper motion and los velocity datasets, we obtained a new estimate for the statistical parallax distance to the NSC using axisymmetric Jeans modeling based on the cluster’s inferred dynamical structure. From matching our best dynamical model to the proper motion and los velocity dispersions within approximately $|l|, |b| < 50''$, we found $R_0 = 8.27 \pm 0.09|_{\text{stat}} \pm 0.1|_{\text{syst}}$ kpc. The statistical error is very small, reflecting the large number of fitted dispersion points. The systematic modeling error was estimated from uncertainties in the density structure of the NSC, as discussed in Section 2.4.2.

Our new distance determination is much more accurate than that of Do et al. (2013) based on anisotropic spherical Jeans models of the NSC, $R_0 = 8.92^{+0.58}_{-0.58}$ kpc, but is consistent within their large errors. We believe this is mostly due to the much larger radial range we modeled, which leaves less freedom in the dynamical structure of the model.

The new value for R_0 is in the range $R_0 = 8.33 \pm 0.35$ kpc found by Gillessen et al. (2009) from analyzing stellar orbits around Sgr A*. A joint statistical analysis of the NSC data with the orbit results of Gillessen et al. (2009) gives a new best value and error $R_0 = 8.33 \pm 0.11$ kpc

(Fig. 2.12, Section 2.4.2). Our estimated systematic error of 0.1 kpc for R_0 in the NSC modeling translates to a similar additional uncertainty in this combined R_0 measurement.

Measurements of R_0 prior to 2010 were reviewed by Genzel et al. (2010). Their weighted average of direct measurements is $R_0 = 8.23 \pm 0.20 \pm 0.19$ kpc, where the first error is the variance of the weighted mean and the second the unbiased weighted sample variance. Two recent measurements give $R_0 = 8.33 \pm 0.05|_{\text{stat}} \pm 0.14|_{\text{syst}}$ kpc from RR Lyrae stars (Dekany et al., 2013) and $R_0 = 8.34 \pm 0.14$ kpc from fitting axially symmetric disk models to trigonometric parallaxes of star forming regions (Reid et al., 2014). These measurements are consistent with each other and with our distance value from the statistical parallax of the NSC, with or without including the results from stellar orbits around Sgr A*, and the total errors of all three measurements are similar, $\sim 2\%$.

2.5.5 Mass of the Galactic supermassive black hole

Given a dynamical model, it is possible to constrain the mass of the central black hole from 3D stellar kinematics of the NSC alone. With axisymmetric Jeans modeling we found $M_\bullet = (3.86 \pm 0.14|_{\text{stat}} \pm 0.4|_{\text{syst}}) \times 10^6 M_\odot$, where the systematic modeling error is estimated from the difference between models with different inner cluster flattening as discussed in Section 2.4.2. Within errors this result is in agreement with the black hole mass determined from stellar orbits around Sgr A* (Gillessen et al., 2009).

Our dataset for the NSC is the largest analyzed so far, and the axisymmetric dynamical model is the most accurate to date; it compares well with the various proper motion and line-of-sight velocity histograms. Nonetheless, future improvements may be possible if the uncertainties in the star density distribution and kinematics within $20''$ can be reduced, the effects of dust are incorporated, and possible deviations from the assumed 2I-axisymmetric dynamical structure are taken into account.

Several similar analyses have been previously made using spherical isotropic or anisotropic modeling. Trippe et al. (2008) used isotropic spherical Jeans modeling for proper motions and radial velocities in $1'' < R < 100''$; their best estimate is $M_\bullet \sim 1.2 \times 10^6 M_\odot$, much lower than the value found from stellar orbits. Schödel et al. (2009) constructed isotropic and anisotropic spherical broken power-law models, resulting in a black hole mass of $M_\bullet = 3.6^{+0.2}_{-0.4} \times 10^6 M_\odot$. However, Fritz et al. (2014) find $M_\bullet \sim 2.27 \pm 0.25 \times 10^6 M_\odot$, also using a power-law tracer density. They argue that the main reason for the difference to Schödel et al. (2009) is because their velocity dispersion data for $R > 15''$ are more accurate, and their sample is better cleaned for young stars in the central $R < 2.5''$. Assuming an isotropic spherical model with constant M/L, Fritz et al. (2014) find $M_\bullet \sim 4.35 \pm 0.12 \times 10^6 M_\odot$. Do et al. (2013) used 3D stellar kinematics within only the central 0.5 pc of the NSC. Applying spherical Jeans modeling, they obtained $M_\bullet = 5.76^{+1.76}_{-1.26} \times 10^6 M_\odot$ which is consistent with that derived from stellar orbits inside $1''$, within the large errors. However, in their modeling they used a very small density slope for the NSC, of $\gamma = 0.05$, which does not correspond to a positive DF for their quasi-isotropic model.

Based on this work and our own models in Section 4, the black hole mass inferred from NSC dynamics is larger for constant M/L models than for power law models, and it increases with the flattening of the cluster density distribution.

The conceptually best method to determine the black hole mass is from stellar orbits close to the black hole (Schödel et al., 2002; Ghez et al., 2008; Gillessen et al., 2009), as it requires only the

assumption of Keplerian orbits and is therefore least susceptible to systematic errors. Gillessen et al. (2009) find that the largest uncertainty in the value obtained for M_\bullet is due to the uncertainty in R_0 , and that M_\bullet scales as $M_\bullet \propto R_0^2$.¹⁹ Therefore using our improved statistical parallax for the NSC also leads to a more accurate determination of the black hole mass. A joint statistical analysis of the axisymmetric NSC modeling together with the orbit modeling of Gillessen et al. (2009) gives a new best value and error for the black hole mass, $M_\bullet = (4.26 \pm 0.14) \times 10^6 M_\odot$ (see Fig. 2.12, Section 2.4.2). An additional systematic error of 0.1 kpc for R_0 in the NSC modeling, through the BH mass-distance relation given in Gillessen et al (2009), translates to an additional uncertainty $\simeq 0.1 \times 10^6 M_\odot$ in M_\bullet .

Combining this result with the mass modeling of the NSC, we can give a revised value for the black hole influence radius r_{infl} , using a common definition of r_{infl} as the radius where the interior mass $M(< r)$ of the NSC equals twice the black hole mass (Merritt, 2013). Comparing the interior mass profile in Fig. 2.18 as determined by the dynamical measurement with $M_\bullet = 4.26 \times 10^6 M_\odot$, we obtain $r_{\text{infl}} \simeq 94'' = 3.8$ pc.

The Milky Way is one of some 10 galaxies for which both the masses of the black hole and of the NSC have been estimated (Kormendy, 2013). From these it is known that the ratio of both masses varies widely. Based on the results above we estimate the Milky Way mass ratio $M_\bullet/M_{\text{NSC}} = 0.12 \pm 0.04$, with the error dominated by the uncertainty in the total NSC mass.

2.6 Conclusions

Our results can be summarized as follows:

- The density distribution of old stars in the central $1000''$ in the Galactic center can be well-approximated as the superposition of a spheroidal nuclear star cluster (NSC) with a scale length of $\sim 100''$ and a much larger nuclear disk (NSD) component.
- The difference between the proper motion dispersions σ_l and σ_b cannot be explained by rotation alone, but is a consequence of the flattening of the NSC. The dynamically inferred axial ratio for the inner component is consistent with the axial ratio inferred from the star counts which for our two-component model is $q_1 = 0.73 \pm 0.04$.
- The orbit structure of an axisymmetric two-integral DF $f(E, L_z)$ gives an excellent match to the observed double-peak in the v_l -proper motion velocity histograms, as well as to the shapes of the vertical v_b -proper motion histograms. Our model also compares well with the symmetrized (even) line-of-sight velocity histograms.
- The rotation seen in the line-of-sight velocities can be modelled by adding an odd part of the DF, and this shows that the dynamical structure of the NSC is close to an isotropic rotator model.
- Fitting proper motions and line-of-sight dispersions to the model determines the NSC mass within $100''$, the mass of the SMBH, and the distance to the NSC. From the star cluster data alone, we find $M_*(r < 100'') = (8.94 \pm 0.31)_{\text{stat}} \pm 0.9_{\text{syst}} \times 10^6 M_\odot$, $M_\bullet = (3.86 \pm 0.14)_{\text{stat}} \pm 0.4_{\text{syst}} \times 10^6 M_\odot$, and $R_0 = 8.27 \pm 0.09_{\text{stat}} \pm 0.1_{\text{syst}}$ kpc, where the estimated systematic errors account for additional uncertainties in the dynamical modeling. The fiducial mass of the NSC is larger than in previous spherical models. The total mass of

the NSC is significantly more uncertain due to the surrounding nuclear disk; we estimate $M_{\text{NSC}} = (2 - 6) \times 10^7 M_{\odot}$. The mass of the black hole determined with this approach is consistent with results from stellar orbits around Sgr A*. The Galactic center distance agrees well with recent accurate determinations from RR Lyrae stars and masers in the Galactic disk, and has similarly small errors.

- Combining our modeling results with the stellar orbit analysis of Gillessen et al. (2009), we find $M_{\bullet} = (4.23 \pm 0.14) \times 10^6 M_{\odot}$ and $R_0 = 8.33 \pm 0.11$ kpc. Because of the better constrained distance, the accuracy of the black hole mass is improved as well. Combining with the parameters of the cluster, the black hole radius of influence is 3.8 pc ($= 94''$) and the ratio of black hole to cluster mass is estimated to be 0.12 ± 0.04 .

2.7 Two-integral distributions functions

In this part we give implementation instructions for the 2I-DF algorithm of Hunter & Qian (1993, HQ). We will try to focus on the important parts of the algorithm and also on the tests that one has to make to ensure that the implementation works correctly. Our implementation is based on Qian et al. (1995) and made with Wolfram Mathematica. For the theory the reader should consider the original HQ paper.

We will focus on the even part of the DF and for the case where the potential at infinity, Ψ_{∞} , is finite and therefore can be set to zero. First one partitions the (E, η) space where $\eta \equiv L_z / L_{z \text{ max}}(E)$ takes values in $(0, 1)$. The goal of the HQ algorithm is to calculate the value of the DF on each of these points on a 2D grid and subsequently end up with a 3D grid where we can apply an interpolation to obtain the final smooth function $f(E, L_z)$. The energy values on the 2D grid are placed logarithmically within an interval of interest $[E_{\text{min}}, E_{\text{max}}]$ (higher E_{max} value is closer to the center) and the values of η are placed linearly between 0 and 1. Physically allowable E and L_z correspond to bound orbits in the potential Ψ and therefore $E > 0$. In addition at each energy there is a maximum physically allowed L_z corresponding to circular orbits with $z = 0$. This is given by the equations:

$$\begin{aligned} E &= \Psi(R_c^2, 0) + R_c^2 \frac{d\Psi(R_c^2, 0)}{dR^2} \Big|_{R=R_c} \\ L_z^2 &= -2R_c^4 \frac{d\Psi(R_c^2, 0)}{dR^2} \Big|_{R=R_c} \end{aligned} \quad (2.35)$$

where R_c is the radius of the circular orbit and the value $L_{z \text{ max}} \equiv L_z(R_c)$ is the maximum allowed value of L_z at a specific E . The $L_{z \text{ max}}(E)$ function can be found by solving the 1st equation for R_c and substituting in the second one therefore making a map $E \rightarrow L_{z \text{ max}}$. The value of the potential of a circular orbit with energy E is denoted by $\Psi_{\text{env}}(E)$ and can be found from $\Psi_{\text{env}}(E) = \Psi(R_c^2, 0)$ after solving the 1st of equation (2.35) for R_c . The value $\Psi_{\text{env}}(E)$ is important for evaluation of $f(E, L_z)$ and it is used in the contour of the complex integral.

To calculate the even part $f_+(E, L_z)$ of the DF for each point of the grid we have to apply the following complex contour integral on the complex ξ -plane using a suitable path:

$$f_+(E, L_z) = \frac{1}{4\pi^2 i \sqrt{2}} \oint \frac{d\xi}{(\xi - E)^{1/2}} \tilde{\rho}_{11} \left(\xi, \frac{L_z^2}{2(\xi - E)^{1/2}} \right) \quad (2.36)$$

where the subscript denotes the second partial derivative with respect to the first argument. A possible path for the contour is shown in figure 2.35. The loop starts at the point 0 on the lower side of the real ξ axis, crosses the real ξ axis at the point $\Psi_{\text{env}}(E)$ and ends at the upper side of real ξ axis. The parametrization of the path in general could be that of an ellipse:

$$\xi = \frac{1}{2}\Psi_{\text{env}}(E)(1 + \cos \theta) + ih \sin \theta, \quad -\pi \leq \theta \leq \pi \quad (2.37)$$

where h is the highest point of the ellipse. The value of h should not be too high because we want to avoid other singularities but not too low either to maintain the accuracy. We optimize our implementation by integrating along the upper part of the loop and multiply the real part of the result by 2 (this is because of the Schwarz reflection principle).

In order to calculate the integrand of the integral we need the following transformation:

$$\tilde{\rho}_{11}(\xi, R^2) = \frac{\rho_{22}(R^2, z^2)}{[\Psi_2(R^2, z^2)]^2} - \frac{\rho_2(R^2, z^2)\Psi_{22}(R^2, z^2)}{[\Psi_2(R^2, z^2)]^3} \quad (2.38)$$

in which each subscript denotes a partial differentiation with respect to z^2 . This equation is analogous to equation (2.7) of the spherical case. In addition $\tilde{\rho}$ is the density considered as a function of ξ and R^2 as opposed to R^2 and z^2 . The integrand of the contour integral 2.36 depends only on θ angle for a given (E, L_z) pair. Therefore we need the maps $R \rightarrow \xi$ and $z \rightarrow \xi$ in order to find the value of the integrand for a specific θ . The first map is given by $R^2 = \frac{1}{2}L_z^2/(\xi - E)$. The second is given by solving the equation $\xi = \Psi \left[\frac{L_z^2}{2(\xi - E)}, z^2 \right]$ for z . It is very important that the solution of the previous equation corresponds to the correct branch in which the integrand attains its physically achieved values. In order to achieve that for each pair $(E, L_{z \text{ max}})$ we start at the point $\xi = \Psi_{\text{env}}(E)(\theta = 0)$ which belongs to the physical domain and we look for the unique real positive solution. For the next point of the contour we use as initial guess the value of z from the previous step that we already know that belongs to the correct branch. Using this method we can calculate the integrand in several values of θ then make an interpolation of the integrand and calculate the value of the DF using numerical integration.

Figure 2.20 shows the shape of the DF for $\eta = 0.5$ for the potential we use in the fourth section of the paper for one value of h , using the aforementioned procedure. We notice that for large energies fluctuations of the DF appear. In order to solve this we introduce a minor improvement of the procedure, by generalizing the h value of the contour to an energy-dependent function $h = h(E)$. The $h(E)$ could be a simple step function that takes four or five different values. For our model the $h(E)$ function is a decreasing function of E . This means that the minor axis of the ellipse should decrease as the E increases to avoid such fluctuations. In general we can write $h = h(E, L_z)$ so that the contour depends both on E and L_z .

Once we implement the algorithm it is necessary to test it. Our first test is to check that the lower half of the integration path in figure 2.35 is the complex conjugate of the upper half. Probably the next most straightforward test is against the spherical case. It is possible to use the HQ algorithm to calculate a DF for spherical system. This DF should be equal to that obtained from Eddington's formula for the same parameters. After calculating our 2I-DF we compare its low-order moments with those of Jeans modeling. The 0th and 2nd moments of the DF (the 1st is 0 for the even part) are given from the integrals.

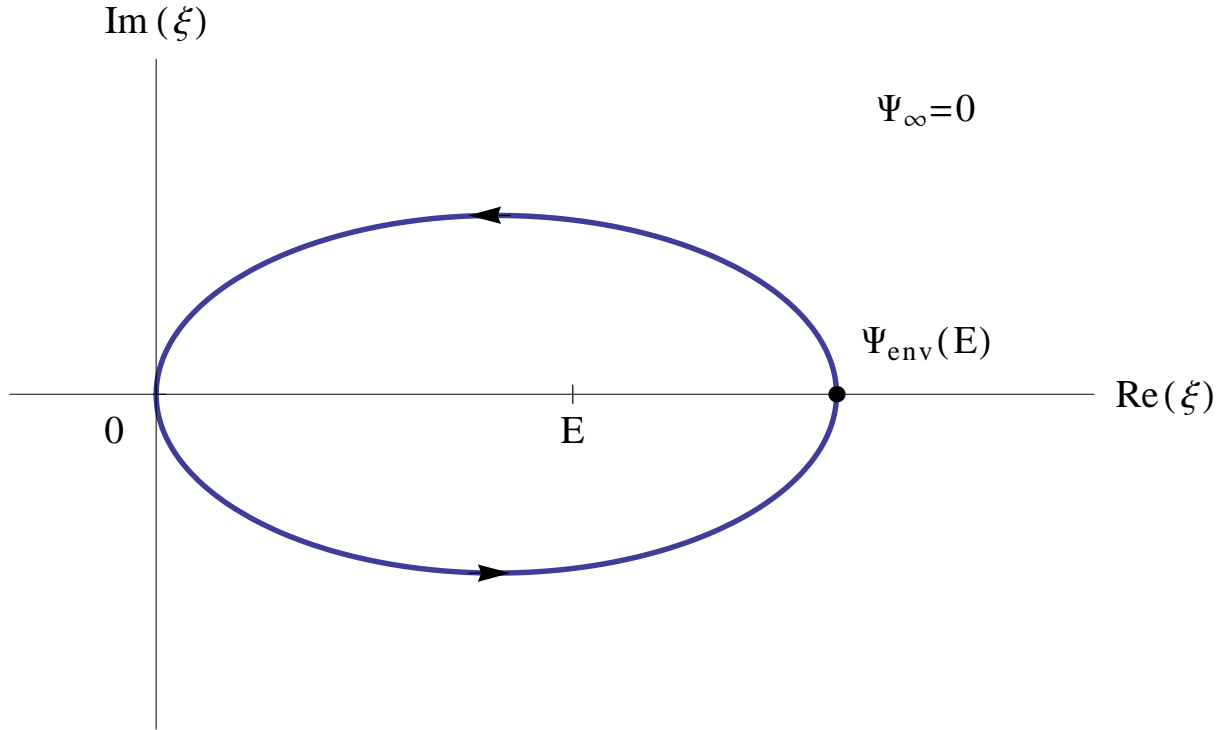


Figure 2.19: The contour used for the numerical evaluation of $f(E, L_z)$ for the case where $\Psi_\infty = 0$. We optimize our implementation by integrating only along the upper or lower part and then multiplying the result by 2.

$$\begin{aligned}
 \rho(R, z) &= \frac{4\pi}{R} \int_0^\Psi dE \int_0^{R\sqrt{2(\Psi-E)}} dL_z f_+(E, L_z) \\
 \rho(R, z)v_\varphi^2(R, z) &= \\
 \frac{4\pi}{R} \int_0^\Psi dE \int_0^{R\sqrt{2(\Psi-E)}} dL_z \left(\frac{L_z}{R}\right)^2 f_+(E, L_z) & \quad (2.39) \\
 \rho(R, z)v_z^2(R, z) &= \\
 \frac{2\pi}{R} \int_0^\Psi dE \int_0^{R\sqrt{2(\Psi-E)}} dL_z \left[2(\Psi - E) - \left(\frac{L_z}{R}\right)^2\right] f_+(E, L_z)
 \end{aligned}$$

Comparison with the 0th moment (density) is straight forward since the density is analytically known from the start. The 1st moments should be 0 within the expected error. In our implementation the error between Jeans modeling and the DF is of the order of 10^{-3} within the area of interest. An additional test would be to integrate the VPs over the velocity space. Since the VPs integrals are normalized with the surface density the integral of a VP over the whole velocity space should be 1 within the expected error.

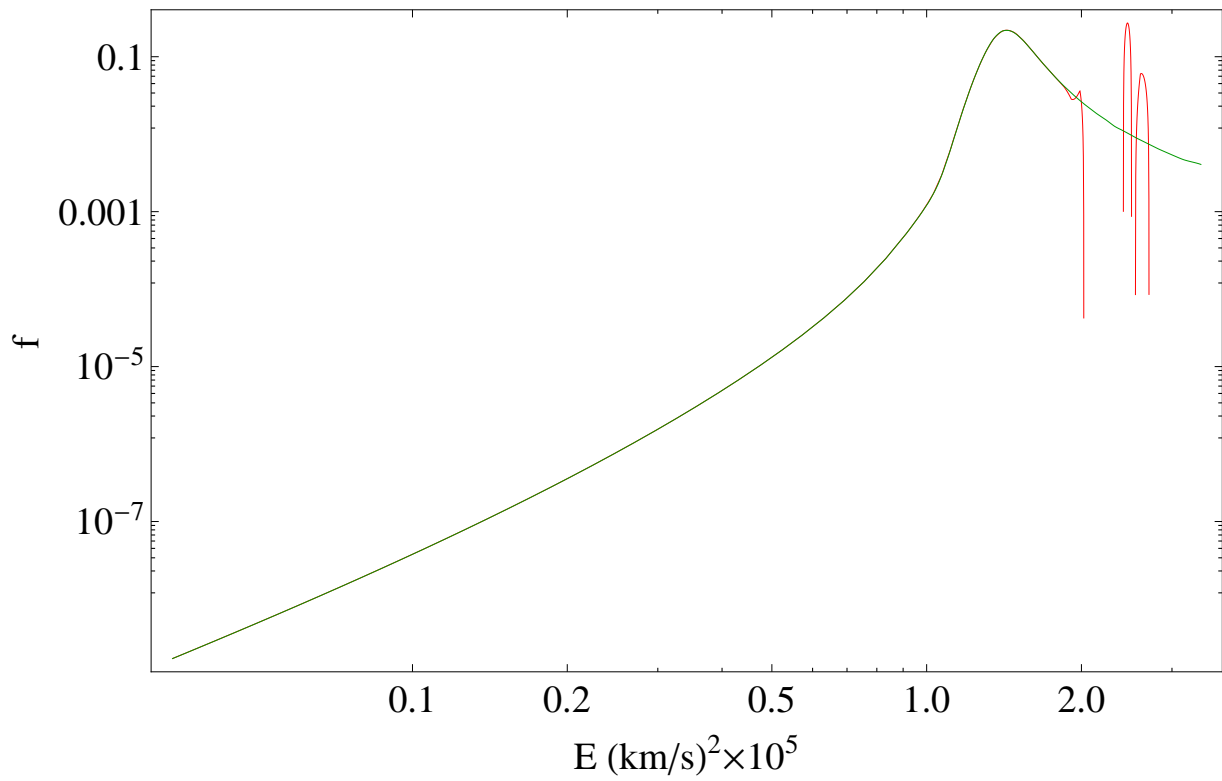


Figure 2.20: This shows our best DF for $\eta = 0.5$ (green line). Fluctuations (red lines) appear for large energies because we used a constant h for equation (2.37). To resolve this we used a more general function $h = h(E)$ or $h = h(E, L_z)$ even closer to the center.

2.8 Velocity histograms for the 2-I model

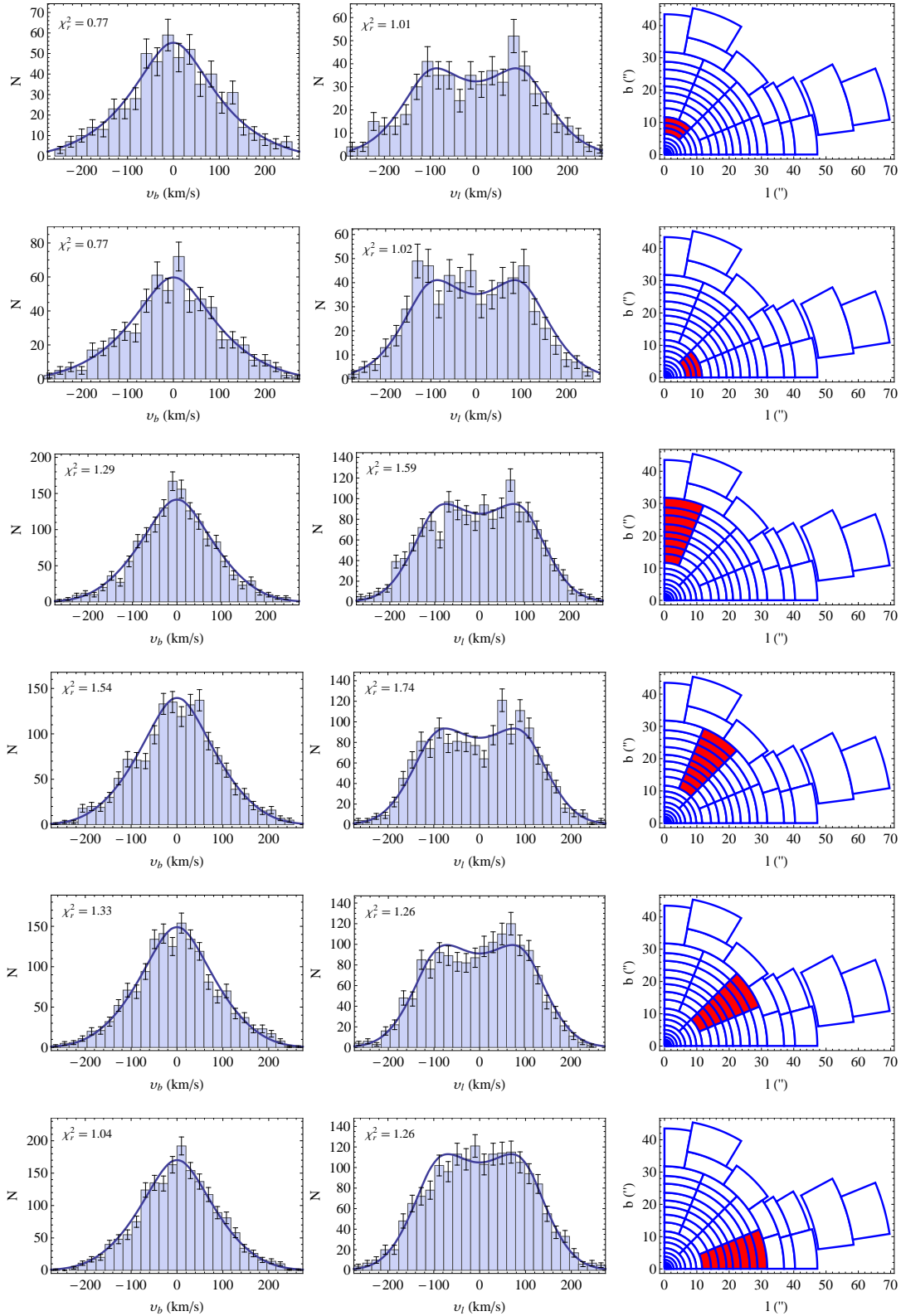


Figure 2.21: VHs and VPs in the l and b directions predicted by the 2I model in angular bins. The reduced χ^2 is also provided. The size of the bins is 0.6mas/yr (~ 23.6 km/s) for the upper two plots and 0.5mas/yr (~ 19.6 km/s) for the rest of the diagrams. The right column shows which cells have been used for the VHs and VPs.

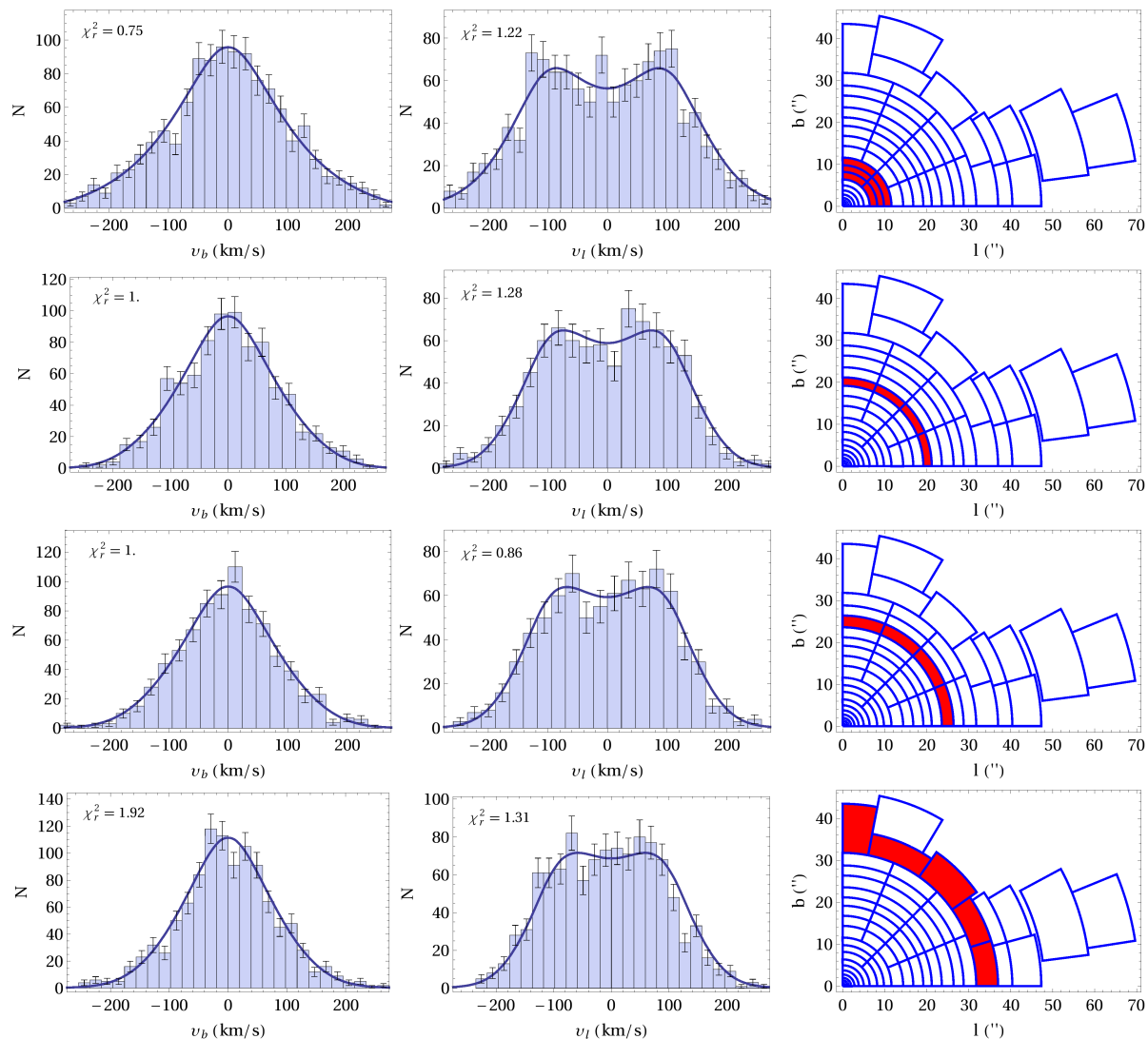


Figure 2.22: VHs and VPs in the l and b directions predicted by the 2I model in radial bins. The reduced χ^2 is also provided. The size of the bins is 0.5mas/yr (~ 19.6 km/s) for the 1st and 4th column and 0.6mas/yr (~ 23.6 km/s) for the rest of the diagrams. The right column shows which cells have been used for the VHs and VPs.

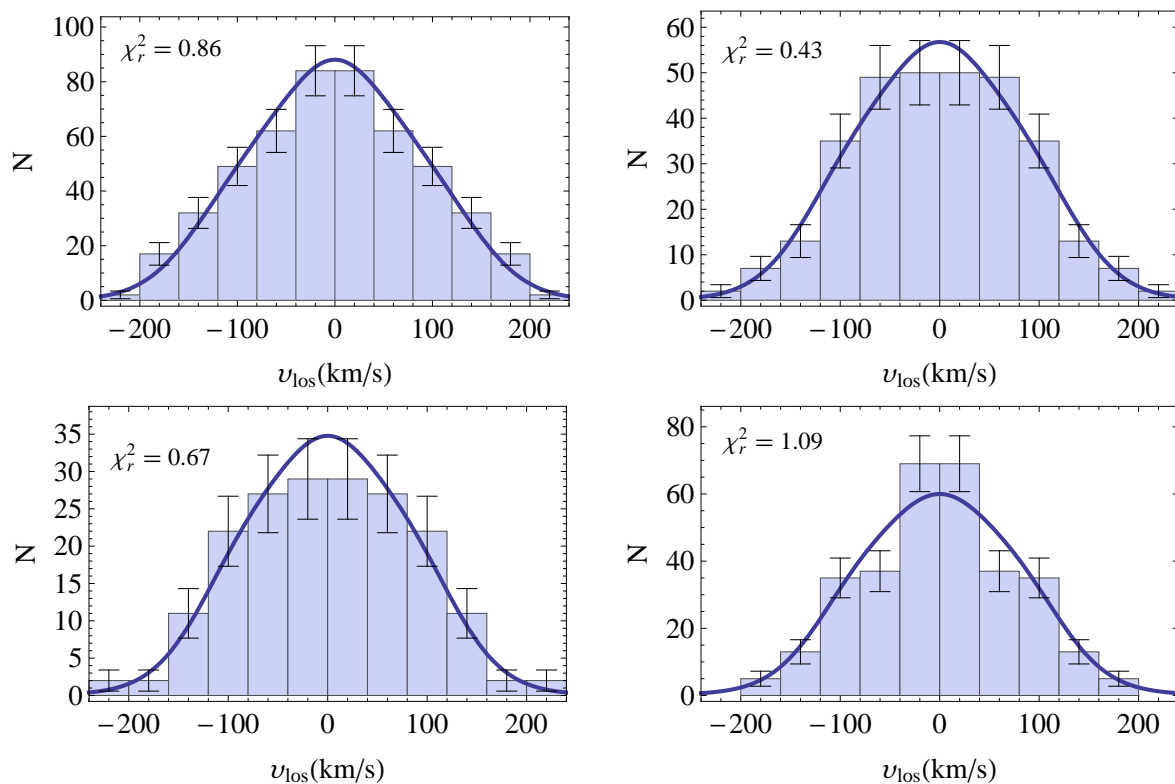


Figure 2.23: VHs for the symmetrized los data compared with the corresponding even VPs of the model. The reduced χ^2 is also provided. The size of the bins is 40km/s. For the upper left we use stars with $20'' < |l| < 30''$ and $|b| < 20''$, for the upper right stars with $30'' < |l| < 40''$ and $|b| < 20''$, for the bottom left $40'' < |l| < 50''$ and $|b| < 20''$, and for the bottom right $50'' < |l| < 70''$ and $|b| < 20''$.

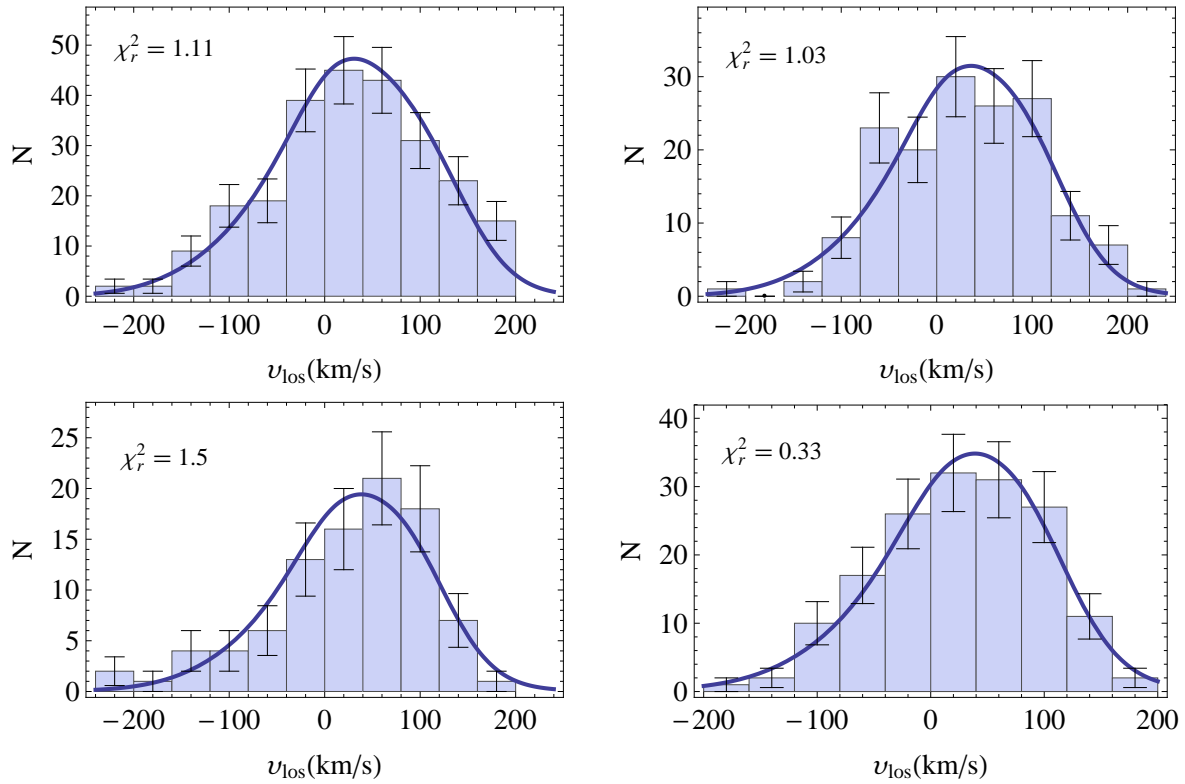


Figure 2.24: Los VHs compared with the corresponding VPs of the model including rotation. The reduced χ^2 is also provided. The size of the bins is 40km/s. For the upper left we use stars with $20'' < |l| < 30''$ and $|b| < 20''$, for the upper right stars with $30'' < |l| < 40''$ and $|b| < 20''$, for the bottom left $40'' < |l| < 50''$ and $|b| < 20''$, and for the bottom right $60'' < |l| < 80''$ and $|b| < 20''$.

Chapter 3

Dust within the old nuclear star cluster

Original publication: S. Chatzopoulos, O. Gerhard, T.K. Fritz, C. Wegg, S. Gillessen

Abstract: The mean absolute extinction towards the central parsec of the Milky Way is $A_K \simeq 3$ mag, including both foreground and Galactic center dust. Here we present a measurement of dust extinction *within* the Galactic old nuclear star cluster (NSC), based on combining differential extinctions of NSC stars with their v_l proper motions along Galactic longitude. Extinction within the NSC preferentially affects stars at its far side, and because the NSC rotates, this causes higher extinctions for NSC stars with negative v_l , as well as an asymmetry in the v_l -histograms. We model these effects using an axisymmetric dynamical model of the NSC in combination with simple models for the dust distribution. Comparing the predicted asymmetry to data for $\sim 7'100$ stars in several NSC fields, we find that dust associated with the Galactic center mini-spiral with extinction $A_K \simeq 0.15-0.8$ mag explains most of the data. The largest extinction $A_K \simeq 0.8$ mag is found in the region of the Western arm of the mini-spiral. Comparing with total A_K determined from stellar colors, we determine the extinction in front of the NSC. Finally, we estimate that for a typical extinction of $A_K \simeq 0.4$ the statistical parallax of the NSC changes by $\sim 0.4\%$.

3.1 Introduction

Nuclear star clusters (NSC) are located at the centers of most spiral galaxies (Carollo et al., 1998; Böker et al., 2002). Their study became possible via high spatial resolution observations from HST in the 1990s. They have properties similar to those of globular clusters although they are more compact, more massive and on average 4 mag brighter than the old globular clusters of the Milky Way (Böker et al., 2004; Walcher et al., 2005). Many NSCs host an AGN (Seth et al., 2008) i.e. a supermassive black hole (SMBH) in their centers, have complex star formation histories (Rossa et al., 2006; Seth et al., 2006) and obey scaling-relations with host galaxy properties as do central SMBHs (Ferrarese et al., 2006; Wehner & Harris, 2006).

The formation scenarios of NSCs can be split into two main categories: The merger scenario where several dense globular clusters migrate close to the center from the outskirts via dynamical friction and merge to form a compact stellar system (Tremaine & Ostriker, 1975; Arca-Sedda

& Capuzzo-Dolcetta, 2014); and the 'in situ' episodic buildup scenario where stars form locally from infalling gas towards the center (Schinnerer et al., 2008).

The study of NSCs is of great interest because several of the most extreme physical phenomena occur within them such as SMBHs, active galactic nuclei, star-bursts and extreme stellar densities. The Galactic NSC is particularly interesting because of its proximity. At a distance of about 8kpc from Earth it is the only NSC in which individual stars can be resolved.

The center of the galactic NSC harbors a SMBH (Genzel et al., 2010; Ghez et al., 2008). Joint statistical analysis based on orbits around Sgr A* (Gillessen et al., 2009), star counts and kinematic data gives $M_{\bullet} = (4.23 \pm 0.14) \times 10^6 M_{\odot}$ and a statistical parallax $R_0 = 8.33 \pm 0.11$ kpc (Chatzopoulos et al., 2015). Recent studies (Schödel et al., 2014; Chatzopoulos et al., 2015) have revealed that the NSC is flattened with an axial ratio $q \approx 0.73$, which is consistent with the kinematic data (Chatzopoulos et al., 2015). One unsolved problem of the NSC is the absence of a stellar cusp near the center. If the nucleus containing the black hole is sufficiently old, a stellar cusp will form eventually (Bahcall & Wolf, 1976; Preto & Amaro Seoane, 2010). For the NSC we instead observe an almost flat core (Burkert, 2009; Bartko et al., 2010).

Observations of the NSC in Optical-UV wavelengths are impossible because of the high extinction $A_V \geq 30$ mag due to interstellar dust (Scoville et al., 2003; Fritz et al., 2011). Therefore we rely on the infrared, with average K-band extinction toward the central parsec close to $A_K \approx 3$ (Rieke et al., 1988; Schödel et al., 2010; Fritz et al., 2011) which is mostly foreground extinction. However it is very difficult observationally to measure the extinction variation along the line-of-sight within the NSC.

The area around Sgr A* contains ionized gas which can be well described by a system of ionized streamers or filaments orbiting Sgr A* (Ekers et al., 1983; Serabyn & Lacy, 1985) that is presumably associated with some dust as well. This complex structure of ionized gas is called the 'mini-spiral' and consists of four main components: the northern arm, the eastern arm, the western arm and the bar (Zhao et al., 2009) surrounded by the circumnuclear disk of radius ~ 1.6 pc (Christopher et al., 2005; Jackson et al., 1993).

In our previous dynamical study of the NSC, an asymmetry in the v_l -proper motions was observed in the histograms which was attributed to dust causing stars on the far side of the NSC to fall out of the sample. The aim of this paper is to present estimates for the extinction within the NSC based on our dynamical model and see to what extent this is correlated with the mini-spiral, to try to understand the slight asymmetry in the v_l velocity histograms of the NSC and to check the impact of this on the fundamental parameters derived from the dynamical model such as the mass and the distance.

In section 2 we discuss briefly our current best dynamical model of the NSC and describe qualitatively the effects of dust on the dynamics of the NSC. In section 3 we show evidence based on dynamics for the presence of dust within the NSC. In section 4 we develop a method for making an analytical model for the dust extinction that can be used on top of an existing dynamical model. Finally in section 5 we present extinction values for the dust within the NSC based on the prediction of the model in conjunction with the mini-spiral observations.

Dust no-rotation

0	0
0	0

Dust with rotation

+	+
+	+

Inclination

+	+
-	-

Triaxiality (expected)

-	+
-	+

Figure 3.1: Each small square represents a quadrant in the (l, b) coordinate system, a + signifies an asymmetry in the v_l VHS (e.g. right peak higher) a - the opposite asymmetry and 0 no asymmetry at all. We notice that dust produces the same asymmetry in every quadrant.

3.2 Effects of dust on the apparent dynamics of the NSC

In this section we give a brief description of the current best dynamical model of the NSC based on Chatzopoulos et al. (2015) and we show initial evidence for dust extinction within the NSC.

3.2.1 Axisymmetric dynamical model of the NSC

For this work we use proper motions from ~ 7100 stars obtained from AO assisted images and photometry data based on Fritz et al. (2014). The proper motion data are given in Galactic longitude l^* and Galactic latitude b^* angles centered on Sgr A*. In the following we always refer to the shifted coordinates but will omit the asterisks for simplicity. We assume that the rotation axis of the NSC is aligned with the rotation axis of the Milky Way disk. This is in accordance with the very symmetric Spitzer surface density distribution of Schödel et al. (2014).

In Chatzopoulos et al. (2015) we used a two-component spheroidal γ -model (Dehnen, 1993; Tremaine et al., 1994) which we fitted to the density data in the l and b directions provided by Fritz et al. (2014). The inner rounder component can be considered as the NSC and the outer, more flattened as the inner part of the nuclear stellar disk. Using the density we applied axisymmetric Jeans modeling in order to constrain the stellar mass M_* , the black hole mass M_\bullet , and the distance R_0 of the NSC which we found to be

$$\begin{aligned} M_*(r < 100'') &= (8.94 \pm 0.31|_{\text{stat}} \pm 0.9|_{\text{syst}}) \times 10^6 M_\odot \\ M_\bullet &= (3.86 \pm 0.14|_{\text{stat}} \pm 0.4|_{\text{syst}}) \times 10^6 M_\odot \\ R_0 &= 8.27 \pm 0.09|_{\text{stat}} \pm 0.1|_{\text{syst}} \text{kpc} \end{aligned} \quad (3.1)$$

for the NSC only, not including the constraints from stellar orbits around Sgr A*.

Having this information we used the Qian et al. (1995) algorithm to calculate the even part of the 2-Integral distribution function (DF) $f(E, L_z)$. This allowed us to calculate the velocity profiles (VP) of the model. We found that the even part of the DF can predict very well the characteristic 2-peak shape (Schödel et al., 2009; Fritz et al., 2014) of the velocity histograms (VH) for the v_l proper motion velocities. The addition of a suitable odd part in L_z to the even part of the DF represents the rotation of the cluster.

3.2.2 Asymmetry of the v_l proper motion histograms

Upon a closer look at the velocity histograms in l direction (VH $_l$) it is noticeable that the right peak is slightly higher than the left (e.g. Fig.3.2, the smooth blue line is a homogeneous dust model see Section 5). This means that seemingly there are more stars in the front of the cluster (positive velocities) than in the back.

At least three effects could produce such an asymmetry. Figure 3.1 illustrates the effect of dust extinction without rotation, dust extinction with rotation, inclination and triaxiality on the VHs. Each small square represents a quadrant of the shifted Galactic coordinate system (l, b) where Sgr A* is at the center. A + signifies an asymmetry (e.g. right peak higher) a - the opposite asymmetry and 0 no asymmetry at all (both peaks same height). We will see in the following Sections that dust with rotation produces the same asymmetry in every quadrant.

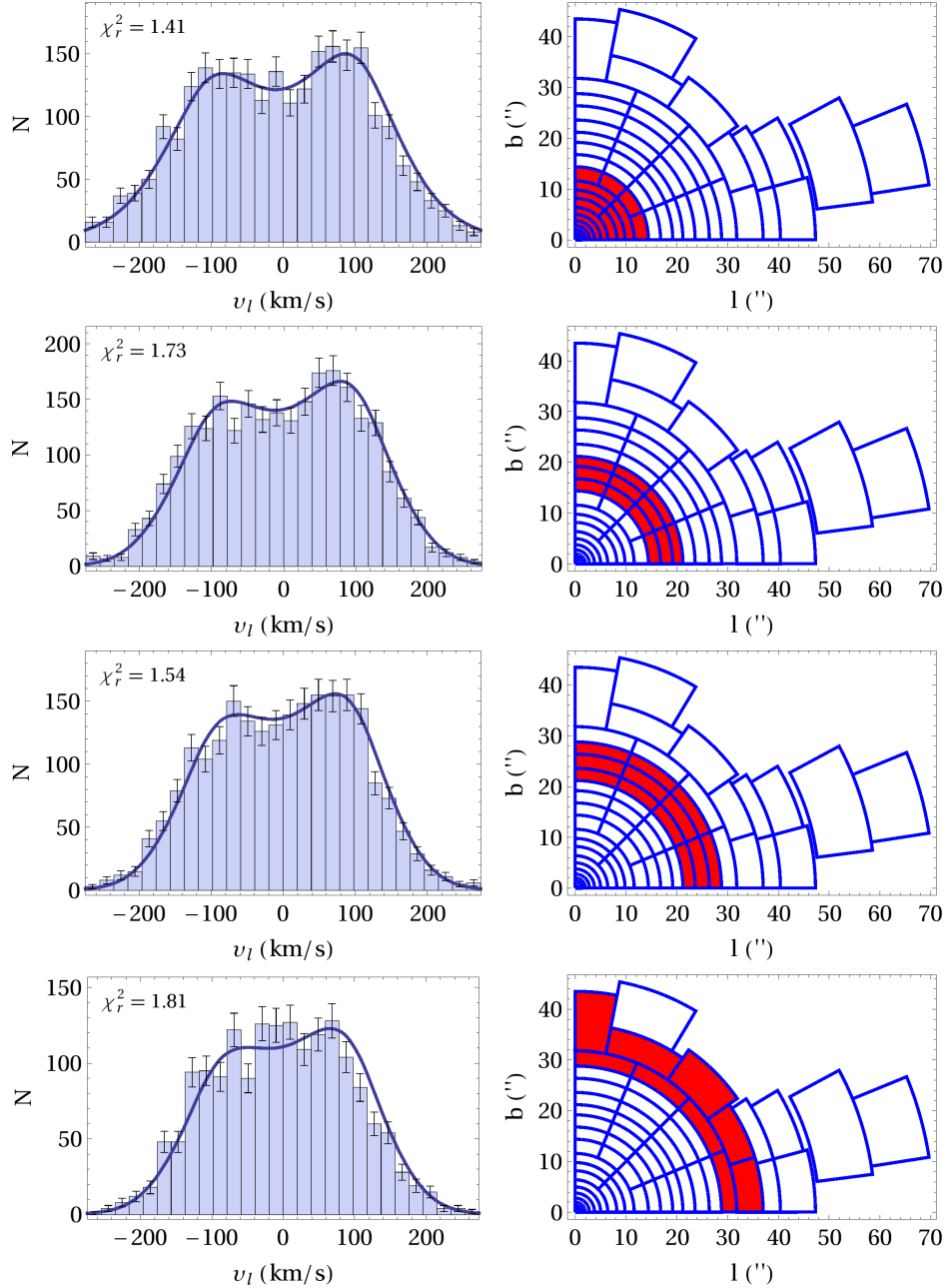


Figure 3.2: VH data and VPs in the l direction predicted by the axisymmetric model and dust model. The cells are from Chatzopoulos et al. (2015). Each star is mapped to the first quadrant using $(l, b) \rightarrow (|l|, |b|)$. The blue smooth lines correspond to our best model of the NSC (based on Chatzopoulos et al. (2015)) plus a homogeneous dust model with $A_K = 0.4$ that extends from $-200''$ to $+200''$ along the line-of-sight.

Because of the dust fewer stars will be visible at the back of the cluster, and because of the rotation the missing stars will be stars with negative velocities. Inclination of the NSC produces the opposite result for upper and lower quadrants because when the line-of-sight does not pass exactly through the center, it passes through areas of unequal density in front of and behind the NSC. On the other hand, triaxiality produces the opposite result for the right and left quadrants because of the geometry of the streamlines of the triaxial system. This plot shows that if we symmetrize the data to one quadrant only, the effect of the dust will remain while the effects of the inclination and triaxiality will cancel out. This is what we observe on the symmetrized data of the NSC (Fig. 3.2). Therefore we conclude that the observed asymmetry cannot be a result of inclination and triaxiality but might be a result of dust. This suggests that dust extinction in conjunction with rotation may produce the observed asymmetry. We note here that in order to observe this asymmetry (right peak higher than left) in the velocity profile in the l direction (VP_l), the dust should be *inside* the cluster (i.e. within a few parsecs of the Galactic center) where the density is maximum, otherwise only a change in scale of the VPs would take place.

3.3 Differential extinction in the NSC

We use photometry data in the H and K bands for 7101 stars. We split the data into a central and an extended field. The central field is a square centered on Sgr A* with size of $40''$ and contains 5847 stars. The rest of the stars belong to the extended fields, as shown in Fig. 3.3.

3.3.1 Total extinction

We obtain the extinction towards each star from the $H - K$ color (stars without H photometry and late-type stars are excluded). We obtain intrinsic color estimates by assuming that the stars are at the distance of the Galactic Center and that they are giants, as it is the case for most stars in the Galactic Center (Pfuhl et al., 2014). The intrinsic color varies between 0.065 and 0.34 but the majority of stars belong to a small magnitude range around the red clump. Therefore and also because the extinction is high, the influence of intrinsic color uncertainties on the extinction is small compared to other effects, like photometric uncertainties. We use the extinction law of Fritz et al. (2011), implying $A_K = 1.348E(H - K)$.

In this work we are mainly interested in the extinction variation A_K within the Galactic center. We obtain an estimate for that by measuring for each star the extinction relative to its neighbors, more specifically relative to the median extinction of its 15 closest neighbors. Obvious foreground stars were already excluded in Fritz et al. (2014). By using 15 neighbors we obtain a robust median extinction estimate that is much less affected by extinction variations in the plane of the sky. To further reduce the influence of this extinction variation we exclude stars with too few close neighbors.

Fig. 3.3 shows a map of extinction for the central and extended fields based on $H - K$ colors. The area within the white frame is the central field which is consistent with Fig. 6 of Schödel et al. (2010). Most of the extinction of typically $A_K = 3$ mag shown in this plot is foreground extinction but a fraction $\simeq 0.4$ mag or so is intrinsic to the NSC region as we show in the following. Fig. 3.4 shows a histogram of the extinction for the central field. The mean extinction inferred from this plot is $A_K = 2.94$ mag with standard deviation 0.24 mag.

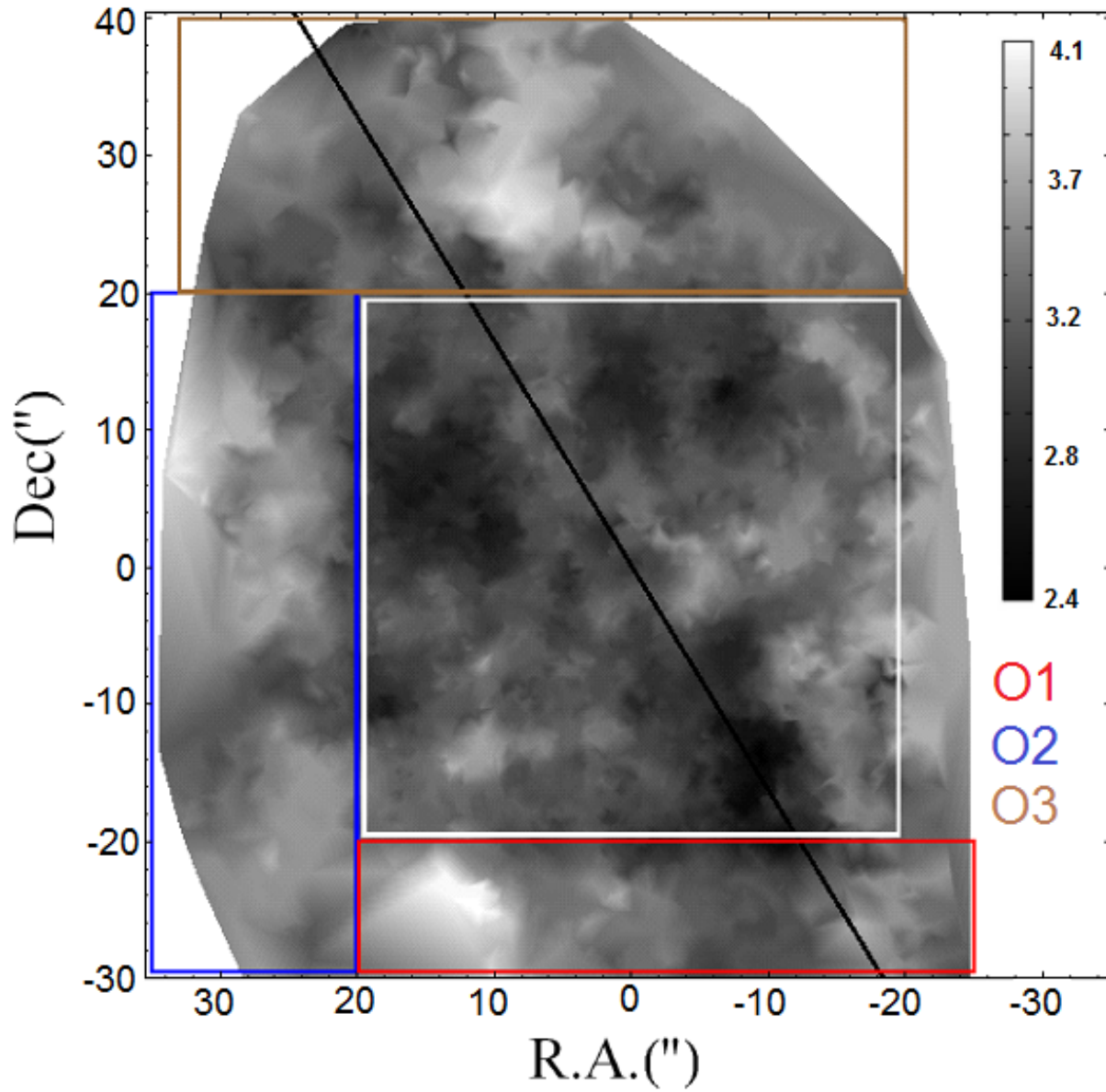


Figure 3.3: Map of A_K for the NSC derived from $H - K$ colors. The map is similar to that of Schödel et al. (2010). The Galactic plane is shown as a black line. The central field is shown in white and the outer fields O1-O3 in red, blue and brown.

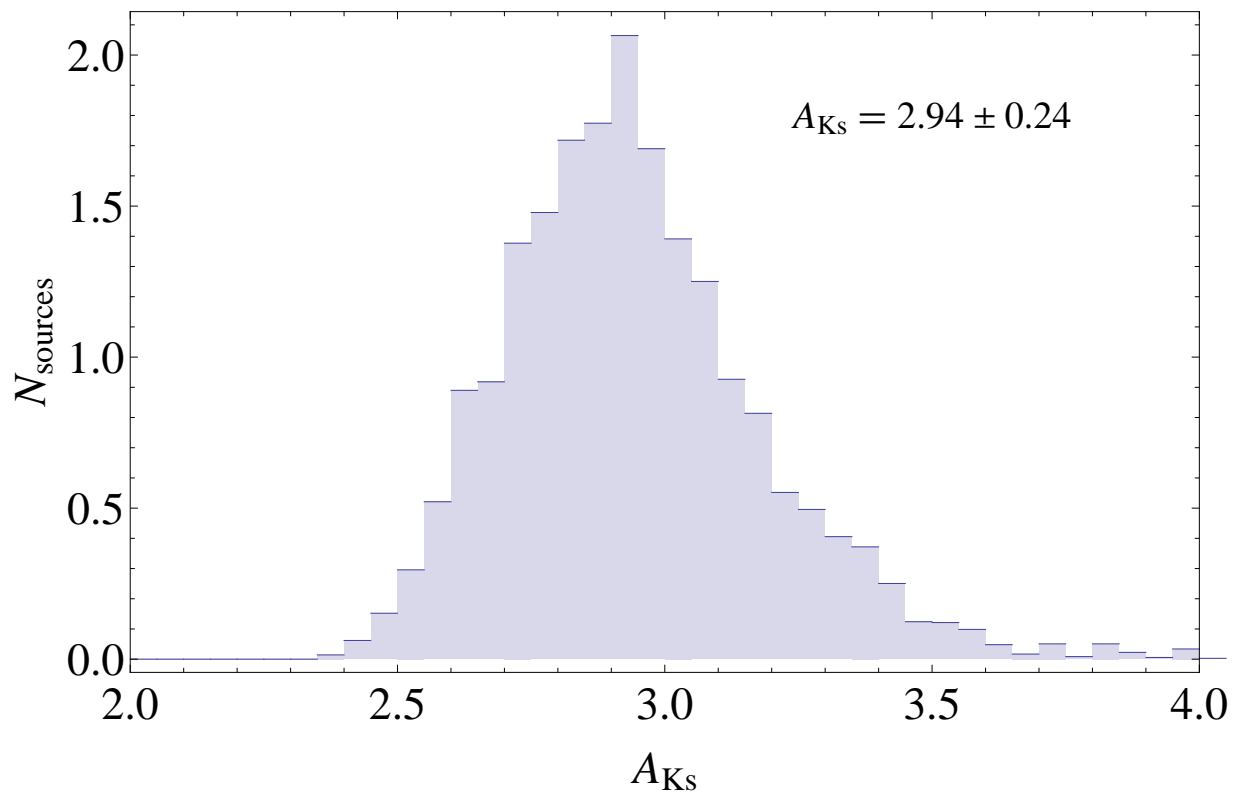


Figure 3.4: Histogram of the extinction A_K based on $H - K$ colors for all the stars. Mean extinction and standard deviation also given. Stars with small A_K are excluded because they are foreground stars (Fritz et al., 2014).

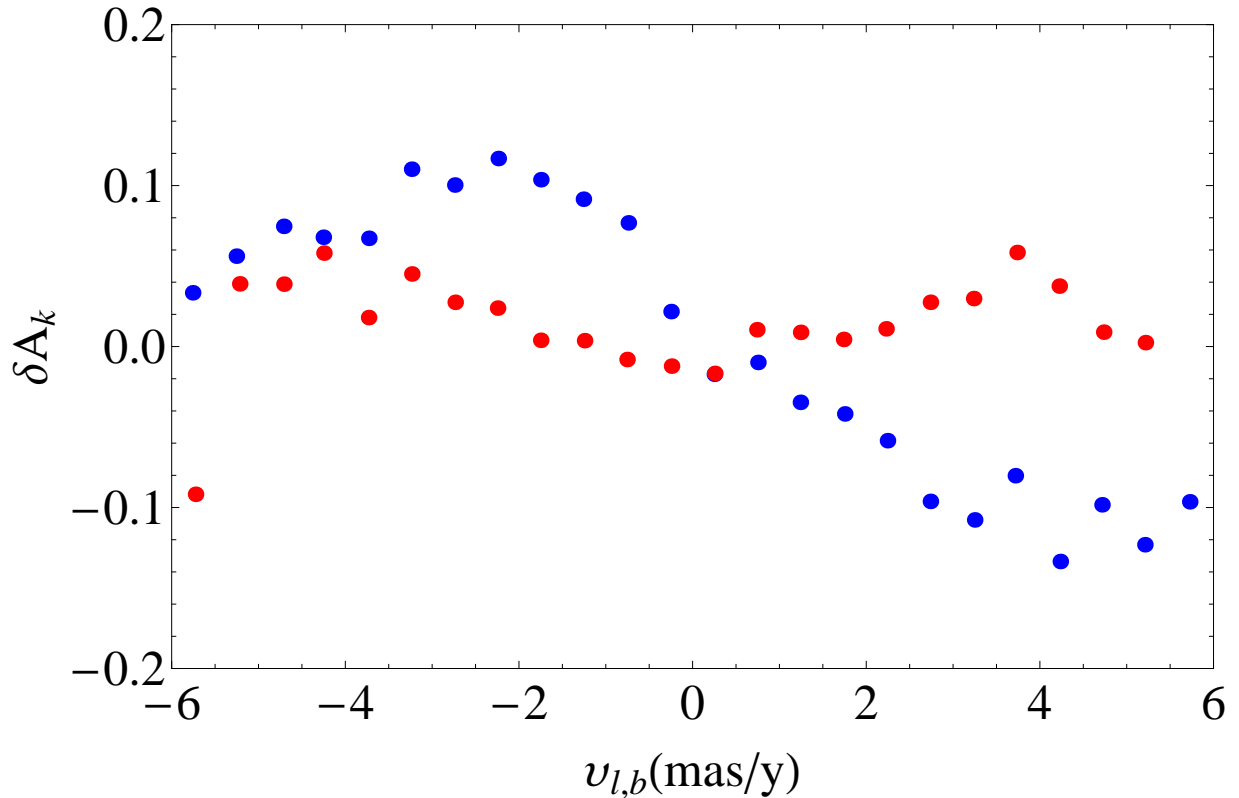


Figure 3.5: Average differential extinction of nuclear cluster stars plotted as a function of v_l (blue) and v_b (red) proper motion. The differential extinction is inferred from the difference in the color of a star to the median of its 15 nearest neighbors using the extinction law of Fritz et al. (2011) and correcting also for the weak color variation with magnitude.

3.3.2 Extinction in the NSC region

The average differential extinction of stars as a function of v_l and v_b velocities is an important photometric quantity that can also be modeled and gives us information about the dust within the NSC. Fig. 3.5 shows this for the central field. We notice that the average differential extinction for the v_l is negative for positive velocities (preferentially at the front of the cluster) and positive for negative velocities (back of the cluster) i.e., stars at the front of the cluster are observed with less extinction than their neighbors. This finding is consistent with the asymmetry of the VHS in l direction (Fig. 3.2) and implies $A_K \simeq 0.4$ within the NSC, see below. In contrast the average differential extinction for v_b is relatively flat and consistent with the symmetric bell shape of the VH in b direction. However we still notice a scatter of the points which is indicative of the systematic variations we should expect in A_K .

Fig. 3.6 shows the extinction distribution from the observed ratio of Pa α to H92 α radio recombination-line emission (Roberts & Goss, 1993) for the central field, from Scoville et al.

(2003). The coloring signifies total extinction and the contours show the outline of the mini-spiral. The fact that the outline of the mini-spiral can be seen also in the dust suggests that a fraction of the extinction is likely to be associated with the mini-spiral and therefore is located within the NSC. The dust associated with the nuclear spiral is likely to be concentrated in a small distance interval along the line-of-sight of order a fraction of the radius in the sky.

3.4 Dust modeling

We saw in the previous section that the observed asymmetry of the VH_l is likely to be associated with dust extinction. In this section we describe how one can make an analytical dust extinction model and use it with an already existing model of the NSC similar to that of section 2.

For the rest of this work, along with l and b we use a Cartesian coordinate system (x, y, z) where z is parallel to the axis of rotation as before, y is along the line of sight (smaller values closer to the earth) and x is along the direction of negative longitude, with the center of the NSC located at the origin.

First we need to model a luminosity function. We can do that by taking the product of two functions. The first represents a power law function in luminosity, corresponding to an exponential magnitude distribution, $L(m) = 10^{\gamma m}$. The second is an error function that represents the completeness function, so that:

$$\frac{dN}{dm} = L(m) \times C(m) = 10^{\gamma m} (1 - \text{erf}[(m - m_0)/\sigma])/2 \quad (3.2)$$

In the previous function γ is the power law index of the luminosity function and m_0 is the value where the completeness function $C(m)$ has its half height. For the power law we set the index to $\gamma = 0.27 \pm 0.02$ as in Schödel et al. (2010). For the completeness function we set $m_0 = 16.5$ and $\sigma = 1$ because we found that these values represent well the K luminosity data as shown in Figure 3.7. The red curve of Figure 3.7 shows equation 3.2 with the chosen values.

Next we need the extinction variation over the line-of-sight which is just the derivative of the extinction over the line-of-sight i.e. da_K/dy . The function da_K/dy is general and could for example be represented as a sum of Gaussians but for simplicity we choose a square function, so that:

$$\frac{da_K}{dy} = \begin{cases} 0, & y < y_1 \\ c, & y_1 \leq y \leq y_2 \\ 0, & y > y_2 \end{cases} \quad (3.3)$$

in which y_1 and y_2 indicate the positions where the dust starts and ends respectively. The integral of eq.3.3 over all line-of-sight is the maximum extinction A_K thus the constant c takes the value $c = A_K/\Delta y$ where $\Delta y = y_2 - y_1$. Function 3.3 integrates to:

$$a_K(y) = \begin{cases} 0, & y < y_1 \\ \frac{A_K}{\Delta y} (y - y_1), & y_1 \leq y \leq y_2 \\ A_K, & y > y_2 \end{cases} \quad (3.4)$$

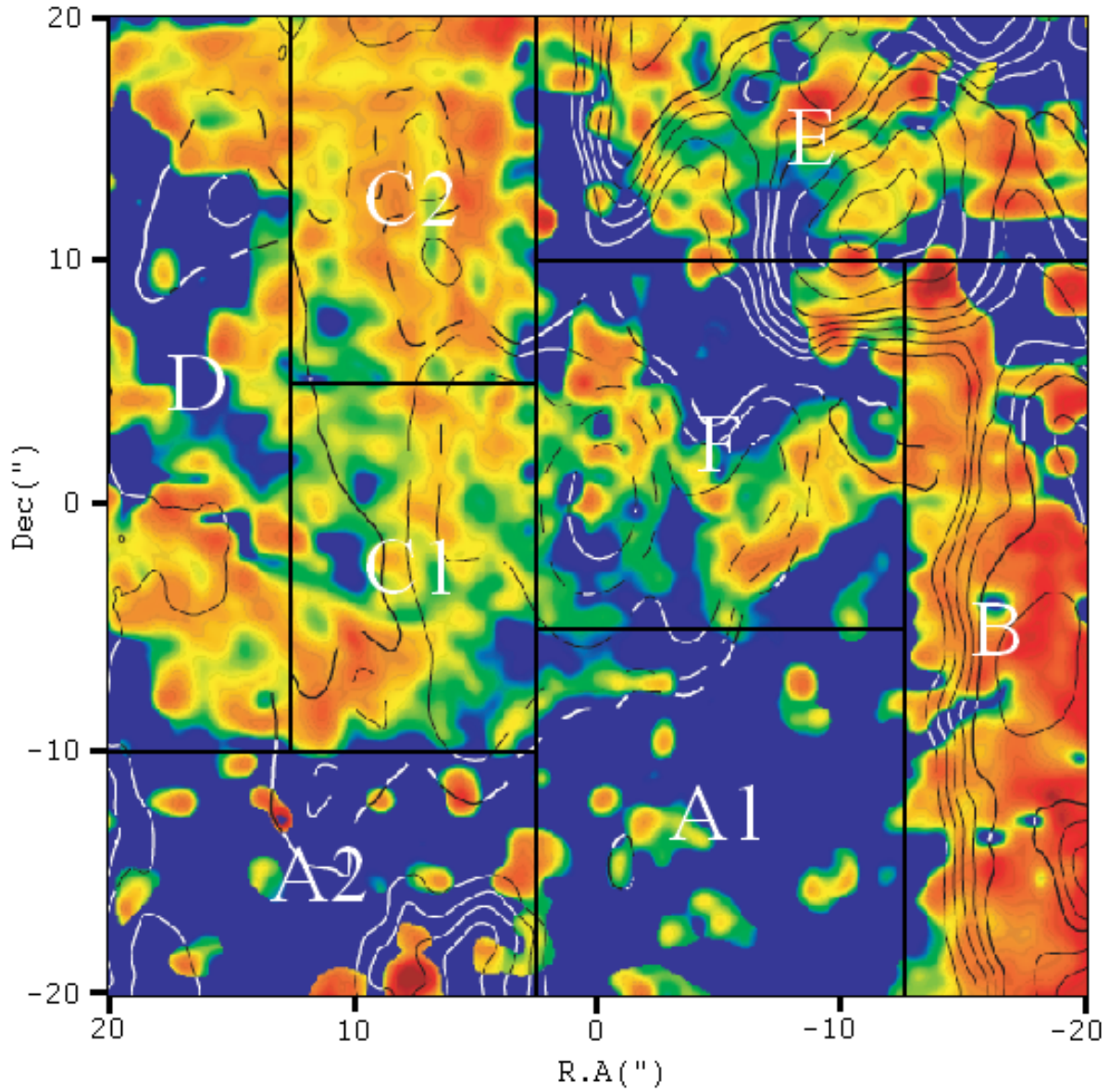


Figure 3.6: Extinction derived from the observed ratio of $\text{Pa}\alpha$ to $\text{H}92\alpha$ radio recombination-line emission (Roberts & Goss, 1993) for the central field from on Scoville et al. (2003). The field is split into eight cells, according to the outline of the mini-spiral, the shape of the VH in v_l and the δA_K curves.

The percentage reduction in observed stars as a function of line-of-sight distance is:

$$p(y) = \frac{\int L(m - a_K(y))C(m)dm}{\int L(m)C(m)dm} \quad (3.5)$$

With this we can calculate the percentage reduction in numbers of stars after the extinction with $p_{\max} = p(y_2)$. The percentage of stars hidden by extinction for $A_K = 0.4$ is about 25%. For the simple case where the luminosity function is a power law, the previous equation (3.5) takes the form $p(y) = L(-a_K(y))$. The function for $A_K = 0.4$ is shown in figure 3.8.

Having that we calculate the VP_l after the effect of dust with:

$$VPD(v_l; x, z) = \frac{1}{\Sigma} \iiint_{E>0} p(y) f_{tot}(E, L_z) dv_{los} dv_z dy. \quad (3.6)$$

Where in the previous function $f_{tot}(E, L_z) = f_e(E, L_z) + f_o(E, L_z)$ is the total DF consisting of an even part in L_z (contributes to the density) and an odd part (contributes to rotation) as in Chatzopoulos et al. (2015). Figure 3.9 shows a typical VP_l after adding dust with $A_K = 0.4$. We observe that the right peak of the VP_l is now higher than the left peak which is a combined effect of dust and rotation. The dust does not produce an asymmetry for the VP in b direction. One useful quantity is the average $A_K(v_l)$ over the line-of-sight. This can be calculated with:

$$\langle A_K(v_l) \rangle = \frac{\iiint a_K(y) p(y) f_{tot}(E, L_z) dv_z dv_{los} dy}{\Sigma \times VPD(v_l)} \quad (3.7)$$

Eq. 3.7 connects our model with the photometry. From this we calculate the average differential extinction variation along the line-of-sight which corresponds to the data of Fig. 3.5.

$$\delta A_K(v_l) = \langle A_K(v_l) \rangle - \frac{\int \langle A_K(v_l) \rangle VPD(v_l) dv_l}{\Sigma \int VPD(v_l) dv_l} \quad (3.8)$$

In order to understand the effects of dust extinction on $\delta A_K(v_l)$, we use two simple models for the dust distribution. The first is a homogeneous dust model that extends a few parsecs along the line-of-sight. The second is a thin $\sim 10''$ screen of dust placed in several positions along the line-of-sight. We have verified that the width of the screen is not a sensitive parameter and the results are almost unchanged if we set it for example to $\sim 5''$. Figures 3.9 and 3.10 shows these effects. In Fig. 3.9 we see the effect of three dust screen models and one homogeneous model on the VP_l for $A_K = 0.4$.

One important point to notice is that we can achieve the same effect (e.g. the same amount of asymmetry in the histograms) with several models by using different combinations of A_K and the distances at which the dust is placed along the line-of-sight, therefore the dust extinction model is degenerate. In Fig. 3.10 we see plots of several screen and homogeneous models based on eq. 3.8. The top panels show the $\delta A_K(v_l)$ curves of a screen dust model placed at several distances in front of (left) and at the back (right) of the cluster for $A_K = 0.4$. The first thing to notice is that the further the screen of dust is placed from the center the smaller is the effect of dust. This makes sense since far from the center the density of stars is lower. We also note that

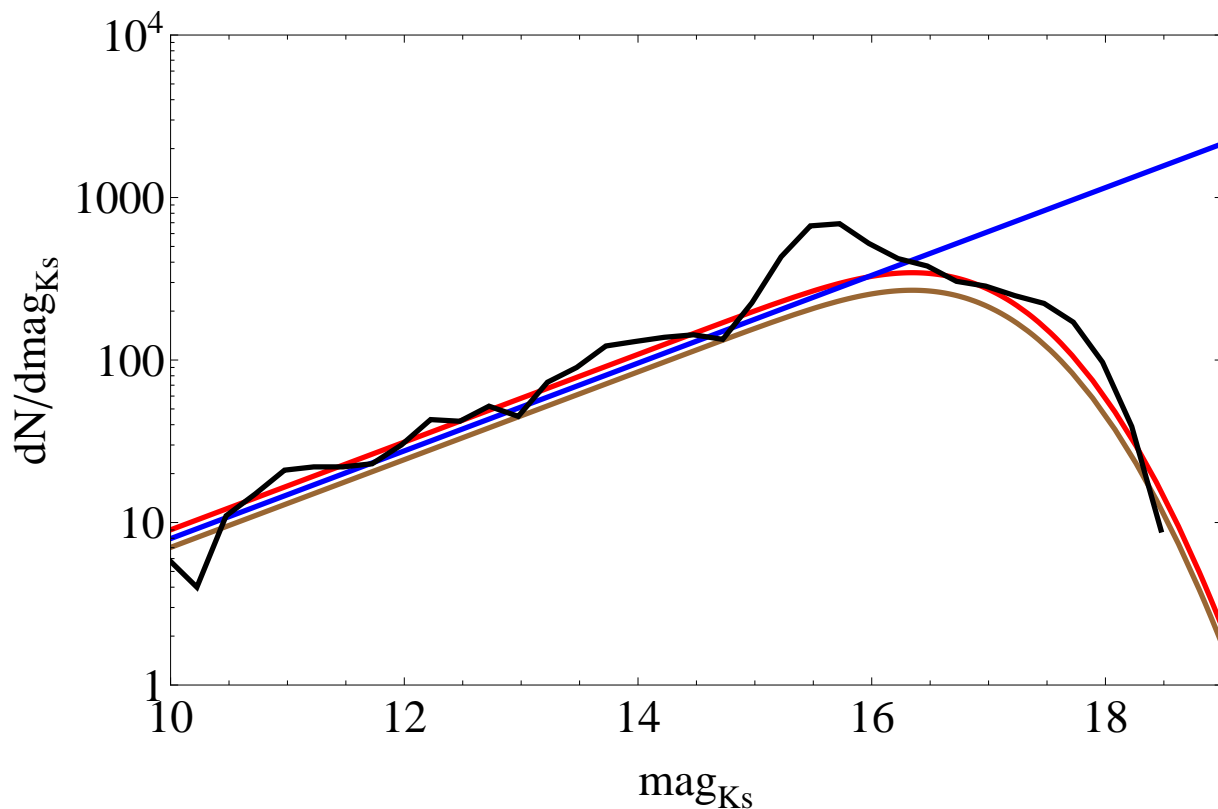


Figure 3.7: Modeled K luminosity with completeness function before (red) and after (brown) a dust effect with $A_K = 0.4$. The blue line is a power law fit to the stars $11 < K < 14$ with power-law index of 0.27 ± 0.02 as in Schödel et al. (2010). The black line is the K luminosity function for the Galactic center.

if the screen of dust is placed in front of the cluster, the curves are close to constant for the stars behind the cluster since there is no dust there to affect the $\delta A_K(v_l)$. The opposite happens when the screen of dust is behind the cluster. The bottom left panel shows the shape of $\delta A_K(v_l)$ for different A_K . The bottom right panel shows three homogeneous models that extend over different distance intervals along the line-of-sight. In this case the curves are symmetric relative to zero. The dust extinction model was implemented with Wolfram Mathematica.

3.5 Predictions of the Dust model

In the last section we described how one can include the effects of dust extinction in the dynamical modeling of the NSC, and calculate differential reddening signatures for the NSC stars. Here we proceed to model predictions and compare with both photometric and kinematic evidence. We will see that the asymmetries seen in the VPs for v_l can be explained as due to dust within the

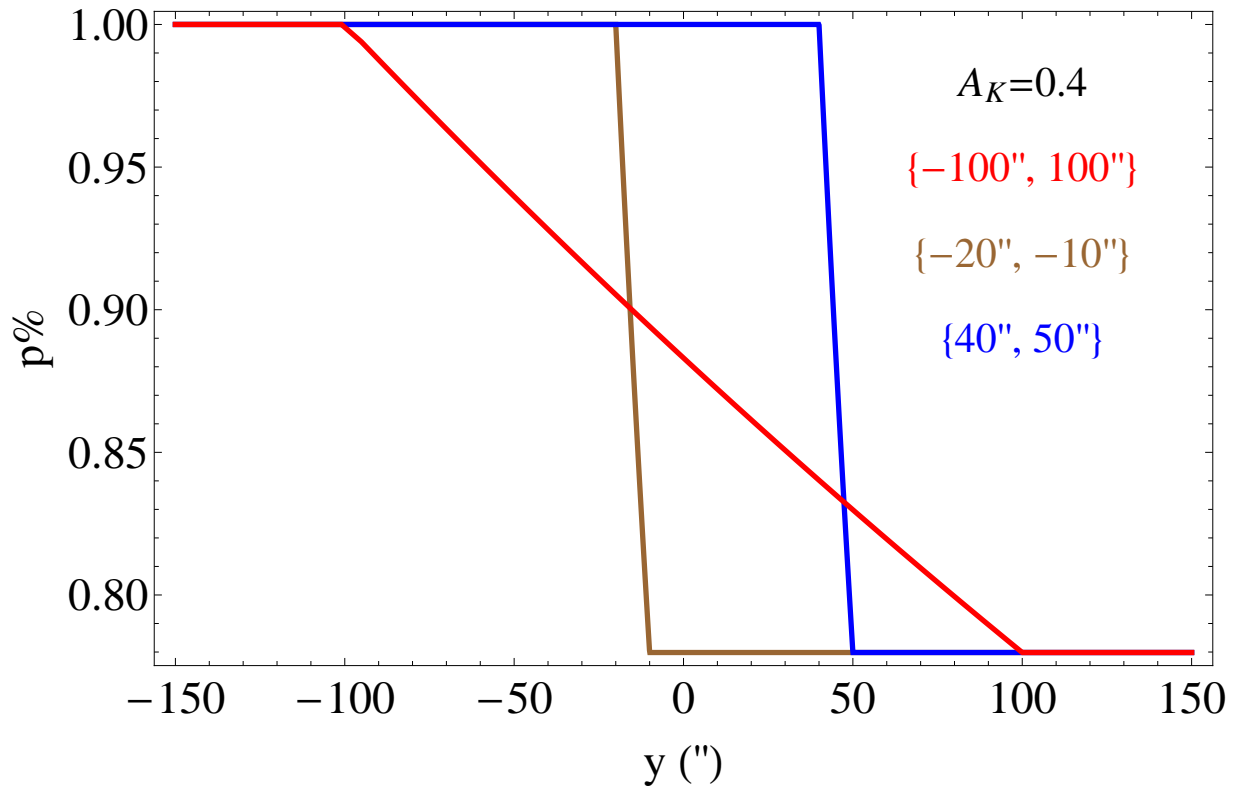


Figure 3.8: Percentage reduction in observable stars after a dust effect with $A_K = 0.4$, as a function of line-of-sight for a homogeneous dust model (red) and two dust screen models (brown, blue). About 75% of stars remain in the observed luminosity function after the extinction due to dust.

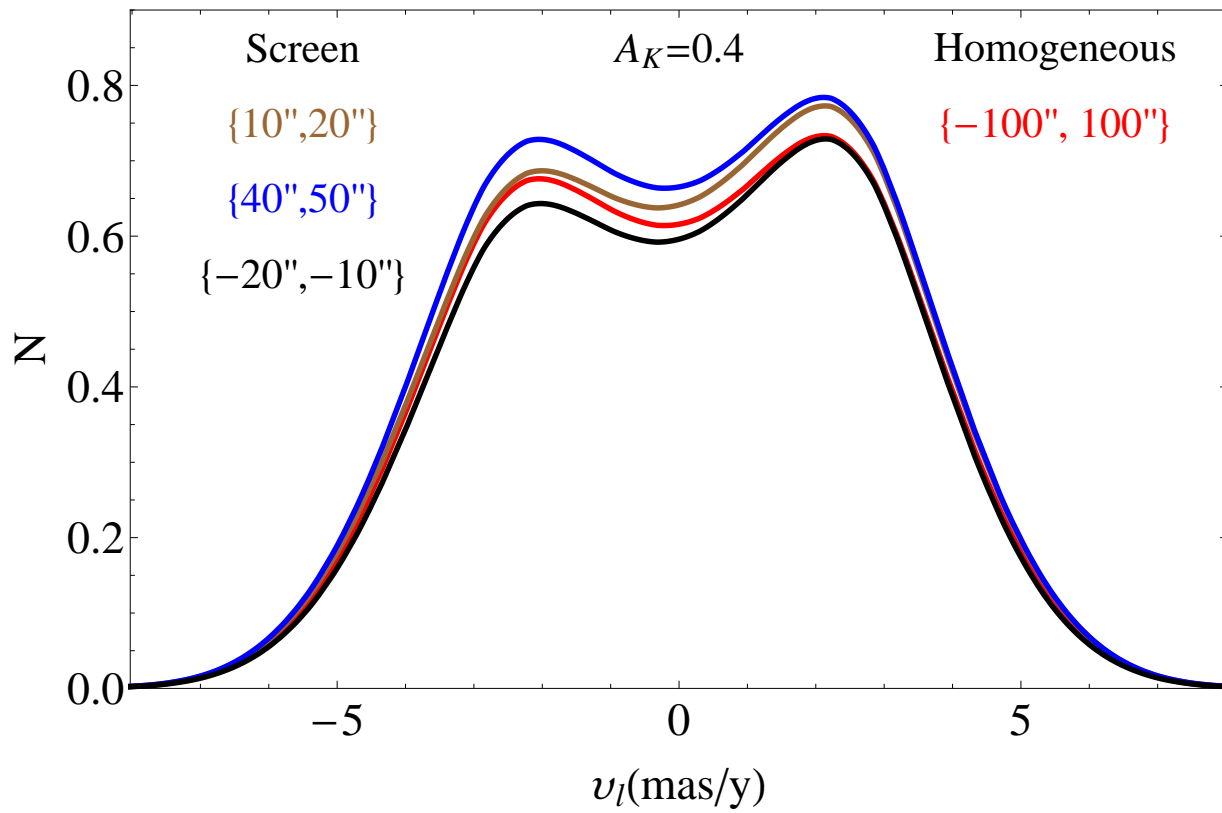


Figure 3.9: VPs in l direction for different models. The right peak is higher due to the combined effects of dust extinction and rotation. We can achieve the same effect (e.g. the same of asymmetry) for several combinations of A_K s and the distances where the dust is placed along the line-of-sight.

NSC. Our goal is to see whether dust in the Galactic Center mini-spiral can explain our data, and also to provide a rough extinction map of the central field based on the model and the available data.

Figure 6 shows the extinction derived from the observed ratio of Pa α to H92 α radio recombination-line emission (Roberts & Goss, 1993) from Figure 5 of Scoville et al. (2003). This extinction map for the central $40'' \times 40''$ around Sgr A* includes both foreground and NSC extinction. It is limited by the signal-to-noise ratio (S/N) of the H92 α recombination line flux, and the regions in which the extinction has an apparent value of $A_V = 15$ is where the S/N is not sufficient to derive the extinction. However, these data show a better representation of the mini-spiral than the extinction map derived from the observed ratio of Pa α to 6 cm radio continuum emission (Scoville et al., 2003).

Fig. 3.6 is split into eight cells and sub-cells. The reasoning behind the choice of these cells is based on the outline of the mini-spiral, the statistics and shape of the velocity histograms in v_l and the mean differential extinction variation δA_K along line-of-sight. The VH_l s for all cells and the δA_K as a function of v_l and v_b are shown in Fig. 3.11 for the following cells:

- Cell A1: This cell's small δA_K values are consistent with the lack of features in the extinction map in comparison with other cells. Also the δA_K values are consistent with the VH_l since both peaks look symmetric which is a sign of lack (or small amount) of dust within the NSC.
- Cell A2: The cell lacks strong mini-spiral features as cell A1. However both the VH_l and δA_K values show relatively strong effects of dust therefore this cell is separated from cell A1.
- Cell B: The δA_K values and the VH_l are consistent with the strong features of the mini-spiral in the extinction map since the δA_K points are higher and lower for negative and positive velocities respectively than the other cells and the asymmetry of the VH_l is intense. We also note that the dust effects are similar within the whole area B because after splitting it into 2 sub-areas (not shown) we observed the same signature.
- Cells C1 & C2: The cells C1 and C2 belong to the Northern Arm of the mini-spiral. The shape of the δA_K data for both cells seems similar for negative velocities but the δA_K for C2 is more symmetric and consistent with the extinction map hence we split the area into 2 halves. We notice also some asymmetry on the VH_l s of both areas C1 and C2.
- Cells D: Cell D was separated from C1 & C2 because the δA_K values look more symmetric than C1 & C2. We also note that the dust effects are similar within the whole area D because after splitting it into 2 sub-areas (not shown) we observed the same signature.
- Cells E & F: The δA_K values of these two cells look similar but the VH_l of the cell F lacks the asymmetry characteristic in contrast of cell E therefore we keep them separate.

The central field with these eight cells is surrounded by a a more extended area with observations for about 2000 stars. We split this area into three outer fields O1-O3 placed around the central field as shown in Fig. 3.3. The VH_l for these cells and the δA_K as a function of v_l are shown in Fig. 3.12.

Our goal is to give a model prediction of each of these cells (8+3 in total). For the model we use a thin screen of dust with width $10''$ because the dust associated with the nuclear spiral is likely to be concentrated in a small distance interval along the line-of-sight. The precise width of the dust screen is not important as the dust signatures are insensitive to this parameter. The two main parameters are the total extinction in the screen and its location along the line-of-sight. However, as explained in the last section, these two parameters are partially degenerate. The degeneracy is particularly strong for the VH_l histograms. The δA_K data in principle are sensitive to whether the extinction is in front or behind the Galactic center, as shown in Fig. 3.10. However, the A_K data have large scatter between adjacent data points such that points with seemingly small error bars can even have the ‘wrong’ sign of δA_K (Fig. 3.11). This large scatter is also seen in the δA_K versus v_b plots (also shown in Fig. 3.11) where no dust signature is present. Therefore we decided to not try to fit the data using χ^2 .

Rather, we choose to place the dust screens along the line-of-sight according to other available information, and only deviate from this when this appears inconsistent with the shape of the δA_K distribution. The total dust extinction of the dust screen is then chosen by eye mostly from the amplitude and shape of the δA_K distribution, taking into account also the scatter of the δA_K points, and to a lesser degree from the asymmetry of the VH_l peaks.

Specifically for the central field we use the three orbit-model of Zhao et al. (2009) for the three ionized gas structures in the central 3pc (the Northern Arm, Eastern Arm, and Western Arc). We then map the center of each of the cells to a point in the relevant orbit plane according to its R.A and Dec. position. The distance from the center along the line-of-sight is given from the coordinates of that point on the orbit plane. For each cell, we use one common mean distance. Table 3.1 shows to which orbital plane each cell is assigned, and the distance of the dust screen from Sgr A*.

Fig. 3.11 shows the predictions of the screen dust model for the 8 cells of the central field. The reasoning behind the choice of A_K and positions for the dust screen is based on the shape of data and the several examples of Fig. 3.10:

- Cell A1 & B: We place the dust screen in front of the cluster according to the value of Table 3.1. These two cells are interesting because they both show a correlation between the outline of the mini-spiral and the photometry data. They also exhibit the maximum contrast between the amount of dust. Cell B needs ~ 5 times more extinction than cell A.
- Cell A2: The dust screen is placed behind the center according to Table 3.1.
- Cell C1 & D: The shape of the data in conjunction with top right panel of Fig. 3.10 indicate that the dust screen should be behind of the cluster (also gives a much better χ^2) in contrast with the value of Table 3.1. The reason for this is probably because the single orbit description is not accurate for the centers of these cells.
- Cell C2 & E: For both cells the dust screen is placed in front of the cluster according to values of Table 3.1.
- Cell F: The shape of the data in conjunction with lower right panel of Fig. 3.10 indicate that the dust screen should be centered.

For the outer cells of the extended field the A_K is selected according to the general characteristics of plot 3.10:

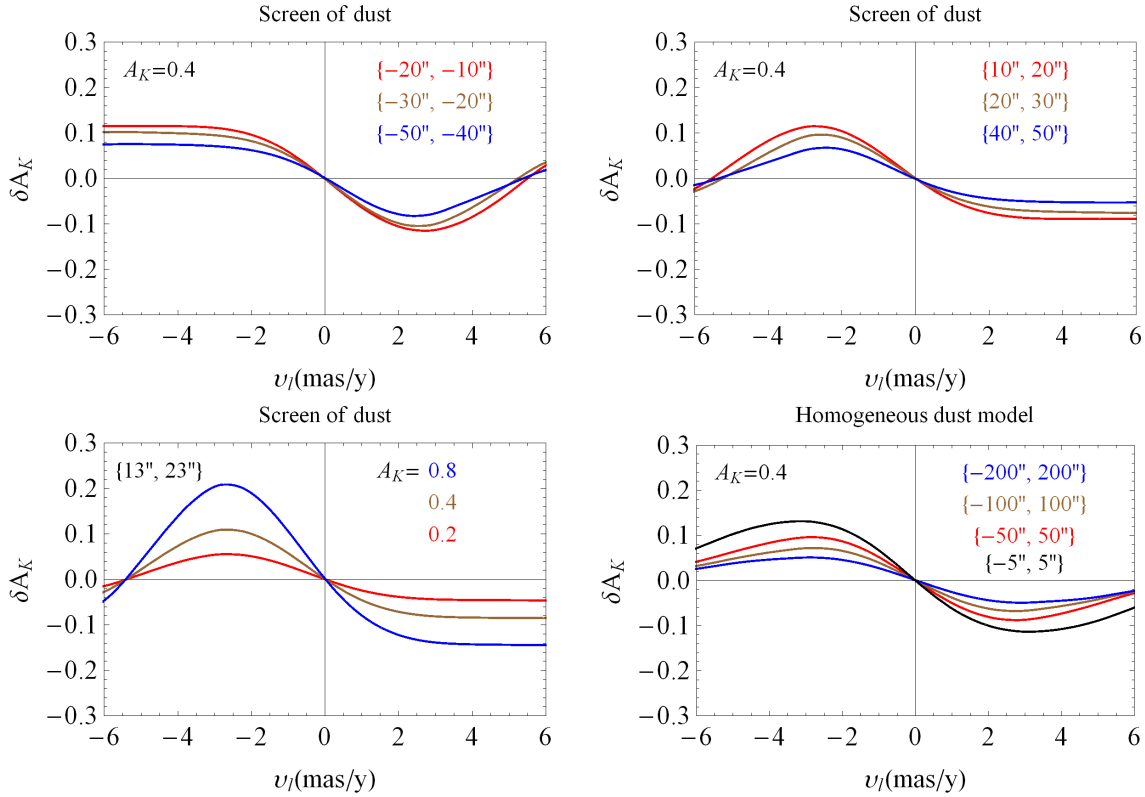


Figure 3.10: Shape of δA_K versus v_l curve for several dust models. Top left: Dust screen models placed in front of the cluster for constant $A_K = 0.4$. The numbers in the parenthesis show where the dust screen starts and ends respectively along the line-of-sight. Top right: Dust screen models placed behind the cluster for constant $A_K = 0.4$. Bottom left: Dust screen models placed slightly behind the cluster for several A_K values. Bottom right: Homogeneous dust models that extend in several distances along the line-of-sight for constant A_K . The line-of-sight for all curves has coordinates $l = 10''$ and $b = 10''$.

Northern Arm	E (-15")			
Eastern Arm	A2 (5")	C1 (-9")	C2 (-25")	D (-20")
Western Arc	B (-25")	A1 (-10")	F (-5")	

Table 3.1: Each one of the eight cells of Fig. 3.10 belongs to an orbital plane (Zhao et al., 2009) representing one of the three ionized gas (Northern Arm, Eastern Arm, and Western Arc) formations. The inferred line-of-sight distance of the dust screen from Sgr A* is given in the parentheses (negative points towards the earth).

Cell	A1	A2	B	C1	C2	D	E	F
Total extinction	2.73	2.99	3.1	2.82	2.87	2.78	2.84	2.95
Foreground extinction	2.66	2.79	2.7	2.67	2.72	2.61	2.69	2.8

Table 3.2: Extinction values per cell based on Fig. 3.3. The foreground extinction of each cell is estimated according to $A_K(\text{total}) = A_K(\text{foreground}) + x * A_K(\text{NSC})$ where we set $x = 0.5$.

- Cell O1 & O3: Both the VHS and the photometry have a consistent signature. For both cells the extinction is close to $A_K \simeq 0.35$ mag.
- Cell O2: For this cell we note that the photometry is as expected but the peaks of the VH are almost even.

Having the prediction for the cells we can estimate the foreground extinction for each cell using the A_K values of Fig. 3.3. The second row of table 3.2 shows the total extinction of each cell of the central field based on Fig. 3.3. The third row shows an estimate of the foreground extinction based on the $A_K(\text{total}) = A_K(\text{foreground}) + x * A_K(\text{NSC})$ where we set $x = 0.5$.

3.6 Does the addition of dust affect the measured M_{\bullet} , M_* and R_0 ?

In this section we try to answer how much the dust *within* the NSC will affect the derived (Chatzopoulos et al., 2015) statistical parallax, supermassive black hole and stellar mass of the NSC. The *foreground* dust will affect the VPs only by a scale factor which does not impact the derived values. In Chatzopoulos et al. (2015) we derived new constraints on the R_0 , M_* and M_{\bullet} by fitting to the corresponding data the $\langle v^2 \rangle_{l,b,los}^{1/2}$ part of the 2nd order Jeans moments, that are moments of the even part of the corresponding VPs of the 2-Integral distribution function. Therefore here the problem is reduced to how much the even part in L_z of the VPs changes after the addition of dust within the NSC.

Figure 3.13 shows the even parts of the VPs for v_l , v_b and v_{los} for a NSC dynamical model with no dust (best model from Chatzopoulos et al. (2015)) and a dynamical model that includes the screen dust prediction for a line-of-sight through cell B which has the largest amount of extinction ($A_K = 0.8$) among the cells of the central and outer fields. We notice that the difference between

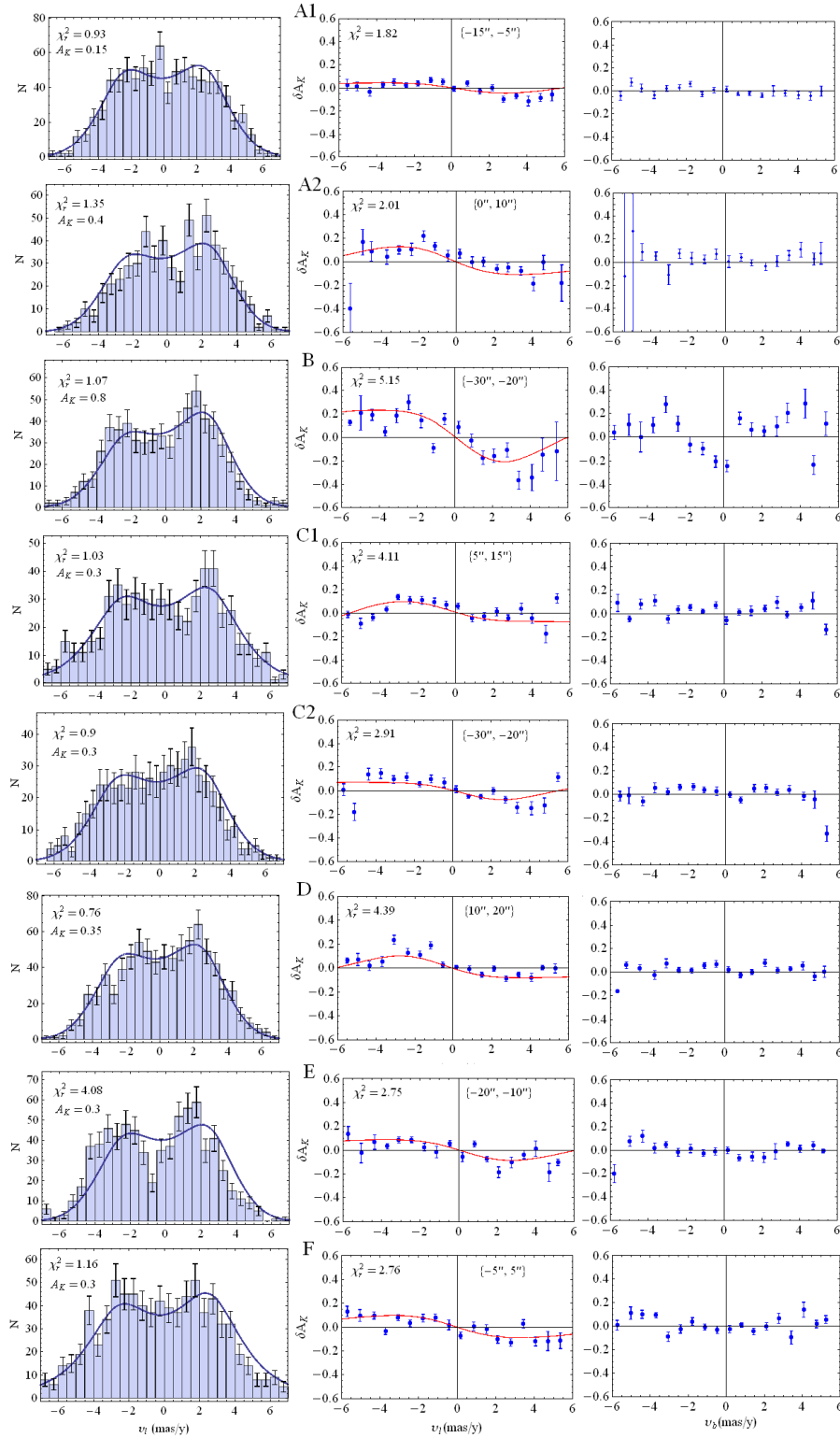


Figure 3.11: Predictions of the model with the VH and δA_K data for each cell. The numbers in the brackets show where the screen of dust is placed relative to the center. Reduced χ^2 are also provided for the histograms and the photometry. For the cells A1, A2, B, C2, E, the screen dust distance is based on the orbit models of the mini-spiral (Zhao et al., 2009).

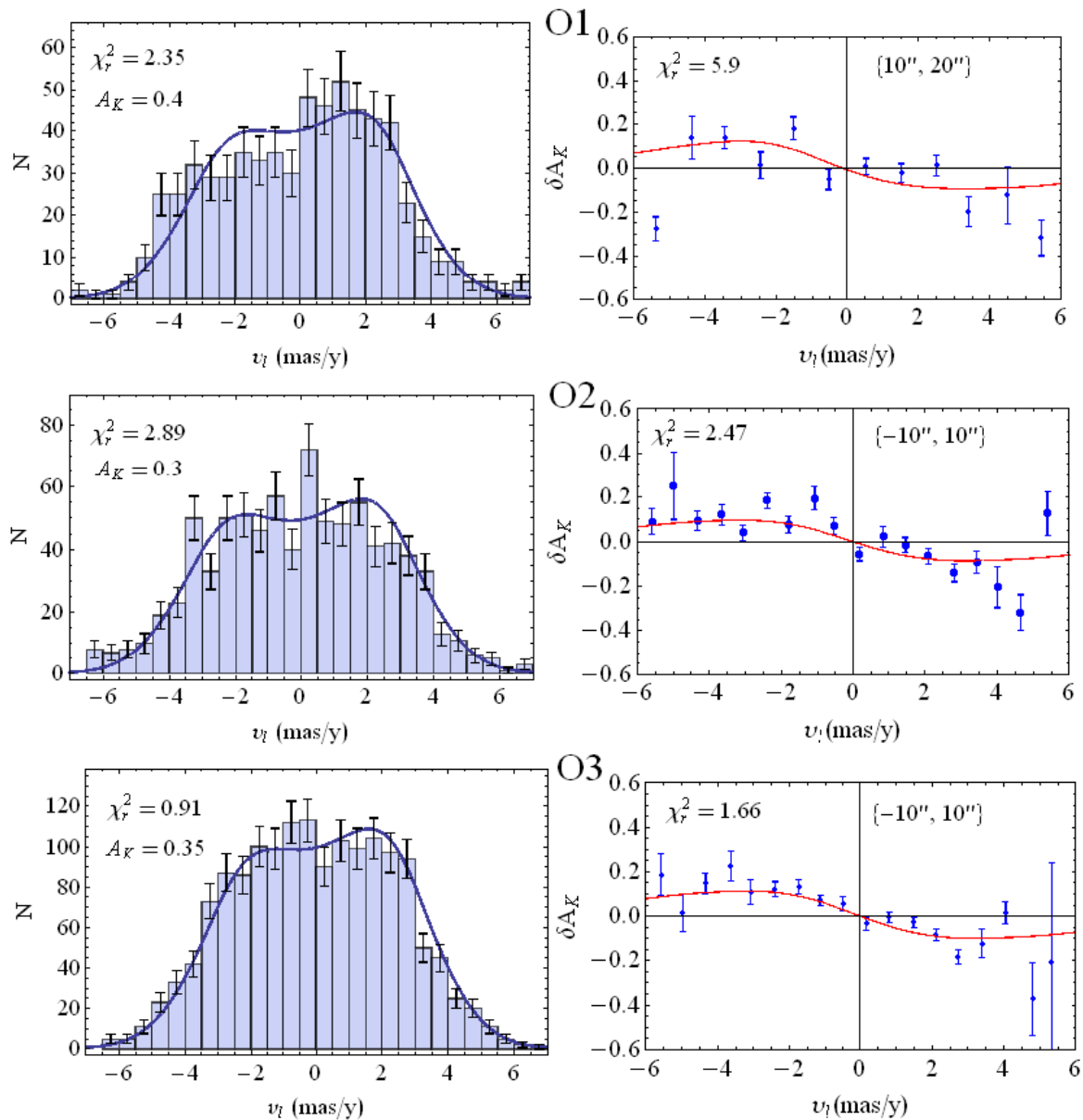


Figure 3.12: Predictions of the model with the VH and δA_K data for the outer cells shown in Fig.3.3. The numbers in the brackets show where the screen of dust is placed relative to the center. Reduced χ^2 are also provided.

the VPs for this amount of extinction is very small. Specifically the average difference of the 2nd moments of the VPs between the two models is $\sim 1.5\%$. If instead we use $A_K = 0.4$, close to the average extinction within the NSC inferred from this work, the difference is smaller than 0.5%. The relative differences of σ_{los}/σ_b and σ_{los}/σ_l between the model with no dust and the model with $A_K = 0.4$ are similarly small, 0.2% and 0.6%, respectively. Therefore we conclude that the systematic effects on the statistical parallax due to dust are within the estimated errors of Chatzopoulos et al. (2015), causing the distance to the NSC to decrease by $\sim 0.4\% \simeq 30\text{pc}$.

That the changes in the even part are so small can be explained by the following formal argument for the VP_l . We show that for small amounts (1st assumption) of homogenized (2nd assumption) dust around the center the even part of the renormalized VP in v_l is the same as that for no dust. The odd part is a direct indicator of dust at that point (l, b) and can be used to estimate A_K .

When the luminosity function is a power law and the dust is homogeneously placed i.e. $y_1 = -y_2$ in equations 3.3 and 3.4, $p(y)$ takes the form within the dust area:

$$p(y) = L(-a_K(y)) = 10^{-\gamma\left(\frac{A_K}{2} + \frac{A_K y}{\Delta y}\right)} \quad (3.9)$$

For small $A_K \ll (\gamma \ln(10))^{-1} \simeq 1.61$ we have:

$$\begin{aligned} p(y) &\simeq 1 - \gamma \ln(10) \frac{A_K}{2} - \gamma \ln(10) \frac{A_K}{\Delta y} y \\ &= p(0) - ky \end{aligned} \quad (3.10)$$

where $p(0) = 1 - \gamma \ln(10) \frac{A_K}{2}$ and $k = \gamma \ln(10) \frac{A_K}{\Delta y}$.

Therefore¹ the function $g(y) = p(y) - p(0)$ is odd everywhere (including the area where there is no dust). Next for simplicity we use $f_{tot}(E, L_z) = f(E, xv_{los} - yv_l) \rightarrow f(v_ly)$ because y appears within f only with the form of y^2 and v_ly .

Now we have:

$$\begin{aligned} &\frac{1}{2} \int p(y) \iint (f(v_ly) + f(-v_ly)) dv_z dv_{los} dy \\ &- \frac{1}{2} \int p(0) \iint (f(v_ly) + f(-v_ly)) dv_z dv_{los} dy = \\ &\frac{1}{2} \int g(y) \iint (f(v_ly) + f(-v_ly)) dv_z dv_{los} dy = 0 \end{aligned} \quad (3.11)$$

The previous is 0 because $g(y)$ is an odd function and $\iint (f(v_ly) + f(-v_ly)) dv_z dv_{los}$ is an even function of y therefore:

$$\begin{aligned} &\frac{1}{2} \int p(y) \iint (f(v_ly) + f(-v_ly)) dv_z dv_{los} dy = \\ &\frac{1}{2} p(0) \iiint (f(v_ly) + f(-v_ly)) dv_z dv_{los} dy \end{aligned} \quad (3.12)$$

¹we showed this for the case where the luminosity function is a power law but the same holds in the general case $L(m)$ where $\gamma \cdot \ln(10)$ is replaced by $\frac{\int L'(m)C(m)dm}{\int L(m)C(m)dm}$.

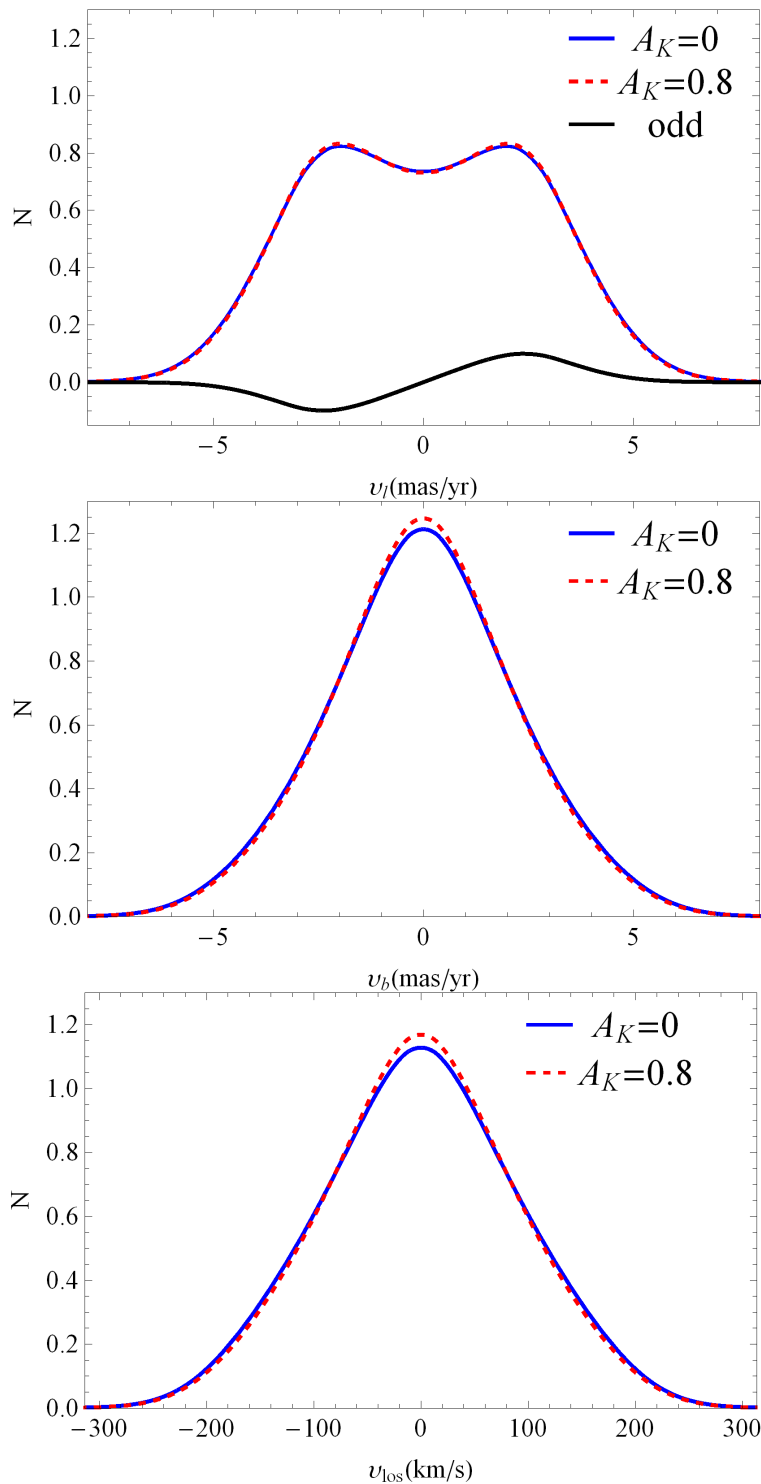


Figure 3.13: Even part of the renormalized VPs for v_t , v_b and v_{los} for a NSC dynamical model with no dust (best model from Chatzopoulos et al. (2015)) and the same dynamical model including the dust screen prediction based on cell B. The black line in the upper panel corresponds to the odd part of the VP_t . The VPs are calculated at the center of cell B.

And thus:

$$\text{VPD}_{\text{even}}(v_l) = p(0)\text{VP}_1(v_l) \quad (3.13)$$

To find the constant $p(0)$ we integrate once more over the velocity this time:

$$\int \text{VPD}_{\text{even}}(v_l) dv_l = p(0) \int \text{VP}_1(v_l) dv_l = p(0) \quad (3.14)$$

Therefore $p(0)$ is the normalization factor of the VPD_1 . The above means that to first order, dust does not affect the even part of the VPD in l direction significantly except for a scale factor. Fig 3.13 shows that the effects for VPD_b and VPD_{los} are similarly small. If extinction within a stellar system is small enough ($A_K \ll 1.6$ for the NSC) then fitting the even part of a model's VPs to the even part of the VHs is sufficient to get accurate estimates of the M_\bullet , M_* and R_0 parameters. In Chatzopoulos et al. (2015) we used the root mean square velocities that are moments of the even parts of the VHs to fit the M_\bullet , M_* and R_0 parameters of the axisymmetric model. Therefore we expect that their values will not be affected from the dust more than 0.4% as we explained earlier.

In principle the odd part of the VPD_1 can be fitted to the odd part of the VHs and this part is scale free since the scaling factor is already known from the even part therefore one can fit the A_K for some combination of cells.

3.7 Discussion & Conclusions

The main goal of this work was to understand the slight asymmetries in the VP_l s of the NSC and their influence on the dynamical modeling following the recent work of Chatzopoulos et al. (2015). Our interest was triggered by the observation that the right peak of the VH_l is consistently slightly higher than the left. A plausible explanation was given based on the existence of dust *within* the NSC. Because of the dust, the apparent number of stars behind the NSC is smaller than that in front of the cluster. This in conjunction with the rotation can explain the observed characteristic.

In order to quantify the dust effects, we worked with proper motions and photometry for ~ 7100 stars from Fritz et al. (2014). We applied an analytic dust extinction model together with our current best NSC dynamical model. The extinction model gave us reasonable results and was able to predict both the signature in the VPs and the photometry.

Observation of the NSC in the optical is almost impossible because of the 30 mag extinction. In the infrared the situation is much better since $A_K \sim 3$ mag. Most of this extinction belongs to the foreground and does not affect the shape of the VHs (except of a normalization factor). We find here that a small fraction of the total extinction value ($\sim 15\%$) belongs within the NSC.

The area between $\sim 1 - 1.5$ pc radius consists of several streamers of dust, ionized and atomic gas with temperatures between $100K - 10^4K$ and is called "ionized central cavity" (Ekers et al., 1983). The mini-spiral is a feature of the ionized cavity, and is formed from several streamers of gas and dust infalling from the inner part of the CND (Kunneriath et al., 2012). It consists of four main components: the Northern arm, the Eastern arm, the Western arm and the Bar (Zhao et al., 2009) that can be described well by streams of ionized gas or filaments orbiting Sgr A* (Serabyn & Lacy, 1985).

We investigated how well the mini-spiral correlates with the extinction effects in the NSC data within the central field. To assess this we first investigated whether our extinction model puts the dust on the same side of the NSC as does the mini-spiral interpretation. This is true for six out of the eight cells (except cells C2 & F). We also found the largest extinction ($A_K = 0.8$) in cell B where also the largest extinction is inferred from the extinction map of Scoville et al. (2003), and particularly low extinction in cell A where the extinction map is consistent with only foreground extinction.

We can estimate the mass that corresponds to a given amount of extinction using

$$\rho_d = \frac{A_K}{\Delta y} \frac{1}{1.086\kappa_\lambda} \quad (3.15)$$

where ρ_d is the dust density, $\kappa_\lambda = 1670\text{cm}^2/\text{g}$ (Draine, 2003a) is the mass extinction coefficient² for the K-Band, $A_K = 0.4$ from the model prediction and $\Delta y = 10''$ is the width of the dust screen. We find that $\rho_d \simeq 1.8 \times 10^{-19}\text{kg}/\text{m}^3$ and the dust mass within a parallelepiped with dimensions $(10'', 40'', 40'')$ centered on Sgr A* is $M_d \sim 3M_\odot$. Since the dust extinction model presented here is not precise we consider that this estimate is correct only within an order of magnitude. This value is within the range of $0.25 - 4M_\odot$ for the mini-spiral found from other works (Zylka et al., 1995; Kunneriath et al., 2012; Etxaluze, 2011).

Finally we showed that for small values of extinction the even parts of the VPs are not affected significantly. As a result, the measured M_\bullet , M_* and R_0 parameters of Chatzopoulos et al. (2015) do not change by more than $\sim 0.4\%$ for extinction $A_K \simeq 0.4$, which is less than the smallest systematic error (for the statistical parallax) inferred for these parameters in Chatzopoulos et al. (2015).

Our results can be summarized as follows:

- We showed that extinction due to dust explains kinematic asymmetries and differential photometry of the NSC, and measured the amount of extinction within the NSC by combining a dynamical model with a dust extinction model.
- We presented an extinction table for the dust *within* the NSC in several cells.
- We found that the distribution of the dust is consistent with the extinction being associated with the mini-spiral for 6 out of 8 cells.
- Systematic effects due to dust with typical extinction $A_K \simeq 0.4$ affect the M_\bullet , M_* and R_0 parameters deduced from previous dynamical modeling only by $\simeq 0.4\%$, which is smaller than their estimated systematic errors.

²ftp://ftp.astro.princeton.edu/draine/dust/mix/kext_albedo_WD_MW_3.1_60_D03.all

Chapter 4

Summary and Outlook

4.1 Summary

The main subject of this work was the study of the old nuclear star cluster in the Milky Way mainly from a dynamical point of view. A star cluster in general is a group of stars that is gravitationally bound. Open star clusters typically contain up to a few hundred of stars and they tend to be young and irregularly shaped. In contrast globular clusters are old, more compact (and subsequently more spherical) and contain up to one million stars. Nuclear Star clusters (NSC) are compact conglomerations of stars like globular clusters, but they are located at the centers of most spiral galaxies and generally contain multiple populations of stars. Also a NSC is more luminous and more massive than a globular cluster and hosts at its center a super-massive black hole (SMBH). The study of NSCs is of great interest because several of the most extreme physical phenomena occur within them such as SMBHs, active galactic nuclei, star-bursts and extreme stellar densities.

The NSC of the Milky Way is of exceptional interest because of its proximity, about 8 kpc from Earth. Because of high interstellar extinction that is caused by dust, it is really impossible to observe the NSC with an optical telescope. Therefore we rely on observations taken in the infrared because the dust is more transparent for longer wavelengths. One additional goal of this work was to see the impact of the dust on the apparent dynamics of the NSC and also present a measurement of dust extinction *within* the NSC.

4.1.1 Modeling the NSC

To model the NSC we worked with ~ 2500 radial velocities (velocities along the line of sight) and ~ 10000 proper motions (perpendicular to the line of sight) plus stellar number counts from Fritz et al. (2014). Before this work the best models in the literature for the NSC were spherical Jeans models (e.g. Trippe et al., 2008). Therefore we decided for this project to apply 2-Integral distribution functions (DF) that possess considerable advantages over Jeans modeling but are also much more complicated to implement. A DF gives the number of stars in phase space as a function of the position and the velocity. Therefore if one knows the DF of a system one knows the probability that a star has phase-space coordinates in a given range. The best indicator for the quality of the modeling was the good prediction of the Velocity Profiles (VP) since those

are equivalent to all the moments of the system. Even though a 2-I DF is not the most general case, it gave us overall very good results and makes the model presented here, the best current description of the NSC dynamics available in the literature.

The inflection point observed at about $\sim 200''$ ($\sim 8\text{pc}$) in the star count map derived in Fritz et al. (2014) suggests two components in the NSC density profile. To account for this we constructed a two-component dynamical model for the star counts in which the two components are described as independent γ -models. This disentanglement works well for both the spherically averaged number density of late-type stars versus projected radius but also for the number density along l and b directions. The inner, rounder component can be considered as the NSC, as in Fritz et al. (2014), while the outer, much more flattened component represents the inner parts of the nuclear stellar disk described in Launhardt et al. (2002).

The radius of influence of the SMBH is $r_h \sim 90''$ (Alexander, 2005) is close to the scale radius $\sim 100''$ of the inner component. The surface density profile of the NSC flattens inside $\sim 20''$ to a possible core (Burkert, 2009; Fritz et al., 2014) but the slope of the three-dimensional density profile for the inner component is not well-constrained.

The flattening for the inner NSC component inferred from star counts is $q_1 = 0.73 \pm 0.04$, very close to the value of $q = 0.71 \pm 0.02$ found recently from Spitzer multi-band photometry (Schödel et al., 2014). These determinations agree with the dynamical flattening of our best Jeans dynamical models: the dynamical flattening is robust because it is largely determined by the ratio of σ_b/σ_l and the tensor virial theorem. Because star counts, photometric, and dynamical values for the inner NSC flattening agree, this parameter can now be considered securely determined.

4.1.2 Distance to the Galactic Center

One of the goals of this work was the estimation of the distance R_0 to the GC. Even though it is known that the distance to the GC is about 8.5 kpc, the exact value is a subject of research. The knowledge of the exact value of the distance is very important because several quantities (e.g. distances and masses) scale according to it. Recent work yields results between 7.2 kpc (Bica et al., 2006) and 8.92 kpc (Do et al., 2013) depending on the method. Measurements of R_0 prior to 2010 were reviewed by Genzel et al. (2010). Their weighted average of direct measurements is $R_0 = 8.23 \pm 0.20 \pm 0.19$ kpc, where the first error is the variance of the weighted mean and the second the unbiased weighted sample variance.

In this work we use our large proper motion and line-of-sight velocity datasets to obtain a new estimate for the statistical parallax distance to the NSC using axisymmetric Jeans modeling based on the cluster's inferred dynamical structure. The use of semi-isotropic Jeans modeling is justified since we found that the VPs of the NSC can be well approximated by a 2-Integral DF $f(E, L_z)$. From matching our best dynamical model to the proper motion and line-of-sight velocity dispersions within approximately $|l|, |b| < 50''$, and varying simultaneously M_\bullet , M_{NSC} , and R_0 we found $R_0 = 8.27 \pm 0.09|_{\text{stat}} \pm 0.1|_{\text{sys}}$ kpc. The small statistical error is indicative to the large number of fitted dispersion points. This value is close to the direct estimate $R_0 = 8.33 \pm 0.35$ kpc found by Gillessen et al. (2009) from analyzing stellar orbits close to Sgr A*. A joint statistical analysis of the NSC data with the orbit results of Gillessen et al. (2009) gives a new best value and error $R_0 = 8.33 \pm 0.11$ kpc (Fig. 2.12, Section 2.4.2).

The value of the distance presented here is consistent with recent measurements. Recently Reid et al. (2014) found $R_0 = 8.34 \pm 0.14$ kpc from fitting axially symmetric disk models to

trigonometric parallaxes of star forming regions. (Dekany et al., 2013) found $R_0 = 8.33 \pm 0.05|_{\text{stat}} \pm 0.14|_{\text{syst}}$ from RR Lyrae stars. Both values are consistent with each other and with our distance value from the statistical parallax of the NSC, with or without including the results from stellar orbits around Sgr A*, and the total errors of all three measurements are similar, $\sim 2\%$.

4.1.3 Mass of the NSC

We showed that the NSC model can be described well as a superposition of a moderately flattened nuclear cluster embedded in a highly flattened nuclear disk. The NSD starts to dominate at about $800''$ which is in good agreement with the value found by Launhardt et al. (2002).

By applying axisymmetric Jeans modeling to the dataset we were able to constrain the mass of the cluster. The estimated mass of the cluster is $M_*(m < 100'') = (7.73 \pm 0.31|_{\text{stat}} \pm 0.8|_{\text{syst}}) \times 10^6 M_\odot$ interior to a spheroidal major axis distance $m = 100''$ close to the inflection point observed in the surface density data. This corresponds to an enclosed mass within 3-dimensional radius $r = 100''$ of $M_*(r < 100'') = (8.94 \pm 0.31|_{\text{stat}} \pm 0.9|_{\text{syst}}) \times 10^6 M_\odot$, where the estimated systematic errors account for additional uncertainties in the dynamical modeling. The mass within 1 pc ($\sim 25''$) is $M_*(r < 1\text{pc}) = 0.89 \times 10^6 M_\odot$. This is compatible with the spherical modeling of Schödel et al. (2009) who gave a range of $0.6 - 1.7 \times 10^6 M_\odot$, rescaled to $R_0 = 8.3$ kpc, with the highest mass obtained for their isotropic, constant M/L model.

The total mass of the inner spheroidal component, $M_1 = 6.1 \times 10^7 M_\odot$, is well-determined within similar relative errors as $M_*(m < 100'')$. However, identifying M_1 with the total mass of the Galactic NSC at the center of the nuclear disk has considerable uncertainties: because the outer NSD component dominates the surface density outside $100'' - 200''$, the NSC density profile slope at large radii is uncertain, and therefore the part of the mass outside $\sim 200''$ ($\sim 64\%$ of the total) is also uncertain. A reasonable estimate for the mass of the inner NSC component is up to where it dominates the star counts $\sim 200''$, which gives $M_{\text{NSC}} > 2 \times 10^7 M_\odot$.

An important point to note is that the cluster mass does not depend on the net rotation of the cluster but only on its flattening. This is because to add rotation self-consistently to the model we need to add an odd part to the DF in L_z which does not affect the mass, density nor the proper motion dispersions σ_l and σ_b .

Finally, we used our inferred dynamical cluster mass to update the K-band mass-to-light ratio of the NSC. The best-determined mass is within $100''$. Comparing our $M_*(r < 100'') = (8.94 \pm 0.31|_{\text{stat}} \pm 0.9|_{\text{syst}}) \times 10^6 M_\odot$ with the K-band luminosity of the old stars derived in Fritz et al. (2014), $L_{100''} = (12.12 \pm 2.58) \times 10^6 L_{\odot, \text{Ks}}$, we obtain $M/L_{\text{Ks}} = (0.76 \pm 0.18) M_\odot / L_{\odot, \text{Ks}}$. The error is dominated by the uncertainty in the luminosity (21%, compared to a total 10% in mass from adding statistical and systematic errors in quadrature). The inferred range is consistent with values expected for mostly old, solar metallicity populations with normal IMF (e.g. Courteau et al., 2013; Fritz et al., 2014).

4.1.4 Mass of the Supermassive Black Hole

Given a dynamical model, it is possible to constrain the mass of the central black hole from 3D stellar kinematics of the NSC alone. With the axisymmetric Jeans modeling we found $M_\bullet = (3.86 \pm 0.14|_{\text{stat}} \pm 0.4|_{\text{syst}}) \times 10^6 M_\odot$, where the systematic modeling error is estimated from the difference between models with different inner cluster flattening as discussed in Section 2.4.2.

Previous works underestimated the mass of the central black hole (e.g. Trippe et al., 2008). Our analysis provides a mass for Sgr A* in agreement with the value determined from stellar orbits around Sgr A* (Gillessen et al., 2009).

Our dataset for the NSC is the largest analyzed so far, and the axisymmetric dynamical model is the most accurate to date; it compares well with the various proper motion and line-of-sight velocity histograms. Nonetheless, future improvements may be possible if the uncertainties in the star density distribution and kinematics within $20''$ can be reduced, the effects of dust are incorporated, and possible deviations from the assumed 2I-axisymmetric dynamical structure are taken into account.

The conceptually best method to determine the black hole mass is from stellar orbits close to the black hole (Schödel et al., 2002; Ghez et al., 2008; Gillessen et al., 2009), as it requires only the assumption of Keplerian orbits and is therefore least susceptible to systematic errors. Gillessen et al. (2009) find that the largest uncertainty in the value obtained for M_\bullet is due to the uncertainty in R_0 , and that M_\bullet scales as $M_\bullet \propto R_0^{2.19}$. Therefore using our improved statistical parallax for the NSC also leads to a more accurate determination of the black hole mass. A joint statistical analysis of the axisymmetric NSC modeling together with the orbit modeling of Gillessen et al. (2009) gives a new best value and error for the black hole mass, $M_\bullet = (4.26 \pm 0.14) \times 10^6 M_\odot$ (see Fig. 2.12, Section 2.4.2). An additional systematic error of 0.1 kpc for R_0 in the NSC modeling, through the BH mass-distance relation given in Gillessen et al. (2009), translates to an additional uncertainty $\simeq 0.1 \times 10^6 M_\odot$ in M_\bullet .

4.1.5 Dust within the NSC

The area between $\sim 1 - 1.5$ pc radius centered at Sgr A* consists of several streamers of dust, ionized and atomic gas with temperatures between $100K - 10^4K$ and it is called “ionized central cavity” (Ekers et al., 1983). An important feature of the ionized cavity is the so called “mini-spiral”, named after its distinctive shape that resembles a spiral. Outside of the mini-spiral (and the ionized cavity) at radius $\sim 1.5 - 4$ pc lies the circumnuclear disk (CND) which is a set of streamers of dense molecular gas and warm dust (Becklin et al., 1982; Guesten et al., 1987). The gas density of the CND is higher than that of the mini-spiral and there is a sharp transition at ~ 1.5 pc. The total mass of the ionized gas in the central cavity is quite small $\sim 30M_\odot$. Additionally there is about $300M_\odot$ of dense neutral hydrogen gas, a few M_\odot of warm dust (Davidson et al., 1992) and an inferred inflow rate into the central parsec of $3 \times 10^{-2} M_\odot \text{yr}^{-1}$ (Jackson et al., 1993).

One of the goals of this thesis was to understand the slight asymmetries in the VP_{lS} (velocity profiles in l direction) of the NSC and their influence on the dynamical modeling following the recent work of Chapter 2 (Chatzopoulos et al., 2015). Our interest was triggered by the observation that the right peak of the VH_l (velocity histogram in l direction) is consistently slightly higher than the left. A plausible explanation was given based on the existence of dust *within* the NSC possibly correlated with the mini-spiral. Because of the dust, the apparent number of stars behind the NSC is smaller than that in front of the cluster. This in conjunction with the rotation can explain the observed characteristic.

In order to quantify the dust effects, we worked with proper motions and photometry for ~ 7100 stars from Fritz et al. (2014). We applied an analytic dust extinction model together with our current best NSC dynamical model. The extinction model gave us reasonable results

and was able to predict both the signature in the VPs and the photometry.

To implement the extinction model, first we modeled a luminosity function. This was expressed as the product of an exponential magnitude distribution with an error function that represents the completeness function. Next we needed the extinction variation over the line-of-sight which is just the derivative of the extinction over the line-of-sight. Having those we then calculated the percentage reduction in observed stars as a function of line-of-sight which allowed us to finally calculate the VPs including the effect of dust.

Next we split the central area of the mini-spiral map into eight cells according to certain criteria. To assess how well the mini-spiral correlates with the extinction effects in the NSC data, we first investigated whether our extinction model puts the dust on the same side of the NSC as does the mini-spiral interpretation. This is true for six out of the eight cells. We also found the largest extinction ($A_K = 0.8$) where also the largest extinction is inferred from the extinction map of Scoville et al. (2003), and particularly low extinction ($A_K = 0.15$) where the extinction map is consistent with only foreground extinction. Finally we found that the typical values for the extinction within the NSC and foreground extinction are respectively $A_K \sim 0.4$ and $A_K \sim 2.7$.

4.2 Outlook

A semi-analytical dynamical model of the NSC with excellent overall predictions is presented. The model is a 2-Integral DF $f(E, L_z)$ based on the algorithm of Hunter & Qian (1993) and Qian et al. (1995) which is a generalization of Eddington's formula. Unfortunately semi-analytic expressions for distribution functions similar to Eddington's formula more general than $f(E, L_z)$, like 3-Integral DFs systems are not available and in these cases we have to rely on potentials of specific form (e.g. Stäckel potential family) or on numerical methods. The available potentials for a 3-Integral DF are very limited in their scope therefore the next logical step is to model the NSC with a particle or an orbit based method.

Our group possesses a parallelized implementation (NMAGIC De Lorenzi et al., 2007) of a made-to-measure scheme based on Syer & Tremaine (1996) that could be used to further model the NSC. Initially we need a particle model of the NSC that is based on our best 2-Integral $f(E, L_z)$ DF of the NSC from Chapter 2. The DF can be sampled in order to produce the particle model. For equal mass particles, this is usually done by applying a rejection method to the even part of the DF to draw the positions and velocities of the particles and then reversing the velocity of each particle with some probability in order to add rotation. This procedure is explained well in van der Marel et al. (1997) and its first part (particle model for the even part of the DF) is already implemented. However, as it is explained in the Appendix A an equal mass particle model has limitations especially if the goal is to model the center of the NSC where the small number of particles there will introduce additional uncertainties, for example in the estimate of the mass of the super-massive black hole. In addition the new multimass models with the increased resolution near the center might also shed some light on the core-cusp issue. One possible solution is to use a multi-mass particle model (e.g. Zhang & Magorrian, 2008; van der Marel et al., 1997) as in Appendix A. However multi-mass particle models introduce additional complexities as they are much more difficult to implement especially for flattened systems, and one has to be careful about the ratio between the maximum and minimum mass of the model in order to preserve the stability of the system especially for a non-static potential.

Once the problems of the previous paragraph has been addressed we have to check the stability

of the particle model for the NSC. A particle model that is drawn from a DF is in dynamical equilibrium, however it may be unstable for several reasons, one of them is excessive flattening. Our NSC model has two components as described in Chapter 2, the first one represents the spheroidal part of the NSC with $q_1 = 0.73$ and the second represents the nuclear disk with $q_2 = 0.28$. As a result the flattening varies monotonically between these two values. At a distance of $1000''$ the flattening is $q \simeq 0.5$. From van der Marel et al. (1997) we know that $f(E, L_z)$ models are generally stable for $q \geq 0.55$ and maybe for flatter systems. However it is possible to observe small signs of instability for distances larger than $1000''$ that may affect inner regions, a problem which has to be addressed if it is true.

In Chapter 3 we showed evidence that the observed asymmetry in v_l velocity histograms of the NSC may be caused by dust located within the central parsecs of the Galactic Center. In order to use the particle model we also have to incorporate those dust effects within the NMAGIC code. The quantity we need is the percentage reduction in observed stars as a function of line-of-sight distance, denoted as $p(y)$ in Chapter 3. This quantity depends on the luminosity function of the NSC and on the extinction value A_K within the NSC and is provided in Chapter 3 for several cells in the central region.

With this prescription we should be ready to explore further the dynamics of the NSC. This work is mostly focused on explaining the observed dynamics of the NSC and their effect on the velocity histograms. Although a good deal of progress has been made there are still some unexplained aspects on the velocity histograms. In Figure 4.1 we see a typical velocity distribution for v_l with the corresponding velocity histograms along with the odd part of the model and the data. We know from Chapter 3 that the odd part is a direct indicator of the dust for a specific field. However we notice that the data do not follow the model as expected for medium to large velocities ($\sim \pm 150$ km/s) something that is clearer in the odd part. This additional asymmetry is observed in several areas on the (l, b) plane. The cause of this signature is unknown and it might be a manifestation of the third integral, the result of an yet unknown effect or just an artifact of the data.

In Chapter 3 we worked with surface density data and kinematical data in order to model the NSC. However the kinematic data were symmetrized. Specifically the radial velocities were mapped to positive Galactic latitudes and the proper motions were mapped to the first quadrant of the (l, b) plane. This allowed us to avoid additional possible complexities introduced by inclination and triaxiality but also this tactic hides any potential substructure of the NSC. Further modeling of the NSC would require to unfold the kinematical data in order to reveal a hidden substructure if any (e.g. Feldmeier et al., 2014) and model the NSC as a more general triaxial and possibly slightly inclined system. In addition, recently it was suggested that there is a misalignment (Feldmeier et al., 2014; Fritz et al., 2014) about $\sim 10^\circ$ of the radial velocity data to the galactic plane. However this cannot be confirmed for the proper motions (Fritz et al., 2014). Therefore there is a possibility that the suggested misalignment is not truly a misalignment but rather a signature of the internal dynamics of the NSC.

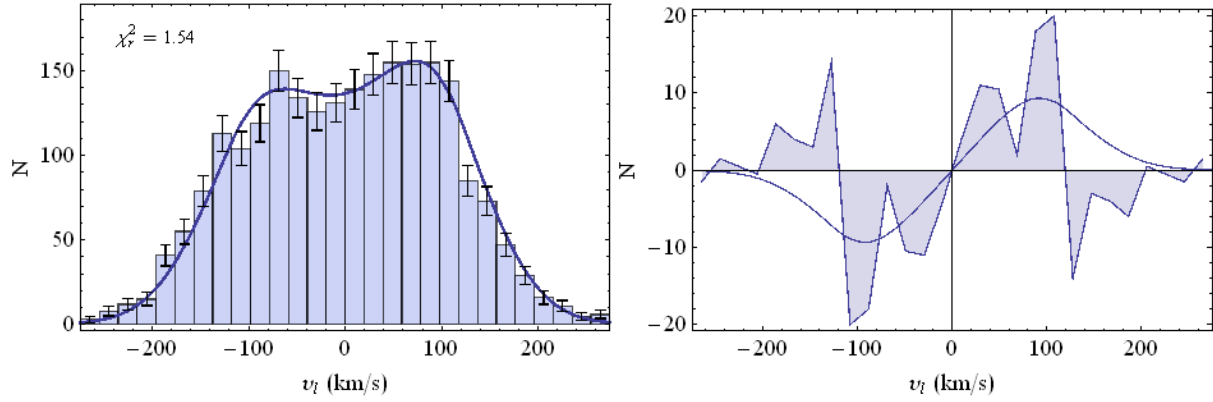


Figure 4.1: Typical velocity distribution for v_l with the corresponding velocity histograms (left) along with the odd part of the model and the data (right). The odd part is a direct indicator of dust at that point (l, b) and can be used to estimate A_K . We notice the data do not follow the model as expected for medium to large velocities $\sim \pm 150$ km/s.

Appendix A

Multi-mass N-body realizations

During the first months of my PhD, I have implemented and tested the multi-mass scheme described in Zhang & Magorrian (2008). This is a general scheme for constructing high resolution Monte-Carlo realizations of equilibrium collisionless galaxy models with a known distribution function (DF). In the remainder of this section, I describe this scheme in more detail.

Over the past few decades the use of N-body simulations has become more and more prominent. The vast majority of these simulations make use of equal mass particle models. The goal of multi-mass N-body simulations is to increase accuracy in “interesting” regions of phase space. Suppose for example that we have to create an equal mass N-body realization from the Hernquist distribution function. The mass as a function of radius for this distribution (normalized) is:

$$M(r) = \left(\frac{r}{1+r} \right)^2 \quad (\text{A.1})$$

In an equal mass particle realization the number of particles within a given r is $N \cdot M(r)$. This means that for 10^6 particles the number of particles within radius of $r = 0.001$ is ~ 1 . We can make a rough estimation of the number of particles needed to resolve the sphere of influence of a black hole. Let us define the radius of influence of the black hole as the radius where the sum of the mass of the particles is equal to the mass of the black hole. N_0 is the total number of particles and N_{res} is the number of particles that we need within the radius of influence r_h .

$$M(r_h) = \lambda \rightarrow N_0 M(r_h) = N_0 \lambda = N_{res} \rightarrow N_0 = N_{res} / \lambda \quad (\text{A.2})$$

From observations $\lambda \sim 10^{-3}$ (because the ratio $\lambda = M_\bullet / M_{total} \sim 10^{-3}$ and $M(r)$ is normalized to 1). Now suppose that we want 100 or more particles within $0.1r_h$, which is $N_{res} = 10^4$ within r_h for a Hernquist model. Therefore we need a minimum number of equal mass particles:

$$N_0 = 10^7 \quad (\text{A.3})$$

This makes it very difficult to resolve regions close to the black hole at the center of a galaxy with a reasonable number of particles. By using multi-mass schemes we can increase the number of particles in areas of interest like the center of a galaxy. The use of multi-mass schemes is

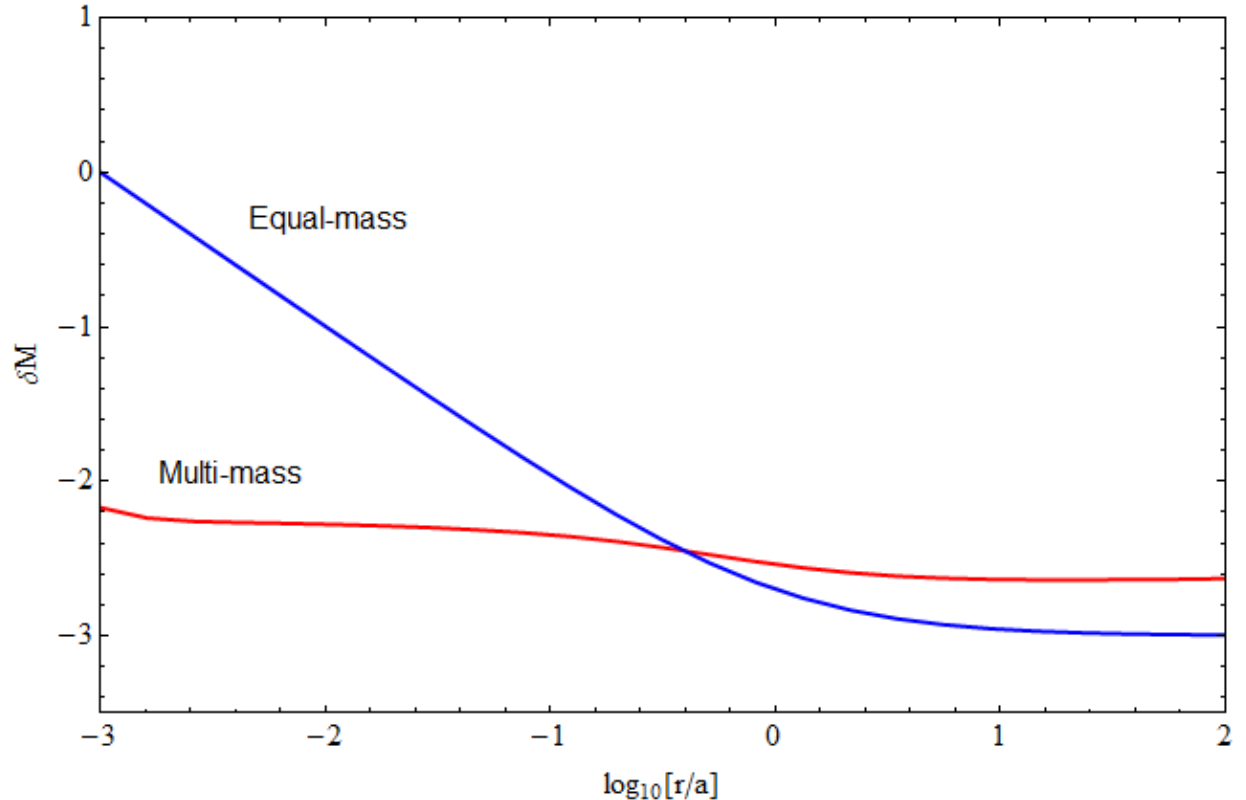


Figure A.1: Formal relative errors in mass included in logarithmically placed spherical cells of a Hernquist model for 10^6 particles for an equal and multi-mass particle realization. The errors in the multi mass model are more than two orders of magnitude smaller near the center than the errors in the equal mass realization.

the literature is relatively limited. Sigurdsson & Hernquist (2008) used a heuristic multi-mass technique to increase the efficiency of their models of galaxies with central black holes. Zhang & Magorrian (2008) devised a multi-mass technique that uses importance sampling on a given distribution to reduce the errors of given quantities (i.e. like the error in mass in a spherical cell between a Hernquist model and the particle realization). In Fig. A.1 we can see how the Zhang & Magorrian (2008) (ZM) technique behaves against an equal mass realization by comparing the relative errors in mass included in logarithmically placed spherical cells. Simply speaking the algorithm separates the mass distribution function from the number distribution function (both are the same in the equal mass case). As a result, near the center we have more particles with smaller masses and as the radius increases the mass of the particles also increases.

A.0.1 Criticism on the ZM multi-mass scheme

In Fig. A.2 we see that the ratio between the maximum and minimum particle mass of the model is $\sim 10^8$. This is highly unusual because until now the ratio of masses in the literature is 3-4 (Sigurdsson & Hernquist, 2008; Weinberg & Katz, 2007; Sellwood, 2008) and this raises the

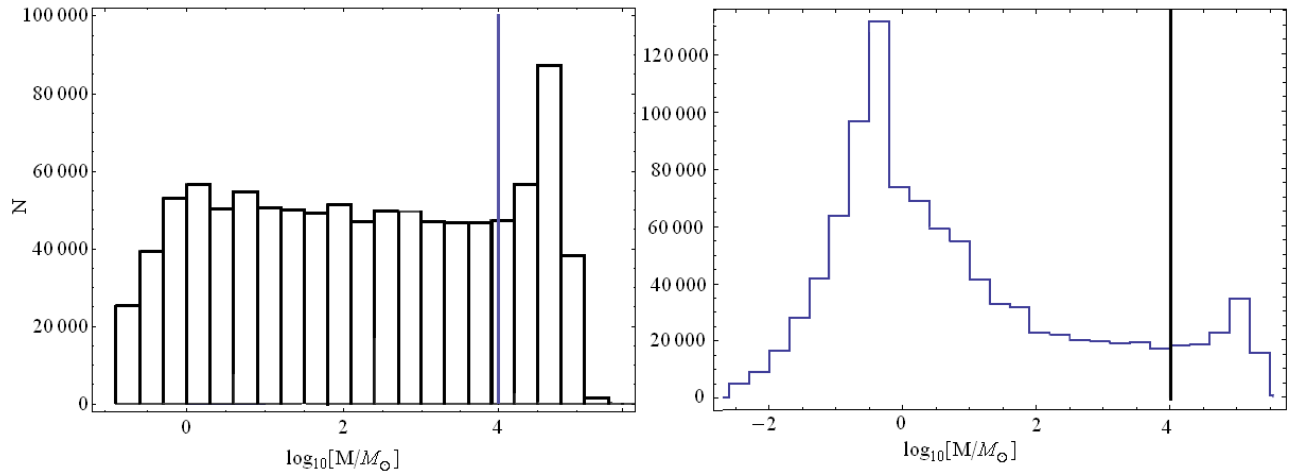


Figure A.2: Left: A Hernquist multi-mass realization with $N = 10^6$ particles based on the Zhang & Magorrian (2008) algorithm. The total mass of the galaxy is scaled to $M_* = 10^{10} M_\odot$. The range of 8 decades in mass gives sub-solar mass resolution in “interesting” regions of phase space. In contrast, in an equal-mass realization all particles would have mass $10^4 M_\odot$ (solid line). Right: As in left but also including a black hole with mass ratio equal to 10^{-3} of the total mass, similar to the ratio of the mass of the Galactic SMBH and the mass of the Galactic Bulge.

question of what might happen if a massive particle from the outer region with very small angular momentum visits the center. Ideally this model is in a statistical equilibrium which means that for every massive particle that visits the center there is another particle that goes out. We have done some initial tests by integrating the particles in their own static Hernquist potential. The model remains in equilibrium with some reasonable fluctuations. However we have not tested how the system behaves when the potential is calculated directly from the particles. The system probably will also be prone to unrealistic dynamical friction and may behave more like a collisional system instead of collisionless system.

A.0.2 Multi-mass and Made to Measure methods

NMAGIC is a recent tool developed mainly by Flavio de Lorenzi that makes use of a similar particle method as described by Syer & Tremaine (1996). This program is parallelized and can be used both as an N-body simulator, as a virtual telescope and (its main function) as a tool to make dynamical models of stellar systems. By using the particle based method we can fit an initial model to a target using data taken from real telescopes and use the final model to measure quantities of the system that are not accessible with real telescopes (e.g. observables and internal moments respectively) and eventually make predictions for a galaxy.

Initial tests show that a combination of multi-mass and made-to-measure methods can work. We started by fitting a multi-mass particle realization of a Hernquist model to an equal mass Hernquist model with a different scale factor. Fig. A.3 shows two snapshots of slit kinematics of the fitted multi-mass Hernquist particle realization. The error bars are the target equal mass particle model that has a scale factor of $a = 1.2$. The initial multi-mass particle model had a

scale factor of $a = 1$. The results are overall good.

The next step could be to test the multi-mass scheme by modeling a real system like the Nuclear Star Cluster (NSC). Initially a multi-mass particle model representing the NSC would be produced based on the spherical 2-component model of the NSC presented in Chapter 2. This model could later be flattened accordingly within our NMAGIC code. The increased resolution of the multi-mass particle model close to the center would help us understand better the core-cusp problem, help resolve with greater detail the area of influence of the SMBH, and in addition would possibly lead to more accurate estimates of the mass of the SMBH.

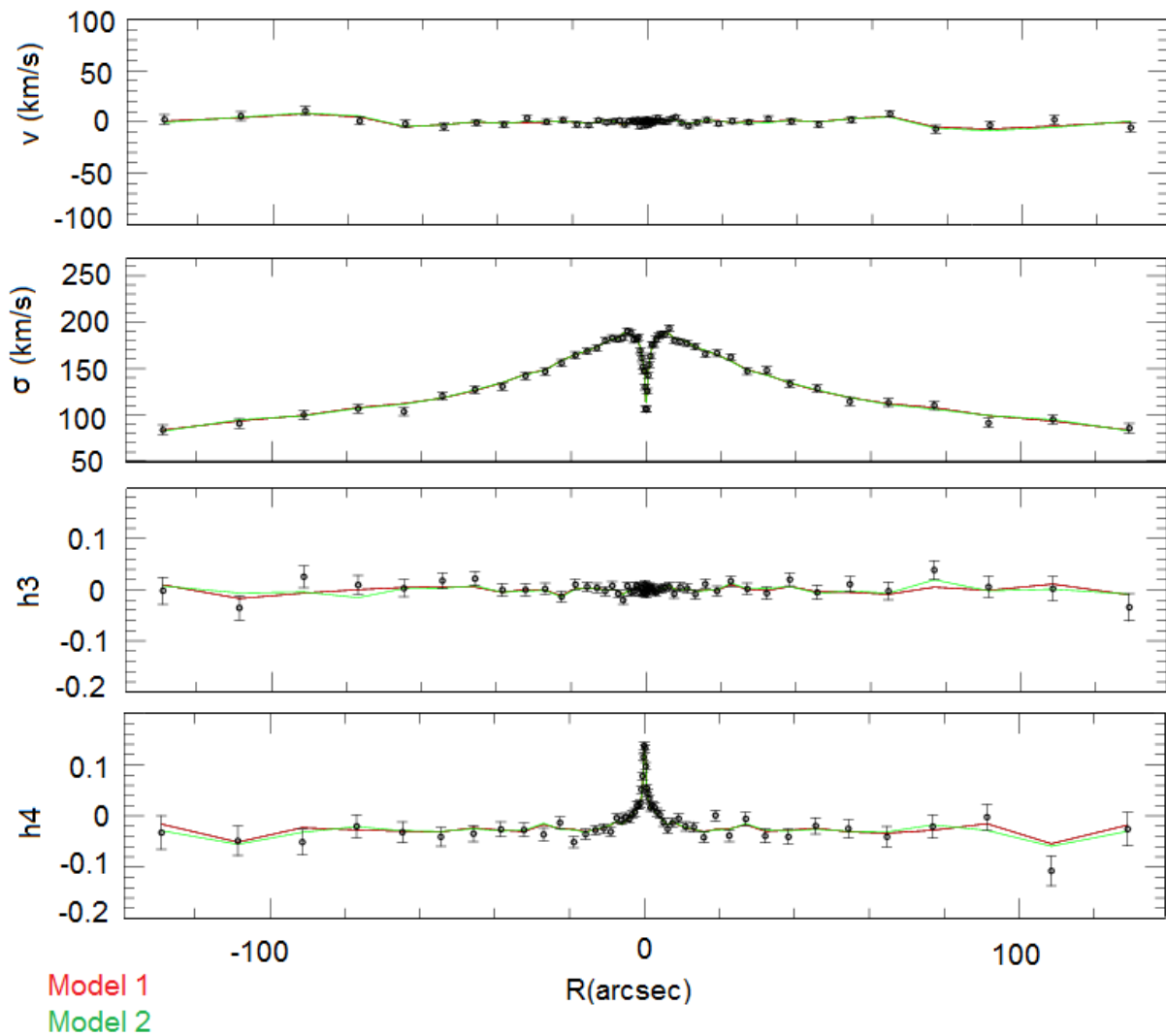


Figure A.3: Two snapshots of slit kinematics of the fitted multi-mass Hernquist particle realization without a black hole. The error bars are the target equal mass particle model that has a scale factor of $a = 1.2$. The initial multi-mass particle model had a scale factor of $a = 1$. The results are overall good.

Bibliography

- Aarseth S. J., Henon M., Wielen R. 1974 A&A 37,183
- Arca-Sedda M., Capuzzo-Dolcetta R., 2014c, MNRAS, 444, 3738
- Alexander T., 2005, Physics Reports, 419, 65
- Allen, D. A., & Sanders, R. H. 1986, Nature, 319, 191
- Antonini F., Capuzzo-Dolcetta R., Mastrobuono-Battisti A., Merritt D., 2012, ApJ, 750, 111
- Baes, M., Dejonge, H., & Buyle, P. 2005, A&A, 432, 411
- Bahcall J. N., Wolf R. A., 1976, ApJ, 209, 214
- Bartko, H., Martins, F., Trippe, S., et al. 2010, ApJ, 708, 834
- Becklin, E. E., & Neugebauer, G. 1968, ApJ, 151, 145
- Becklin, E. E., Gatley, I., & Werner, M. W. 1982, ApJ, 258, 135
- Bica E., Bonatto C., Barbuy B., Ortolani S., 2006, A&A, 450, 105
- Böker, T. 2010, IAU Symposium, 266, 58
- Böker T., Laine S., van der Marel R. P., et al., 2002, AJ, 123, 1389
- Böker T., Sarzi M., McLaughlin D. E., et al., 2004, AJ, 127, 105
- Böker T., 2010, IAUS 266, 50
- Bonnell I., Rice W., 2008, Science, 321, 1060
- Bovy J., Rix H.-W., Hogg D. W., 2012, ApJ, 751, 131
- Binney J. J., Tremaine S D., Galactic dynamics 2nd edition. Princeton University Press, Princeton
- Blum, R. D., Ramrez, S. V., Sellgren, K., & Olsen, K. 2003, ApJ, 597, 323
- Buchholz, R. M., Schodel, R., Eckart, A. 2009, A&A, 499, 483
- Bullock, J. S., Kolatt, T. S., Sigad, Y., et al. 2001, MNRAS, 321, 559

- Burkert, A. 2009, in ASP Conf. Ser. 419, *Galaxy Evolution: Emerging Insights and Future Challenges*
- Carney B. W., Latham D. W., Laird J. B., 1990, *AJ*, 99, 572
- Carollo, C. M., Stiavelli, M., & Mack, J. 1998, *AJ*, 116, 68
- Côté, P., et al. 2006, *ApJS*, 165, 57
- Cappellari M., 2008, *MNRAS*, 390, 71
- Chandrasekhar S., 1943, *ApJ*, 97, 255
- Chandrasekhar S. 1969, *Ellipsoidal Figures of Equilibrium*. Yale University Press, New Haven
- Chatzopoulos S., Fritz T., Gerhard O., Gillessen S., Wegg C., Genzel R., Pfuhl O., 2015, *MNRAS*, 447, 952
- Chatzopoulos, S., Gerhard, O., Fritz, T. K., Wegg, C., Gillessen, S., 2015, arXiv:1504.03699
- Chiba M., Beers T. C., 2000, *AJ*, 119, 2843
- Christopher, M. H., Scoville, N. Z., Stolovy, S. R., & Yun, M. S. 2005, *ApJ*, 622, 346
- Carollo C. M., Stiavelli M., de Zeeuw P. T., Mack J. 1997, *AJ*, 114, 2366
- Courteau S., et al., 2013, *RevModPhys*, in press
- Davidson, J. A., Werner, M. W., Wu, X., Lester, D. F., Harvey, P. M., Joy, M., Morris, M. 1992 *ApJ*, 387, 189D
- Deguchi S., Imai H., Fujii T., et al., 2004, *PASJ*, 56, 765
- Dehnen W., 1993 *MNRAS* 269, 250
- Dehnen W., Binney J., 1998, *MNRAS*, 294, 429
- Dehnen W., Gerhard O. E., 1994, *MNRAS*, 268, 1019
- Dejonghe H. B. 1986, *Phys. Re.*, 133, 218
- Dekany I., Minniti D., Catelan M., Zoccali M., Saito R.K., Hempel M., Gonzalez O.A., 2013, *ApJ*, 776, L19
- de Lorenzi, F., Debattista, V. P., Gerhard, O., and Sambhus, N. (2007), *MNRAS*, 376,71
- De Lorenzi F., Hartmann M., Debattista V. P., Seth A. C., Gerhard O., 2013, *MNRAS*, 429, 2974
- Do T., Ghez A. M., Morris M. R., Lu J. R., Matthews K., Yelda S., Larkin J., 2009, *ApJ*, 703, 1323

- Do T., et al., 2013, ApJ, 779, L6
- Draine, B.T. 2003a, ARA&A, 41, 241
- Eggen OJ, Lynden-Bell D, Sandage AR 1962 ApJ 136:748
- Ekers, R. D., van Gorkom, J. H., Schwarz, U. J., & Goss, W. M. 1983, A&A, 122, 143
- Eckart, A., & Genzel, R. 1996, Nature, 383, 415
- Eddington, A.S. 1916 MNRAS, 76, 572
- Einsel, C., & Spurzem, R. 1999, MNRAS, 302, 81
- Eisenhauer, F., Genzel, R., Alexander, T., et al. 2005, ApJ, 628, 246
- Evstigneeva E. A. et al., 2008, AJ, 136, 461
- Etxaluze, M., Smith, H. A., Tolls, V., et al. 2011, AJ, 142, 134
- Fall S. M., Efsthathiou G., 1980, MNRAS, 193, 189
- Ferrarese L., Merritt D., 2000, ApJ, 539, L9
- Ferrarese L., Côtè P., Jordan A., et al., 2006, ApJS, 164,334
- Ferrarese, L., Ford, H., 2005, Space Sci. Rev. 116, 523624.
- Feldmeier, A., Neumayer, N., Seth, A., Schödel, R., Lützgendorf, N., de Zeeuw, P. T., Kissler-Patig, M., Nishiyama, S., & Walcher, C. J. 2014, ArXiv e-prints
- Fiestas, J., Spurzem, R., 2010, MNRAS, 405, 194
- Fiestas J., Porth, O., Berczik, P., Spurzem, R., MNRAS, 419, 57
- Flynn C., Holmberg J., Portinari L., Fuchs B., Jahrei H., 2006, MNRAS, 372, 1149
- Frebel A., Christlieb N., Norris J. E., Thom C., Beers T. C., Rhee J., 2007, ApJ, 660, L117
- Freeman K. C., 1987, ARA&A, 25, 603
- Freeman K., Bland-Hawthorn J., 2002, ARA&A, 40, 487
- Fritz T., From the Sun to the Galactic Center: Dust, Stars and Black Hole(s), 2013 Thesis
- Fritz T. K., et al. 2011, ApJ, 737, 73
- Fritz T. K., Chatzopoulos S., Gerhard O., Gillessen S., Dodd-Eden K., Genzel R., Ott T. Pfuhl O., Eisenhauer F., 2014, submitted
- Fuchs B., Jahreiß H., 1998, A&A, 329, 81
- Gould A., Flynn C., Bahcall J.N., 1998, ApJ, 503, 798

- Graham, A. W., & Spitler, L. R. 2009, MNRAS, 397, 2148
- Gerhard, O. 1991. MNRAS, 250, 812
- Gerhard O., 2011, Mem. Soc. Astron. Ital. Suppl., 18, 185
- Genzel R., Eisenhauer S., Gillessen S. 2010, Reviews of Modern Physics 82, 3121
- Genzel R, Schodel R, Ott T, Eisenhauer F, Hofmann R, Lehnert M, Eckart A, Alexander T, Sternberg A, Lenzen R, Clenet Y, Lacombe F, Rouan D, Renzini A & Tacconi-Garman L E 2003 ApJ 594, 812-832.
- Genzel, R., Thatte, N., Krabbe, A., Kroker, H., & Tacconi-Garman, L. E. 1996, ApJ, 472, 153
- Genzel R., Pichon C., Eckart A., Gerhard O.E., Ott T., 2000, MRAS, 317, 348
- Ghez, A. M., Duchene, G., Matthews, K., et al. 2003, ApJL, 586, L127
- Ghez A., et al., 2008, ApJ, 689, 104
- Gilmore G., Reid N., 1983, MNRAS, 202, 1025
- Graham A. W., Spitler L. R., 2009, MNRAS, 397, 2148
- Gillessen S., Eisenhauer S., Trippe S, Alexander T., Genzel R., Martins F., Ott T, 2009, ApJ, 707, L11
- Guesten, R., Genzel, R., Wright, M. C. H., et al. 1987, ApJ, 318, 124
- Haller, J. W., Rieke, M. J., Rieke, G. H., et al. 1996, ApJ, 456, 194
- Helmi A., 2008, A&AR, 15, 145
- Hernquist L., 1990, ApJ, 356,359
- Hill V. et al., 2002, A&A, 387, 560
- Hunter C., Qian E., 1993, MNRAS, 202, 812
- Humphreys R. M., Larsen J. A., 1995, AJ, 110, 2183
- Ho, L. C., Filippenko, A. V., & Sargent, W. L. 1995, ApJS, 98, 477
- Jackson, J. M., Geis, N., Genzel, R., et al. 1993, ApJ, 402, 173
- Jaffe W., 1983, MNRAS, 202, 995
- Jansky, K. G. 1932, Proceedings of the IRE, 20, 1932
- Juric, M., Ivezić, Z., Brooks, A., et al. 2008, ApJ, 673, 864
- Kantorowitsch, L.,1948, Functional analysis and applied mathematics (russ.). UMN3, 6 (28), 89185.

- Kim E., Yoon I., Lee H.M., Spurzem R., 2008, MNRAS, 383, 2
- Kormendy, J., 2013, in *Secular Evolution of Galaxies*, eds. Jesus Falc on-Barroso & Johan H. Knapen, Cambridge, UK: Cambridge University Press, 2013, 1
- Kuijken K. 1995 MNRAS 446, 194
- Kunneriath et al. 2012, A&A, 538A, 127K
- Launhardt R., Zylka R., Mezger P.G., 2002, A&A, 384, 112
- Levin, Y., & Beloborodov, A. M. 2003, ApJL, 590, L33
- Lindquist M., Winnberg A., Habing H.J., Matthews H.E., 1992, A&AS, 92, 43
- Lynden-Bell D., 1960 MNRAS, 120, 204L
- López-Corredoira M., Cabrera-Lavers A., Mahoney T. J., Hammersley P. L., Garzòn F., Gonzalez-Feràandez C., 2007, AJ, 133, 154
- Lotz J. M., Telford R., Ferguson H. C., Miller B. W., Stiavelli M., Mack J., 2001, ApJ, 552, 572
- Martinez-Valpuesta I., Gerhard O., 2011, ApJ, 734, L20
- McMillan P. J., 2011, MNRAS, 414, 2446
- Magorrian J. Binney J., 1994 MNRAS, 271, 949
- Magorrian J. 1995 MNRAS 277, 1185
- Magorrian, J. 1999, MNRAS, 302, 530
- Merritt D. & Szell A 2006 ApJ 648, 890-899
- Merritt, D. 1985. AJ, 90, 1027 and MNRAS, 214, 25p
- Merritt D., 2010, ApJ, 718, 739
- Merritt D., 2013. *Dynamics and Evolution of Galactic Nuclei*. Princeton, NJ: Princeton University Press
- McGinn, M. T., Sellgren, K., Becklin, E. E., & Hall, D. N. B. 1989, ApJ, 338, 824
- Minniti, D., & Zoccali, M. 2008, in *IAU Symp.*, ed. M. Bureau, E. Athanassoula, & B. Barbuy, 245, 323
- Mo H. J., Mao S., White S. D. M., 1998, MNRAS, 295, 319
- Morris, M. 1993, ApJ, 408, 496
- Morrison H. L., 1993, AJ, 106, 578

- Nagai R., Miyamoto M., 1975, PASJ, 27, 533
- Ortolani, S., et al. 1995, Nature, 377, 701
- Osipkov, L.P. 1979. PAZh, 5, 77 (in Russian). See also SvAL, 4, 42 (in English)
- Paumard, T., Maillard, J.-P., & Morris, M. 2004, A&A, 426, 81
- Paumard, T., Genzel, R., Martins, F., et al. 2006, ApJ, 643, 1011
- Portail, M. Wegg, C., Gerhard, O., Martinez-Valpuesta, I. MNRAS 448, 713
- Preto M. & Amaro-Seoane P. 2010 ApJ 708, L42-L46.
- Preto, M., Merritt, D., & Spurzem, R. 2004, ApJ, 613, L109
- Pfuhl, O., Fritz, T. K., Zilka, M., et al. 2011, ApJ, 741, 108
- Pfuhl, O., Alexander, T., Gillessen, S., et al. 2014, ApJ, 782, 101
- Qian E.E, de Zeeuw P.T., van der Marel R.P., Hunter C. 1995, MNRAS 274, 602
- Rattenbury N. J., Mao S., Debattista V. P., Sumi T., Gerhard O., De Lorenzi F., 2007b, MNRAS, 378, 1165
- Reid M.J., et al., 2014, arxiv:1401.5377
- Planets, Stars and Stellar Systems, 2013, pp 271-346
- Rieke, G. H., & Rieke, M. J. 1988, ApJL, 330, L33
- Rieke, G. H., Rieke, M. J., & Paul, A. E. 1989, ApJ, 336, 752
- Rix H.-W., Bovy J., 2013, A&AR, 21, 61
- Roberts, D. A. & Goss, W. M. 1993, ApJ, 86, 133
- Rossa J., van der Marel R. P., Böker T., et al., 2006, AJ, 132, 1074
- Schinnerer, E., Böker, T., Emsellem, E., & Lisenfeld, U. 2006, ApJ, 649, 181
- Schinnerer E., Böker T., Meier D. S., Calzetti D., 2008, ApJ, 684, L21
- Schinnerer E., Böker T., Emsellem E., Downes D., 2007, A&A, 462, L27
- Schinnerer, E., Böker, T., Meier, D. S., & Calzetti, D. 2008, ApJL, 684, L21
- Schödel R., Ott T, Genzel R., et al., 2002, Nature, 419, 694
- Schödel, R., Ott, T., Genzel, R., et al. 2003, ApJ, 596, 1015
- Schödel, R., et al., 2007, A&A, 469, 125

- Schödel R., Merritt D., Eckart A., 2009, *A&A*, 502, 91
- Schödel R., Najarro F., Muzic K., Eckart A., 2010, *A&A*, 511, A18
- Schödel R., Feldmeier A., Kunneriath D., Stolovy S., Neumayer N., Amaro-Seoane P., Nishiyama S., 2014, preprint (arXiv:1403.6657)
- Schwarzschild M., 1979, *ApJ*, 232, 236
- Scoville, N. Z., Stolovy, S. R., Rieke, M., Christopher, M., & Yusef-Zadeh, F. 2003, *ApJ*, 594, 294
- Sellwood J., 2008, *ApJ*, 679, 379
- Searle L., Zinn R., 1978 *ApJ* 225, 357
- Serabyn, E., & Lacy, J. H. 1985, *ApJ*, 293, 445
- Seth A., Dalcanton J. J., Hodge P. W., Debattista V. P., 2006, *AJ*, 132, 2539
- Seth A., Agueros M., Lee D., Basu-Zych A., 2008, *ApJ*, 678, 116
- Seth A., Agueros M., Lee D., Basu-Zych A., 2008, *ApJ*, 678, 116
- Sigurdsson S., Hernquist L., & Quinlan G. D. 1995, *ApJ*, 446, 75
- Siegel M. H., Majewski S. R., Reid I. N., Thompson I. B., 2002, *ApJ*, 578, 151 Skrutskie
- Stolovy S, Ramirez S, Arendt R G, Cotera A, Yusef-Zadeh F, Law C, Gezari D, Sellgren K, Karr J, Moseley H & Smith H A 2006 *Journal of Physics Conference Series* 54, 176-182
- Tremaine S. D., Ostriker J. P., Spitzer L., Jr, 1975, *ApJ*, 196, 407
- Syer, D., & Tremaine, S. 1996, *MNRAS*, 282, 223
- Tremaine, S., Gebhardt, K., Bender, R., et al. 2002, *ApJ*, 574, 740
- Tremaine S. D., Ostriker J. P., Spitzer L., Jr, 1975, *ApJ*, 196, 407
- Tremaine S., Richstone, D. O., Byun, Y., Dressler, A., Faber, S. M., Grillmair, C., Kormendy, J., Lauer, T. R. 1994, *AJ*, 107, 634
- Trippe S., et al., 2008, *A&A* 492, 419
- van der Marel R.P., Sigurdsson S., Hernquist L., 1997, *ApJ*, 487, 153
- van de Ven G., van den Bosch R. C. E., Verolme E. K., de Zeeuw P. T., 2006, *A&A*, 445, 513
- Valluri, M., Ferrarese, L., Merritt, D., Joseph, C.L., 2005 *AJ*, 628, 137152.
- Walcher, C. J., van der Marel, R. P., McLaughlin, D., et al. 2005, *ApJ*, 618, 237
- Wegg C., Gerhard O., 2013, *MNRAS*, 435, 1874

Wegg, Christopher, Gerhard, Ortwin, Portail, Matthieu arXiv:1502.00633

Wehner E. H., Harris W. E., 2006, ApJL, 644, L17

Weinberg M. D., Katz N., 2007, MNRAS, 375, 460

Wolfram Research, Inc., Mathematica, Version 8.0, Champaign, IL (2011)

Wollman, E. R., Geballe, T. R., Lacy, J. H., Townes, C. H., & Rank, D. M. 1977, ApJL, 218, L103

Zoccali M. et al., 2003, A&A, 399, 931

Zhang M., Magorrian J., 2008, MNRAS, 387, 1719

Zhao, Jun-Hui, Blundell, Ray, Moran, James M., Downes, Dennis, Schuster, Karl F., Marrone, Daniel P., 2010ApJ, 723, 1097Z

Zhao, J.-H., Morris, M. R., Goss, W. M., & An, T. 2009, ApJ, 699, 186

Zylka R., Mezger P. G., Ward-Thompson D., Duschl W. J., Lesch H., 1995, A&A, 297, 83

Acknowledgements

A PhD in science usually is (or at least it should be in my opinion) a several year daunting task with primary purpose to advance as far as possible the limits of our current knowledge about the universe.

As this four year long research adventure comes to an end I would like to thank and acknowledge all those who helped me in carrying out this project. Most importantly I would like to thank my supervisor Prof. Ortwin Gerhard for giving me the chance to be part of this amazing institute and particularly to the dynamics group and teaching me professionalism and focus in the detail.

Special thanks goes to Revekka for her full support over the years. In addition I would like to thank my parents and brother for their support, my friend Giorgos, Tobias for the assistance he provided on the data section of the project, Chris for the insightful conversations and valuable comments, Steffan for listening to me and supporting my project and my former supervisor Panos Patsis.

My warmest thanks also go to Isabella, Alessia, Jonny, Matthieu, Mattias, Manuel, Lucia and Angeles for their help in various ways. Finally I acknowledge the very high quality of education and research in Germany and specifically in the Max Planck Institute and I wish that every country could follow the same paradigm.